ISTANBUL TECHNICAL UNIVERSITY ★ EURASIA INSTITUTE OF EARTH SCIENCES

CLIMATE CHANGE IMPACTS ON THE HYDROLOGY OF THE EUPHRATES-TIGRIS BASIN

Ph.D. THESIS

Deniz BOZKURT

Department of Climate and Marine Sciences

Earth System Science Programme

Anabilim Dalı :   Herhangi Mühendislik, Bilim
Programı :   Herhangi Program

APRIL 2013

ISTANBUL TECHNICAL UNIVERSITY ★ EURASIA INSTITUTE OF EARTH SCIENCES

CLIMATE CHANGE IMPACTS ON THE HYDROLOGY OF THE EUPHRATES-TIGRIS BASIN

Ph.D. THESIS

Deniz BOZKURT
(601062009)

Department of Climate and Marine Sciences

Earth System Science Programme

Thesis Advisor: Prof. Dr. Ömer L. ŞEN
Anabilim Dalı :   Herhangi Mühendislik, Bilim
Programı :   Herhangi Program

APRIL 2013

İSTANBUL TEKNİK ÜNİVERSİTESİ ★ AVRASYA YER BİLİMLERİ ENSTİTÜSÜ

İKLİM DEĞİŞİKLİĞİNİN FIRAT-DİCLE HAVZASI HİDROLOJİSİNE OLAN ETKİLERİ

DOKTORA TEZİ

Deniz BOZKURT
(601062009)

İklim ve Deniz Bilimleri Anabilim Dalı

Yer Sistem Bilimi Programı

Tez Danışmanı: Prof. Dr. Ömer L. ŞEN
Anabilim Dalı :   Herhangi Mühendislik, Bilim
Programı :   Herhangi Program

NİSAN 2013

Deniz Bozkurt, a Ph.D. student of ITU **Eurasia Institute of Earth Sciences** student ID **601062009**, successfully defended the **dissertation** entitled "**Climate change impacts on the hydrology of the Euphrates-Tigris Basin**", which he prepared after fulfilling the requirements specified in the associated legislations, before the jury whose signatures are below.

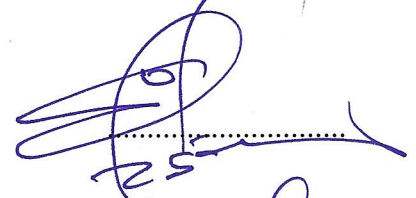Thesis Advisor :   **Prof. Dr. Ömer Lütfi ŞEN**
Istanbul Technical University

Jury Members :   **Prof. Dr. Mehmet KARACA**
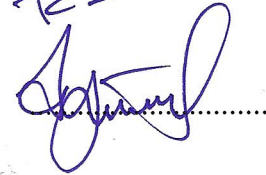Istanbul Technical University

Prof. Dr. H. Nüzhet DALFES
Istanbul Technical University

Prof. Dr. Emin ÖZSOY
Middle East Technical University

Assoc. Prof. Dr. İsmail YÜCEL
Middle East Technical University

Date of Submission : 1 March 2013
Date of Defense :   25 April 2013

I dedicate this thesis to my late father, Mehmet Bozkurt (1944-2004), who is a great giant of a proletarian educationist and who is sorely missed...,

FOREWORD

April 2013   Deniz BOZKURT

TABLE OF CONTENTS

ABBREVIATIONS

AIM : Asian Pacific Integrated Model
AOGCM : Atmosphere-Ocean General Circulation Model
AVHRR : Advanced Very High Resolution Radiometer
BATS : Biosphere-Atmosphere Scheme
BC : Before Calendar
CCM : Community Climate Model
CCSM : Community Climate System Model
CRU : Climate Research Unit
CT : Center Time
ECHAM : European Centre Hamburg Model
ECMWF : European Centre for Medium-Range Weather Forecasts
EMBS : Eastern Mediterranean-Black Sea
ERA40 : ECMWF Re-Analysis 40
ETB : Euphrates-Tigris Basin
FAO : Food and Agriculture Organization
GCM : General Circulation Model
GHG : Greenhouse Gas
GISST : Global Sea-Ice Sea Surface Temperature
GLCC : Global Land Cover Characterization
GTOPO : Global Topographic Data
HadAMH : Hadley Centre Global Atmospheric Model
HadCM : Hadley Centre Coupled Model
HDM : Hydrological Discharge Model
IIASA : International Institute for Applied Systems Analysis
IPCC AR4 : Intergovernmentanl Panel on Climate Change Assessment Report 4
JSBACH : Jena Scheme for Biosphere-Atmosphere Coupling in Hamburg
MDG-F : Millenium Development Goals-Fund
MESSAGE : Model for Energy Supply Strategy Alternatives and their General Environmental Impact
MiniCAM : The Mini Climate Assessment Model
MK : Mann-Kendall
MODIS : Moderate Resolution Imaging Spectroradiometer
MPI : Max Planck Institue
MPI-ESM-LR : Max Planck Institue-Earth System Model-Low Resolution
MPIOM : Max Planck Institue Ocean Model
NAO : North Atlantic Oscillation
NCAR : National Center for Atmospheric Research
NCEP : National Center for Environmental Prediction
NCP : North Sea-Caspian Pattern
NIES : National Institute for Environmental Studies
OISST : Optimum Interpolation Sea Surface Temperature

PNNL	**:** Pacific Northwest National Laboratory	
RegCM3	**:** Regional Climate Model Version 3	
RCM	**:** Regional Climate Model	
RCP	**:** Representative Concentration Pathway	
RMSD	**:** Root Mean Square Difference	
SAPRDA	**:** Southeastern Anatolia Project Regional Development Administration	
SRES	**:** Special Report on Emissions Scenarios	
SST	**:** Sea Surface Temperature	
SWE	**:** Snow Water Equivalent	
TSMS	**:** Turkish State Meteorological Service	
UNDP	**:** United Nations Development Programme	
USCB	**:** United States Census Bureau	

LIST OF FIGURES

CLIMATE CHANGE IMPACTS ON THE HYDROLOGY OF THE EUPHRATES-TIGRIS BASIN

SUMMARY

The Euphrates-Tigris Basin hosts two important snow-fed rivers of the Middle East and eastern Anatolia, and its water resources are critical for the hydroelectric power generation, irrigation and agriculture in the basin countries, namely Turkey, Syria, Iraq and Iran. The headwaters of the basin lies in the Taurus and Zagros Mountains, and it's particularly vulnerable to climate change. This study aims to provide a comprehensive assessment of climate change impacts on the hydrology of the basin within two research focus: (i) historical climate variability in the basin and (ii) regional hydro-climatological consequences of future climate change in the basin.

In order to reveal historical climate change signals in the basin, observed changes in temperature, rainfall and streamflow were investigated. Trend analysis of temperature indicates that there has been a striking temperature increase after the early 1990s. More pronounced and statistically significant increase in minimum temperatures in highlands are detected. In terms of precipitation, no striking change is found. The statistical analysis reveals that there are no significant trends in the annual streamflow data (i.e., covering 35 years from 1972 to 2006). However, the streamflow timings of the Euphrates and Tigris Rivers, are found to be shifting to earlier days in the year. Six out of eight stations indicate statistically significant shifts between two consecutive 17-years periods (i.e., 1972-1988 and 1990-2006). Among these stations, the average shift to earlier times is over 5 days, suggesting earlier spring melting of snowpack due to increased temperatures in the second period. A striking increase in the discharges takes place during the first half of March, and it is observed at all stream gauging sites considered in this study. An analysis based on the NCEP/NCAR reanalysis data indicates that warming which results in this increase is associated with the switching from the northeasterly flow to southwesterly flow over the Black Sea and western Anatolia caused by the weakening of the Siberian High over eastern Europe. These changes in the circulation features from the first to second periods are found to be very consistent with the positive and negative phases of the North Sea-Caspian pattern.

Hydro-climatic effects of future climate change in the Euphrates-Tigris Basin are investigated dynamically downscaled outputs of different GCM (ECHAM5, CCSM3 and HadCM3)-emissions scenario (A1FI, A2 and B1) simulations. The suite of simulations (total five) enables an analysis taking into account the A2 emission scenario simulations of three different GCMs (ECHAM5, CCSM3 ve HadCM3) and another analysis based on the three different emissions scenario (A1FI, A2 and B1) simulations of one GCM (CCSM3). All scenario simulations indicate winter surface temperature increases in the entire basin, however, the increase is larger in the highlands. The greatest increase in the annual temperature by the end of century belongs to the CCSM3 A1FI simulation with an increment of 6.1 $^{\circ}$C in the highlands.

There is a broad agreement amongst the simulations in terms of the winter precipitation decrease in the highlands and northern parts and increase in the southern parts of the basin. A remarkable impact of warming could be seen on the snow water equivalent in the highlands where each simulation points out statistically significant decreases ranging from 55% (lower emissions) to 87% (higher emissions). Statistically significant declines (25 to 55%) are found for the annual surface runoff of the main headwaters area. Moreover, significant temporal shifts to earlier days (between 18 and 39 days depending on the scenario) are projected to occur in the surface runoff timing in the headwaters region. Projected annual surface runoff changes in all simulations suggest that the territories of Turkey and Syria within the basin are most vulnerable to climate change, as they will experience significant decreases in the annual surface runoff. Eventually, however, the downstream countries, especially Iraq, may suffer more as they rely primarily on the water released by the upstream countries. The substantial changes in the hydro-climate of the basin, therefore, are likely to increase the challenges associated with the management of several dam reservoirs and hydropower plants in the basin in addition to causing further impacts on physical and biological components of the ecosystems along these rivers.

In addition to analysis of atmospheric model outputs, the impacts of future climate changes on river discharges in the basin are investigated via a hydrological discharge model (the HDM) using both CMIP3 and CMIP5 outputs. Simulations were carried out by using surface runoff and drainage outputs of two low resolution GCMs (CMIP3 simulations of ECHAM5 and CMIP5 simulations of MPI-ESM-LR). In addition to this, the HDM was forced by high resolution RCM outputs of different GCM (ECHAM5, CCSM3) - emissions scenario (A1FI, A2 and B1) simulations. Future hydrological discharge simulations indicate a striking decrease in discharge of the rivers in the basin. The decrease is more remarkable by the end of the century. Another important result of the hydrological discharge simulations is that significant temporal shifts to earlier days in the peak of discharges are projected by the end of the century. Different model and scenario combinations are in agreement with these two main results. High resolution RCM-forced simulations yield more pronounced decreases and shifting compared to the low resolution GCM-forced simulations.

İKLİM DEĞİŞİKLİĞİNİN FIRAT-DİCLE HAVZASI HİDROLOJİSİNE OLAN ETKİLERİ

ÖZET

Fırat-Dicle Havzası, Orta Doğu ve Doğu Anadolu'nun kar ile beslenen iki önemli nehrine ev sahipliği yapar. Havzanın su kaynakları, havza ülkeleri olan Türkiye, Suriye, Irak ve İran için hidroelektrik üretimi, sulama ve tarım gibi alanlarda kritik öneme sahiptir. Ancak insanoğlunun son yıllarda doğaya ve doğal yaşama gittikçe artan müdahalesi yüzbinlerce, hatta milyonlarca yılda oluşan dengeleri bozmaya başlamıştır. Fırat-Dicle Havzası'nın kapsadığı bereketli Mezopotamya toprakları ve çevresi de bu müdahalelerin yarattığı değişikliklerden nasibini almaya başlamıştır. Havzanın ana su kaynaklarının olduğu kar ile kaplı dağlık alanlar, Toros ve Zagros Dağları'nda yer alır ve iklim değişikliğine karşı özellikle savunmasızdır. Bu çalışma, iki araştırma konusu kapsamında, iklim değişikliğinin havza hidrolojisine olan etkilerinin kapsamlı bir değerlendirmesini hedeflemektedir: (i) havzadaki tarihsel iklim değişikliği ve (ii) gelecek iklim değişikliğinin havzadaki bölgesel hidro-iklimsel sonuçları.

Havzadaki tarihsel iklim değişikliği sinyallerini ortaya koymak için, sıcaklık, yağış ve akım verilerindeki gözlemlenmiş değişiklikler incelenmiştir. Tarihsel sıcaklık verileri havzanın kaynak kısımları için son yıllarda hem minimum hem de maksimum sıcaklıklarda istatistiksel olarak anlamlı artışların meydana geldiğini göstermektedir. Benzer bir analiz yağışta herhangi bir önemli değişikliğin olmadığını ortaya çıkarmıştır. 1972-2006 yılları arasını kapsayan akım verileri kullanılarak yapılan ayrıntılı bir çalışmada ise, bölgenin yıllık akımlarında anlamlı bir değişikliğin olmadığı sonucuna varılmıştır. Ancak, Fırat ve Dicle Nehirleri'nin tepe akım zamanlarında erkene kaymalar olduğu tespit edilmiştir. Bu çalışmada kullanılan 8 akım istasyonundan 6'sında, ardışık iki zaman periyodu arasında (1972-1988 ve 1990-2006) tepe akım zamanlarında 5 gün civarında erkene kaymalar görülmektedir. Bu değişim istatistiksel olarak anlamlıdır. Ayrıca çalışmada kullanılan akım istasyonlarının hepsinde Mart ayının ilk haftasında akımlarda dikkat çekici bir artış görülmektedir. NCEP/NCAR reanaliz verisi kullanılarak yapılan analizde görülmektedir ki ikinci dönemde bu akım artışına neden olan ısınmanın Karadeniz ve batı Anadolu üzerindeki rüzgar akımlarının kuzeydoğulu yönlerden güneybatılı yönlere doğru değişmesidir. Doğu Avrupa civarındaki Sibirya Yüksek Basıncı'nın ikinci dönemde zayıflaması, akımlardaki bu değişimin ana nedenidir. Birinci dönemden ikinci döneme doğru oluşan hava sirküklasyonlarındaki bu değişiklikler, Kuzey Denizi-Hazar Paterni'nin (North Sea-Caspian Pattern, NCP) pozitif ve negatif fazları ile oldukça uyumludur.

Gelecek iklim değişikliğinin havzadaki hidro-iklimsel etkilerini araştırmak için değişik küresel sirkülasyon modeli (ECHAM5, CCSM3 ve HadCM3) ve emisyon (A1FI, A2, B1) çıktılarının dinamik ölçek yöntemi ile küçültülmüş yüksek çözünürlüklü projeksiyonları kullanılmıştır. Toplamda beş farklı simulasyon sonucu

ile yapılan bu değerlendirme ile üç farklı genel sirkülasyon modelinin (ECHAM5, CCSM3 ve HadCM3) A2 emisyon senaryosunun ve tek bir modelin (CCSM3) üç farklı emisyon senaryosunun (A1FI, A2 ve B1) olduğu çıktılar analiz edilmiştir. Kullanılan modellerin performans analizleri içinse 1961-1990 periyodu referans dönem alınarak, model çıktıları gözlemlerle mukayese edilmiştir. Dinamik ölçek küçültmek için kullanılan bölgesel iklim modelinin (ICTP-RegCM3) performansı için de NCEP/NCAR reanaliz verisi dinamik olarak küçültülmüştür. Modellerin değerlendirilmesinde öncelikli olarak gridlenmiş gözlem verileri (CRU) kullanılmıştır. Ancak nispeten daha yoğun bir gözlem ağının olduğu bölgesel bir veri grubu da modellerin değerlendirilmesinde kullanılmıştır. Reanaliz verisi ile yapılan simülasyonlar RegCM3 bölgesel iklim modelinin yağış ve sıcaklıkla beraber üst seviyelerdeki değişkenleri iyi bir şekilde simüle edebildiğini göstermektedir. Ancak, bölgesel iklim modeli yağışı dağlık alanlardan olduğundan fazla simüle etmektedir. Kullanılan üç farklı genel sirkülasyon modelinin, kış yağışı ve sıcaklığını simüle etmede oldukça iyi olduğu tespit edilmiştir. ECHAM5 ve HadCM3 modelleri aynı zamanda yaz yağışı ve sıcaklığını da iyi simüle etmektedir, ancak CCSM3 simülasyonları gözlemlere göre kurak ve daha sıcak koşullar üretmektedir. Bu durum, bölgesel iklim modeline girdi olarak verilen CCSM3 verisinin üst seviyelerindeki kuruluktan kaynaklanmaktadır. Daha yoğun gözlem ağına sahip veri setinin kullanılması patern korelasyonunu geliştirmemekle beraber, gözlem ve model çıktıları arasında yağışın değişkenliği ve ortalama karekök hatası yönlerinden daha iyi sonuçlar vermektedir. Genel sonuç olarak, bu çalışmada değerlendirilen üç farklı genel sirkülasyon model çıktıları, ortaya konulan güçlü ve zayıf yönleri ile beraber bu bölge için iklim değişikliği ve etkileri çalışmalarında kullanılabilir.

Farklı modellerin farklı emisyon senaryo çıktıları kullanılarak yapılan analizler havzada kış yüzey sıcaklıklarının artacağını ve bu artışın havzanın yüksek yerlerinde daha fazla olacağını göstermektedir. En fazla yıllık sıcaklık artışı CCSM3 A1FI çıktıları ile yapılan ve en kötümser olan simülasyonlarda olup, yüzyıl sonunda 6.1 $^{\circ}$C artış öngörülmektedir. Tüm simülasyonlarda, kış yağışının havzanın dağlık alanlarında ve kuzey kesimlerinde azaldığı, havzanın güney kesimlerinde arttığı yönünde geniş bir uyumluluk vardır. Isınmanın dikkate değer bir etkisi havzanın dağlık kesimlerindeki kar-su eşdeğeri değişimlerinde görülmektedir. Bu bölgelerde tüm simülasyonlar, kar-su eşdeğerlerinde %55 (düşük emisyon) ile %87 (yüksek emisyon) arasında değişen ve istatistiksel olarak anlamlı azalmalar öngörmektedir. Ana su kaynaklarının olduğu bölgede ise yıllık yüzey akışı değerlerinde %25 ve %55 arası, istatistiksel olarak anlamlı azalmalar öngörülmektedir. Ayrıca, ana su kaynaklarının olduğu bölgede, yüzey akışlarının tepe zamanlarında ciddi bir şekilde erkene kaymalar (kullanılan senaryoya göre 18 ve 39 gün arası) tahmin edilmektedir. Tüm senaryolarda tahmin edilen yıllık yüzey akış değişimlerine göre, ciddi azalmaların öngörüldüğü havzanın Türkiye ve Suriye toprakları, iklim değişikliğine karşı en kırılgan bölgeleridir. Diğer taraftan, havzanın alt ülkeleri, özellikle Irak, yukarı taraflardan bırakılan suya öncelikle ihtiyaç duyduğu için sıkıntı çekebilir. Bu yüzden havzadaki önemli hidro-iklimsel değişiklikler, havzadaki baraj ve hidro-elektrik santrallerinin yönetimi ile ilgili zorlukların artmasına neden olabileceği gibi havzanın biyolojik ve fizyolojik ekosistem bileşenleri üzerinde daha fazla etkilere yol açabilir.

Atmosfer model çıktılarının analizlerine ek olarak, Max Planck Meteoroloji Enstitüsü'nde geliştirilen bir hidrolojik deşarj modeli (The Hydrological Discharge Model) ile gelecek iklim değişikliğinin havzadaki nehir akımlarına olan etkileri

ortaya konulmuştur. İlk aşamada, düşük çözünürlüklü iki farklı küresel iklim modelin yüzey akışı ve drenaj çıktıları hidrolojik deşarj modeli için girdi olarak hazırlanıp, simülasyonlar yapılmıştır. Daha sonra ise yüksek çözünürlüklü bölgesel iklim modeli çıktılarının değişik senaryo ve modellerine ait yüzey akışı ve drenaj verileri ile hidrolojik deşarj modeli çalıştırılmıştır. Düşük çözünürlüklü verilerle çalıştırılan hidrolojik model sonuçlarında akımın yıllık döngüsünün tam olarak simüle edilemediği tespit edilmiştir. Ayrıca, gene bu simülasyonlarda yıllık tepe akımının oluştuğu zamanın da doğru olarak simüle edilemediği görülmüştür. Bu iki ana sonuç, ağırlıklı olarak küresel iklim modelinden alınan çıktılardaki eksikliklerden kaynaklanmaktadır. Havzanın dağlık kesimlerindeki yağışın ana nedeni yüzey topoğrafyasının neden olduğu orografik yağışlar olduğu için, düşük çözünürlüklü çıktılarda bu yağışın bu dağılımı yeterince iyi simüle edilemez. Diğer taraftan, yüksek çözünürlüklü bölgesel iklim modeli çıktıları ile yapılan hidrolojik öteleme simülasyonlarda ise, akımın yıllık döngüsü oldukça iyi çıkmıştır. Ancak bu simülasyonlarda, ıslak aylarda akımın gözlemlere göre fazla simüle edilmesi ve tepe akımının zamanlarında yanılma gibi sistematik hatalar da tespit edilmiştir. Bu hatalar çoğunlukla bölgesel iklim model çıktılarındaki, özellikle yıllık yağış döngüsündeki, eksikliklerden kaynaklanmaktadır. Gerçekten de, ıslak aylar için gözlemlenmiş yağış verisi ile yapılan karşılaştırmalarda, bölgesel iklim model çıktılarına ait yağışın havzanın üst kesimlerinde daha fazla simüle edildiği tespit edilmiştir. Ayrıca, bölgesel iklim model çıktılarında, geçiş aylarındaki (Mart) daha yüksek sıcaklık değerleri, erken kar erimelerine neden olarak yüksek akım değerlerinin ortaya çıkmasına neden olabilmektedir.

Atmosfer model çıktılarından elde edilen yüzey akışı analizlerine paralel olarak, hidrolojik öteleme modelinden elde edilen toplam akımlardaki değişimler de özellikle yüzyıl sonuna doğru akımlarda ciddi azalmaların meydana geleceğini öngörmektedir. Ayrıca, gene aynı paralellikte, akımların tepe zamanlarında dikkat çekici bir şekilde erkene kaymalar da öngörülmüştür. Farklı model ve senaryo kombinasyonları bu sonuçlarda hemfikirdir. Yüksek çözünürlüklü bölgesel iklim model çıktıları ile yapılan hidrolojik öteleme simülasyonları, düşük çözünürlükteki küresel iklim modeli çıktıları ile yapılan simülasyonlara nazaran daha belirgin akım azalmaları ve tepe akımlarında erkene kaymalar üretmektedir.

1. INTRODUCTION

It is widely recognized that the increasing temperatures have the potential to greatly impact the global and regional hydrological cycle (IPCC, 2007). Geographic areas where the water cycle is dominated by snowmelt hydrology are expected to be more susceptible to increasing temperatures as they affect the snow cover and seasonality of runoff (Stewart et al., 2005; Adam et al., 2009; Özdoğan, 2011; Sen et al., 2011). Himalayan region, for instance, is considered highly vulnerable due to the profound impacts of climate change on snow cover and glaciers (Xu, 1999; Singh and Bengtsson, 2004; Immerzeel et al., 2010). In recent years, the potential impacts of climate change on hydrological cycle and water resources in such regions have been of interest to many researchers (e.g. Xu, 1999; Hayhoe et al., 2007; Sorooshian et al., 2008; Chenoweth et al., 2011). These regions are relatively far from the human developments, and for this reason, they are also considered to be arguably the best places to detect the global climate change signal that is not "contaminated" by the small-scale phenomena such as urban heat island effect (Sen et al., 2011). In such regions, however, several factors including the inadequate observational network and difficulty of maintenance of the available hydrometeorological stations affect the quality and quantity of the data that could be used in the climate change studies. Furthermore, regional disputes and conflicts may severely complicate the in-situ data collection in some of these regions. Studies on the hydroclimatology of the large Euphrates and Tigris Basin suffer from all these deficiencies. The problem of the lack of adequate data in such studies is usually overcome by the use of the atmospheric and hydrological models (e.g. Kavvas et al., 2011). In addition to historical analysis, these models are used to generate projections on the future changes in the regional hydrology.

Global Circulation Models (GCMs), whose data are easily accessible by hydrologists, are commonly used in large-scale climate change impact studies, and they can have a key role to understand future global climatic changes (Fujihara et al., 2008). The GCMs, on the other hand, provide limited information about the climate

change impacts on hydrology and water resources at sub-regional scales. This is primarily due to their coarse spatial resolutions, which do not adequately resolve the structure of the earth's surface at these scales (Busuioc et al., 1999). One common procedure for obtaining fine scale regional information is to dynamically downscale the GCM outputs using a regional climate model (RCM). In recent years, the RCMs have been increasingly used to determine the climate change impacts on water resources and water cycles using different emissions scenarios (e.g. Wilby et al., 2000; Hay et al., 2002; Christensen et al., 2004). Due to computational costs of their use, however, it is usually difficult for a research group to obtain a set of high-resolution RCM simulations that amounts to an "ensemble", which is preferable in climate change and impact studies as it allows better analysis of uncertainties. Thus, the RCM studies usually involve limited number of simulations, which is also the case in the present study.

1.1 Motivation

There is no doubt that enhanced greenhouse forcing has been unequivocally altering the radiative balance of the atmosphere, causing changes in climatic variables (Houghton et al., 1990). The Fourth Assessment Report of the Intergovernmental Panel on Climate Change (IPCC, 2007) points out that the Middle East, which lies in the east of the Mediterranean Basin, is one of the most vulnerable regions to the global climate change. Indeed, downscaling studies (e.g. Gao et al., 2006; Önol and Semazzi, 2009), providing greater details for the region, demonstrate significant large-scale reductions in precipitation besides increases in temperatures by the end of the twenty-first century. Intriguingly, just to the north of the basin, e.g., the Alps, the Carpathians, the Black Sea Basin and the Caucasus mountains, the same studies generally indicate increases in precipitation. According to these results, summer mean temperature differences indicate that temperature increase reaches up to 5-6 ºC over the Eastern Mediterranean Basin. These results suggest that such changes in climatic variables can have significant impacts on the hydrological process by causing variations in snow cover, runoff and evapotranspiration in different scales.

The Euphrates-Tigris Basin (hereafter ETB) hosts the two important snow-fed rivers of the Middle East, and its water resources are critical for the hydroelectric power generation, irrigation and domestic use in the basin countries, namely Turkey, Syria,

Iraq and Iran. Kavvas et al. (2011) developed a regional hydroclimate model, which consists of different modules such as atmosphere, snow, soil/vegetation and river, for water balance assessment of the ETB. They successfully modeled water balance of the basin based on the hydrologic period of water years 1957 through 1969, which represents the period prior to the construction of large dams. Based on the actual observed data, they reproduced via the model that approximately 90% of the Euphrates flow originates in Turkey, whereas 46% of the Tigris flow originates in Turkey. It is only very recently that studies for the climate change impacts on regional hydrology and water cycle have been performed for the ETB. Akyurek et al. (2011) analyzed changes in snow-covered area over the upper Euphrates Basin in Turkey by using the MODIS snow products for 10 years (2000 - 2009). They reported no significant changes in the extent of the snow-covered area over this relatively short period. Özdoğan (2011) assessed the effects of climate change on the amount of water stored in snowpack in the mountains of the ETB using a hydrological model and a set of regional climate change simulations driven by thirteen different GCM outputs forced with two greenhouse gas emissions scenarios. This recent study reports substantial declines (between 10 and 60%) in the available snow water, particularly under the A2 scenario, by the end of this century. Greatest changes (over 50%) were found to take place in lower elevations. Despite some uncertainties in both GCMs and hydrological model, the study of Özdoğan (2011) shows that climate change could seriously affect the water resources and lead to serious disputes among the countries that have territories in the ETB. Chenoweth et al. (2011) investigated the likely effects of climate change on the water resources of the eastern Mediterranean and Middle East regions using a high-resolution climate model forced by lateral boundary conditions from the HadCM3, driven by SRES A1B scenario. They found that the average annual Euphrates-Tigris river discharge could decline by 9.5% by 2040-2069 with the greatest decline (12%) in Turkey, while it is only 4% in Iraq. They also found further decrease in river discharge by 2070-2099; however, the decrease is less than 1%. Kitoh et al. (2008) estimated a discharge decrease of 29 - 73% for the Euphrates River by the end of the present century (2080-2099) based on moderate and high emissions scenario simulations carried out by a super-high-resolution GCM. Nohara et al. (2006) also reported a 40% decrease in the annual streamflow of the Euphrates River based on simulations of nineteen coupled-atmosphere-ocean GCMs under A1B scenario.

1.2 Purpose

Water has historically played a central role in the civilizations of the ETB, especially of Mesopotamia, which is the fertile land between the Euphrates and Tigris Rivers. The increasing population together with climate change makes the future of the water resources an important issue in the region. The objective of the present study is therefore to provide a compherensive analysis for past and future climate change impacts on the hydrology of the ETB within two research topics: (i) historical climate variability in the basin and (ii) regional hydro-climatological consequences of future climate change in the basin (Figure 1.1).
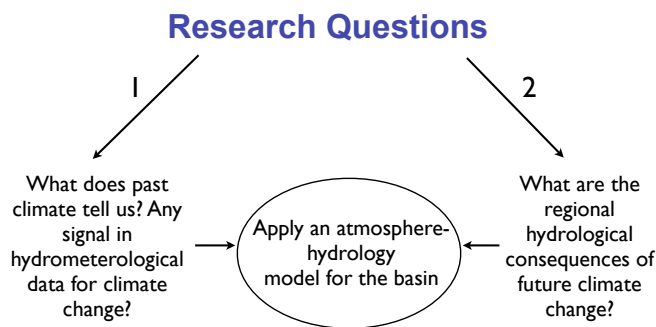
Figure 1.1 : Purpose diagram and research questions of the thesis.

1.3 Method and Thesis Plan

In order to demonstrate historical climate variability, an investigation of how changes in hydrometeorological variables and large-scale patterns affect regional hydrology in the context of changing climate was carried out using the meteorological and streamflow stations. A diagnostic study for changes in the snowmelt-derived streamflow in the Euphrates Basin was performed as well as trend analysis for temperature and precipitation data from meteorological observations. Hydro-climatic effects of future climate change in the basin have been investigated using dynamically downscaled outputs of different GCM (ECHAM5, CCSM3 and HadCM3)-emissions scenario (A1FI, A2 and B1) simulations via a regional climate model (RegCM3), obtained from a UNDP project (MDG-F 1680) entitled with "Enhancing the capacity of Turkey to adapt to climate change". Atmospheric model performance evaluation in terms of precipitation and temperature was perfomed by comparing the reference period simulations with the observations. The future climate change impact assessments were then achieved through a comparison of the

projected climate changes with the corresponding modeled climatology for the reference period. The suite of simulations (total five) enables an analysis taking into account the A2 emission scenario simulations of three different GCMs (ECHAM5, CCSM3 ve HadCM3) and another analysis based on the three different emissions scenario (A1FI, A2 and B1) simulations of one GCM (CCSM3). In addition to analysis of atmospheric model outputs, the impacts of future climate changes on river discharges in the basin have been investigated via a hydrological discharge model (the HDM). Simulations have been carried out by using surface runoff and drainage outputs of two low resolution GCMs (ECHAM5, MPI-ESM-LR). In addition to this, the HDM was forced by high resolution RCM outputs of different GCM (ECHAM5, CCSM3) - emissions scenario (A1FI, A2 and B1) simulations. Flow diagram of the atmospheric and hydrological modeling part of the study is given in Figure 1.2.
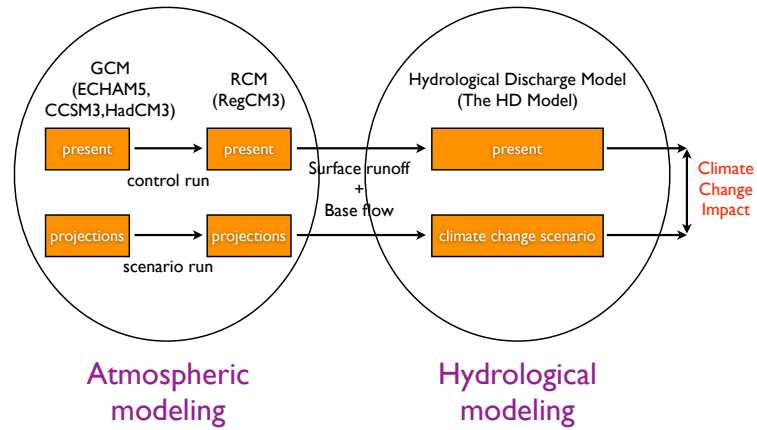
Figure 1.2 : Flow diagram of future climate change assessment in the basin.

The next section (Chapter 2) describes the basin and its climate. Chapter 3 provides the observational dataset and observed climate change impacts in the basin. Model descriptions, RCM simulations with performance evaluation and hydro-climatological consequences of future climate change in the basin are demonstrated in Chapter 4. Hydrological discharge model and simulations are provided in Chapter 5. Finally, the results and conclusions are discussed in Chapter 6.

2. STUDY BASIN

The ETB is a major basin in the Middle East, and it drains an area of approximately 880000 sq km (Figure 2.1). The basin lies in the territories of Iraq (46%), Turkey (22%), Iran (19%), Syria (11%), Saudi Arabia (1.9%) and Jordan (0.03%) (FAO, 2009).
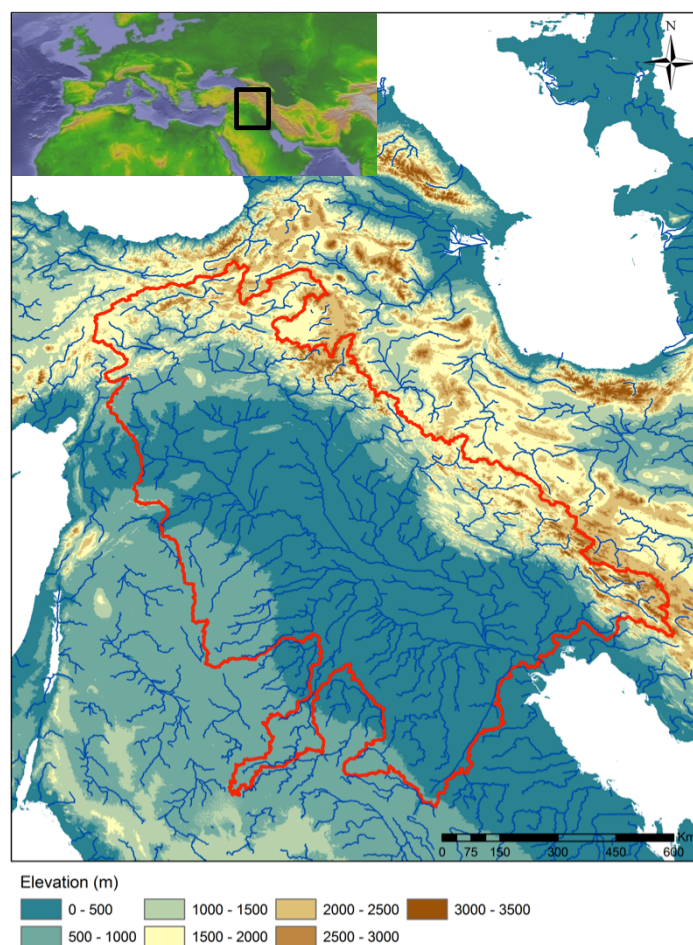
Figure 2.1 : Location and border of the Euphrates-Tigris Basin on a digital elevation map derived from GTOPO30, Global 30 Arc-Secon Elevation Data.

The ETB is characterized by the two snow-fed rivers, the Euphrates and Tigris, which originate from the eastern Anatolia with heights of up to 4500 meters. Not only for feeding the southeastern Turkey and Mesopotamian lowlands but also for transporting the products of erosion across the southern portion of the Anatolian microplate and the Arabian Platform of Turkey, Syria, and Iraq (since it drains the

7

youngest collision within the Alpine-Himalayan orogenic belt), the ETB has been constituted a key role in hydrological and geological characteristics of the Mesopotamian civilization (Nicoll, 2009). The Euphrates River (with an annual total flow around 30 billion cubic meters (FAO, 2009)) originates in eastern Turkey and feeds the southeastern Turkey, much of northern and eastern Syria and Mesopotamian lowlands of Iraq with a mouth at the head of the Persian/Arabian Gulf (Kolars and Mitchell, 1991). The eastern Anatolian mountains of Turkey provide approximately 90% of the Euphrates total annual flow, modest contributions come from the Syrian highlands and only minimal additions come from Iraq (Gruen, 2000; FAO, 2009). The Tigris River (with an annual total flow around 50 billion cubic meters (FAO, 2009)) originates in the eastern Taurus Mountains of southeastern Turkey near Lake Van. It flows across the Mesopotamian lowlands by following the base of the Zagros Mountains and reaches its outlet at the Persian Gulf. The southeastern Anatolian mountains of Turkey contribute approximately 50% of the total Tigris flow, whereas the remaining flow comes from numerous tributaries that originate in the Zagros Mountains between Iraq and Iran (Gruen, 2000; FAO, 2009).

The basin has a rich history and culture. It hosted "The Cradle of the Civilization" and the region is called as "Mesopotamia", a Greek name that has a meaning of land between the rivers. Due to flat and vast alluvial plain between the Euphrates and Tigris Rivers, The Fertile Crescent region hosted the earliest civilizations as people formed permanent settlements (Figure 2.2). Throughout much of its history Mesopotamia was divided into two halves, north (Subir) and south (Sumer), based on differences in language, geography, cultural spheres of influence and the use of irrigation (Walshaw, 1999). The northern plains were covered by rain-fed agricultural plains, while the southern plains were fed through drawn from the Euphrates (Weiss, 1986). The majority of Mesopotamian cultures thrived first in the south, reaching the north only through long term residence and slow invasion (Walshaw, 1999). The importance of rivers for the earliest civilizations were based on transportation, fertile soils leaved by river floods and irrigation. With such a vast fertile areas under favorable climate conditions, many developments such as urbanization, civilization, agriculture, mathematics and astronomy took place in that area. Moreover, it hosted the first empire that is under the rule of Sargon of Akkad and his descendants, the Akkadians more than 4000 years ago (Weiss et al., 1993).

Figure 2.2 : The earliest civilizations in flat alluvial plain between the Euphrates and Tigris Rivers called as "The Fertile Crescent" (Url-1).

In modern civilizations, these rivers have been at the center of international disputes over water availability and use (Daoudy, 2004). The basin is marked as water-stressed and the region is notorious for water scarcity as ever greater demands are placed on limited water resources through population growth and economic development (Chenoweth et al., 2011). Table 2.1 provides basic socioeconomic and water resources data for the main countries around and inside the basin, including volume of precipitation, internal water resources, and percentage of available water resources used (Chenoweth et al., 2011). With rapid population growth (i.e. the population in this region quadrupled in 55 years, increased from 46 million in 1950 to 180 million in 2005 (USCB, 2009)) and industrialization, renewable water potential per capita per year has been decreasing. Furthermore, the issue of water rights became a point of contention for Iraq, Syria and Turkey, beginning in the 1960's when Turkey implemented the Southeastern Anatolian Project, a 30-billion-dolar investment, which aims to generate energy (SAPRDA 2009) and to irrigate vast semi-arid plains in southeastern Turkey via constructing 19 hydropower plants and 22 dams. The amount and quality of the water received by the downstream have been reduced then. Lastly, the 2008 drought in Iraq and Syria sparked new negotiations between the basin countries over transboundary river flows. However, water is still at the center of the international disputes among the countries in the Middle East and the disputes are expected to grow in the future as a result of climate change impacts on the region.

Table 2.1 : Basic socioeconomic and water resources data for Iraq, Syria and Turkey. Table adapted from Chenoweth et al., 2011.[*]

Country	Area (km^2)	Human Development Level	GDP per Capita (PPP $)	2009 Population (x 10^6)	Volume of Precipitation (km^3 yr^{-1})	Internal Renewable Water Resources (km^3 yr^{-1})	Current Water Withdrawals as a Percentage of Total Renewable Water Resources
Iraq	438,320	-	-	30.747	94.7	35.2	85.3
Syria	185,180	medium	4,760	21.906	46.7	7.0	61.5
Turkey	783,560	high	13,359	74.817	459.5	227.0	18.3

* Sources are the Food and Agriculture Organization (FAO, AQUASTAT, 2009), United Nations Population Division (2009), and United Nations Development Programme (2010). GDP, gross domestic product; PPP, purchasing power parity. All dollar values are given in U.S. dollars.

2.1 Climate of the Basin

Water availability, rather than temperature, is the key climatic determinant for life in semiarid expanses across the planet (deMenocal, 2001). Not only for hosting broad river-fed agricultural lands in the south and snow-covered mountains in the north, but also being extremely vulnerable to any reductions in available surface and ground water, the ETB has been inevitably sensitive to climate variability since the beginning of the earliest civilizations. In one hand, for instance, under favorable climate conditions between 2300 and 2200 BC, Akkadian Empire dominated over the Mesopotamian region, which is linked productive but remote rain-fed agricultural lands of northern Mesopotamia with the irrigation agriculture tracts of southern Mesopotamian cities (deMenocal, 2001). On the other hand, climatic changes are thought to punctuate and redirect cultural trajectories in the late prehistoric-early historic Eastern Mediterranean and Mesopotamian regions (Weiss et al., 1993; deMenocal, 2001; Kaniewski et al., 2010). For instance, drought hypothesis was developed by Weiss (1982) to explain the Late Bronze Age (LBA) collapse, which was a period of collapse of cities and states from Greece through Mesopotamia to Egypt. Weiss et al. (1993) concluded that the desertification and desertion of the Habur Plains between ~2200 and 1900 BC engendered the collapse of the Akkadian Empire, and the attendant displacement of Hurrian, Gutian, and Amorite populations into southern Mesopotamia. Moreover, several studies based on regional paleoenvironmental proxy data has indicated that striking decrease in rainfall that is also correlated with minima in the Euphrates and Tigris river discharges from 1150 to 950 BC, is one of the main reasons for the declining of the Babylonian and Assyrian Empires between 1200 and 900 BC (Brinkman, 1968; Kay and Johnson, 1981; Neumann and Parpola, 1987; Alpert and Neumann, 1989; Kaniewski et al., 2010). Natural climate variability and forcings such as solar forcing, ocean circulation changes, atmospheric teleconnections and volcanic eruptions have been considered to explain the such these late Holocene climate variabilities in the basin and its surrounding in several studies (e.g. Weiss et al., 1993; Bond et al., 2001; deMenocal, 2001; Kaniewski et al., 2010). For instance, deMenocal (2001) highlighted a possible atmospheric teleconnection mechanism which relates the

aridification of Mesopotamia near 2100 BC with the onset of cooler sea surface temperatures in the North Atlantic.

Having being located between sub-tropical and mid-latitude regions, and influenced by several climate factors, the ETB region must be considered as a climate hot spot. Therefore, one should know about the general climate characteristics of the region, before any assessment of anthropogenic climate change impacts. The climate of the ETB is mainly determined by the large-scale circulation patterns, teleconnections and regional topography. Highlands of the ETB demonstrate the characteristics of cold-continental climate, while lowlands are classified as hot desert climate and hot semi-arid climate according to Köppen climate classification (Figure 2.3). In summer both lowlands and highlands of the ETB are under the influence of tropical air masses, whereas in winter the highlands are broadly under the influence of polar air masses (Figure 2.4). In the cold half of the year, maritime polar air masses from the Atlantic with a track over eastern Europe favor the cyclogenesis over the eastern Mediterranean, which are responsible for the majority of the annual precipitation in eastern Mediterranean and many parts of the ETB (Alpert et al., 1990; Cullen and deMenocal, 2000; Lionello et al., 2006; Romem et al., 2007).
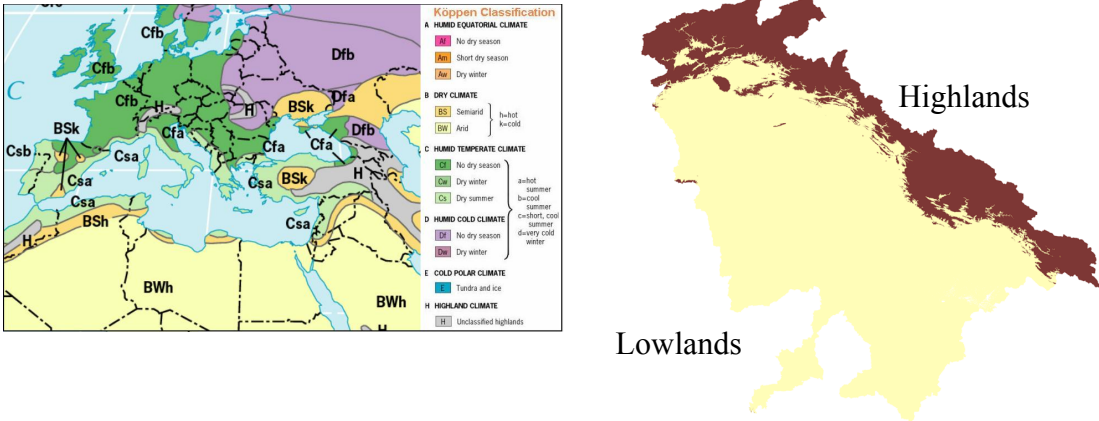
Figure 2.3 : Köppen climate classification and highlands and lowlands of the basin.

The cyclones crossing the eastern Mediterranean are the main moisture sources of orographic precipitation in the Taurus and Zagros Mountains located inside the ETB. One of the major climate characteristics of the ETB is the domination of subtropical high-pressure system during summer that leads to summer dryness in lowlands. The thermal low centered over Persian Gulf that is a branch of the Asian monsoon low

also influences the ETB by bringing dryer air from over Asian continent (Rohling and Hilgen, 1991; Krichak et al., 2010).
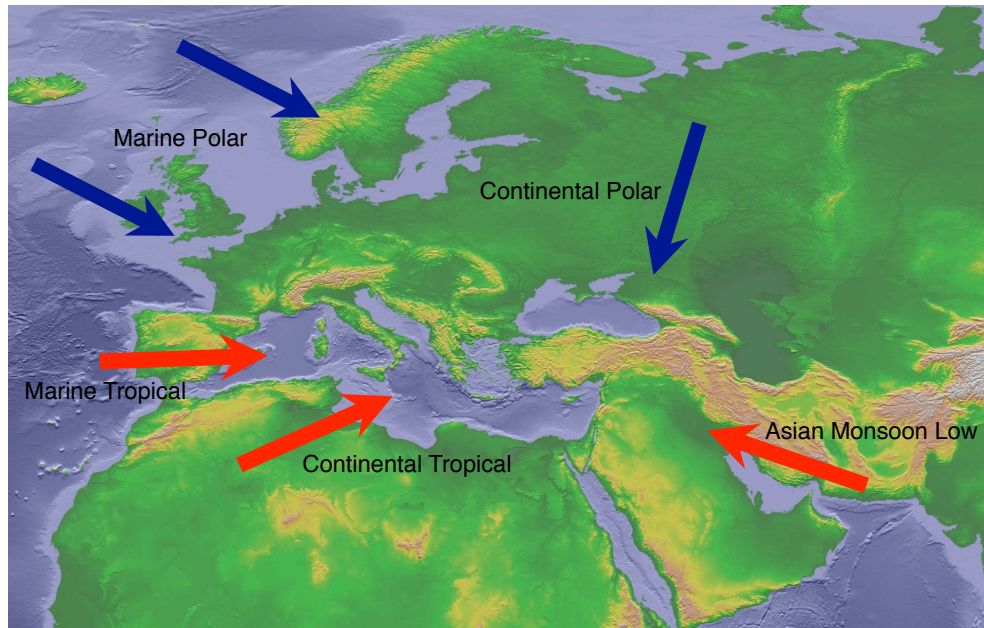
Figure 2.4 : Air massess influencing the Euphrates-Tigris Basin and its surrounding.

Large-scale circulation patterns and atmospheric teleconnections also influence the climate of the ETB. A robust signal between winter precipitation over the ETB and North Atlantic Oscillation (NAO) was documented by several diagnostic studies (Hurrel, 1995; Cullen et al., 2002; Trigo et al., 2004). The North Sea-Caspian Pattern (NCP) is also reported to have strong influence on the temperature variability of the ETB (Kutiel and Benaroch, 2002; Kutiel et al., 2002; Türkeş and Erlat, 2009). In a recent study, Sen et al. (2011) found a striking increase in the discharges of the Anatolian tributaries of the Euphrates and Tigris Rivers during the first half of March in recent years, which causes a shift in the peak flows to earlier days. According to their analysis based on NCEP/NCAR Reanalysis data, warming that results in this increase is associated with the switching from the northeasterly flow to southwesterly flow over the Black Sea and western Anatolia caused by the weakening of the Siberian High over eastern Europe, which are found to be very consistent with the positive and negative phases of the NCP identified by Kutiel and Benaroch (2002). Except from the large-scale effects, the region is also under influence of important local factors such as sea surface temperature (SST) and orography. In a recent study, sensitivity of precipitation in the Anatolian Peninsula to increased SSTs in the surrounding seas was investigated through regional climate model sensitivity

simulations and it was highlighted that the additional heat and moisture gained over the warmer eastern Mediterranean Sea are carried over the eastern Anatolia (Bozkurt and Sen, 2011). The moisture advection makes statistically significant increases in the winter precipitation in large areas in the eastern Anatolia, which are the main headwaters of the Euphrates and Tigris Rivers. In terms of orographic influences, eastward propagation moisture flux towards the basin results in a greater likelihood of orographic precipitation over the Taurus and Zagros mountain ranges (Evans et al., 2004).

Due to surrounding mountains, interior steppe and deserts of Syria and Iraq receive very little amount of precipitation (Evans et al., 2004). Annual rainfall in the lowlands is about 300 mm, while it reaches to about 600 mm in the highlands (Bozkurt et al., 2012). The basin receives much of the precipitation in winter. Annual average surface temperatures of lowlands and highlands are about 20 ^{o}C and 9 ^{o}C, respectively (Figure 2.5). Monthly fractions of the streamflow gauging stations located in the headwaters of the Euphrates and Tigris Rivers in eastern Anatolia indicate that 60-80% of their total annual flows occur in March-June period with a peak in April (Sen et al., 2011). This is a good indicator of the fact that these rivers are primarily fed by snowmelt runoff.
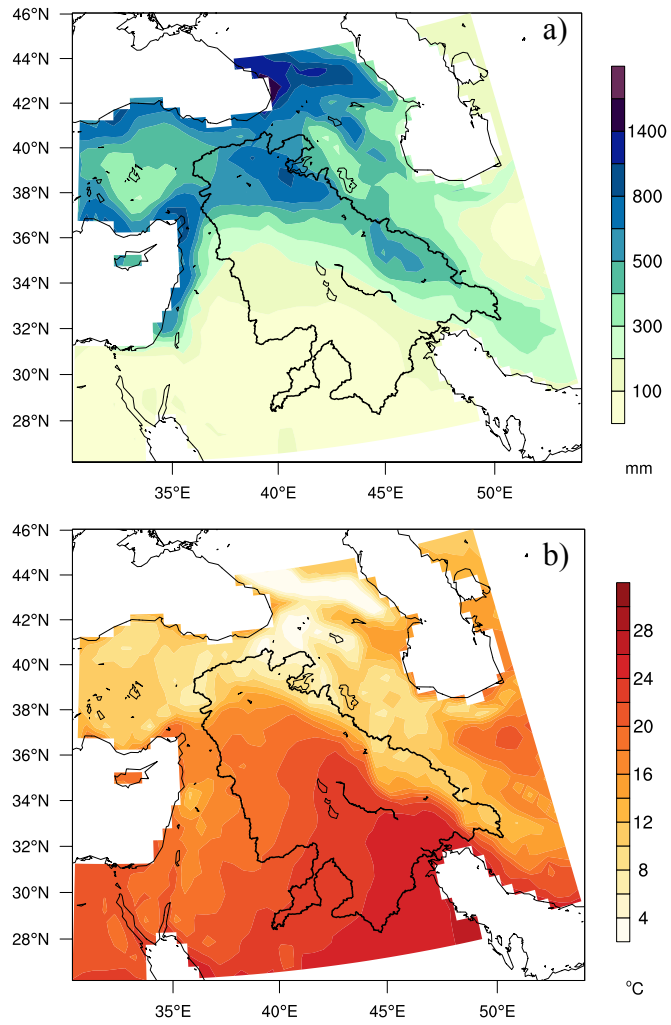
Figure 2.5 : 30-year (1961-1990) observed mean annual precipitation (a) and temperature (b) distribution in the basin.

3. OBSERVED CLIMATE CHANGES IN THE BASIN

3.1 Data and Method

In order to demonstrate observed climate changes and its impacts in the basin, by using meteorological and streamflow stations, an investigation of how changes in hydrometeorological variables and large-scale patterns affect regional hydrology in the context of changing climate was carried out. A diagnostic study for changes in the snowmelt-derived streamflow in Euphrates Basin was performed as well as trend analysis for temperature and precipitation data from meteorological observations. Results of observed changes in streamflow of the Euphrates and Tigris Rivers together with the atmospheric teleconnections influencing these changes was published by Sen et al. (2011) in which I was involved as co-author. Therefore, streamflow analysis in this chapter mainly consists of the analyzes and results in Sen et al. (2011). Analyzes covering the whole basin in terms of precipitation and temperature are based on the data provided by University of East Anglia, Climate Research Unit (CRU). The CRU global climate dataset consists of multi-variate 0.5^{o} latitude by 0.5^{o} longitude resolution monthly climatology for global land areas (Figure 3.1). The number of the CRU stations within the basin is 26. In addition to the CRU data, a regional dataset of precipitation and temperature in the main headwaters of the basin, which is based on relatively dense gauging network is also used to see how it affects the results (Figure 3.2). The regional dataset (17 stations in the main headwaters region) is provided by Turkish State Meteorological Service (TSMS). These data are first subjected to the Mann-Kendall (MK) trend test to determine whether there is statistically significant trends in precipitation and temperature between 1961 and 2002. General information for the MK test and its algorithm are provided in Appendix A.

Streamflow records were obtained from Turkish General Directorate of Electrical Power Resources Survey and Development Administration Hydro-Climatic Data Network for 21 stations. It should be noted that these two rivers are an essential part

of the Southeastern Anatolian Project, a 30-billion-dollar investment which aims to produce energy (SAPRDA, 2009) and to irrigate vast semi-arid plains in the southeastern parts of Turkey via constructing 19 hydro-power plants and 22 dams. Streamflow measurements at downstream locations of dams and/or hydro-power plants were excluded in this study since such man-made structures might divert streamflow from its natural characteristics.
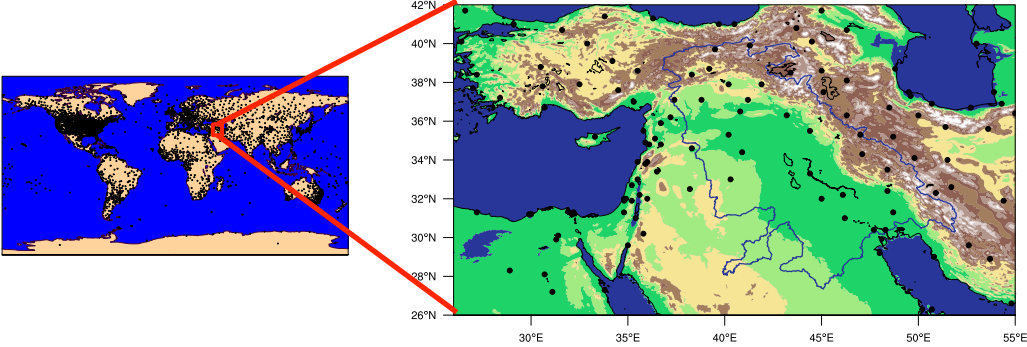
Figure 3.1 : CRU station data distribution over the globe and the ETB.
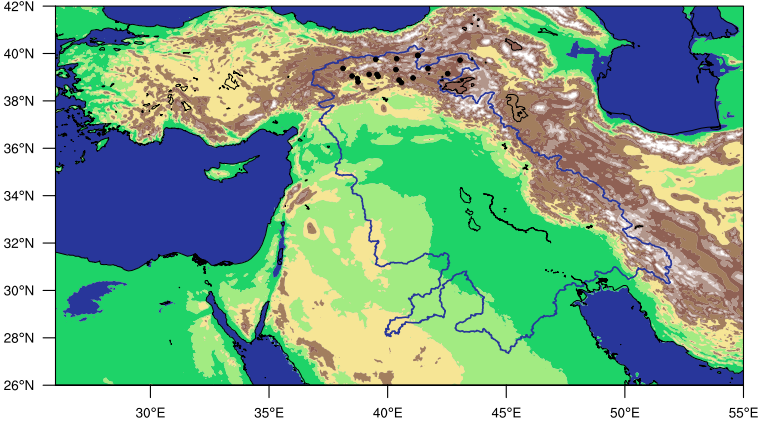
Figure 3.2 : Meteorological stations in the main headwaters of the basin.

After filtering the data for location, length and quality, 8 gauging stations remain to be used for analysis. All these stations have 35-year continuous daily measurements between 1972 and 2006. We also used daily surface temperature data in the analysis that were obtained from the TSMS for six sites in (or near) the basins that feed the tributaries of Euphrates and Tigris rivers. Locations of the climate stations as well as streamflow measurement sites are given in Figure 3.3. Informations about the streamflow gauging stations used in this part can be found in Table 3.1. In order to

investigate the corresponding changes in the atmospheric fields, data from NCEP/NCAR Reanalysis was used (Kalnay et al., 1996).

In order to detect the changes in the streamflow timing, researchers have used different measures, such as 'spring pulse onset' that define the date when snowmelt streamflow begins to cause an increase in discharge in spring or early summer (Cayan et al., 2001), and 'center time' (CT) that defines the date that marks the timing of the center of mass of annual flow (Stewart et al., 2005). In this study, CT was adopted as the measure to detect any shifts in streamflow timing. In the first part of the analysis, the CT dates were estimated and then the significance of the differences between two periods were assessed using the Monte Carlo test. The CT dates were estimated and then the significance of the differences between two periods were assessed using the Monte Carlo test. The CT dates were estimated from the daily streamflow measurements for every year at all measurement sites. The CT data were then divided into two periods of 17 years (i.e. 1972–88 and 1990– 2006), and mean values were compared for possible changes (named as actual difference).
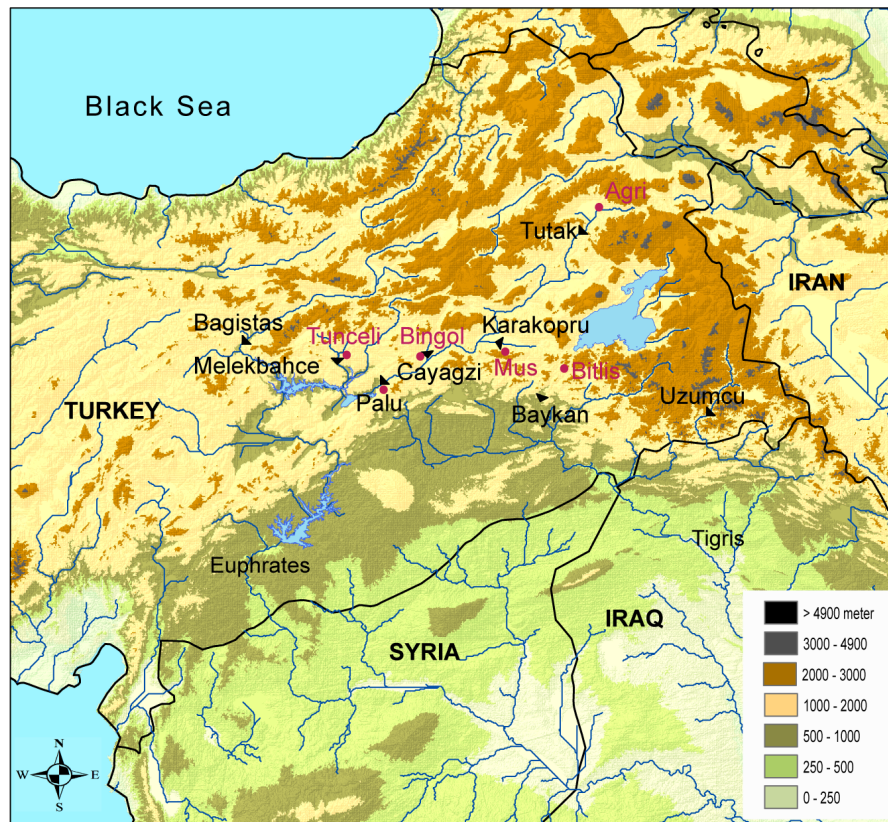
Figure 3.3 : Locations of the streamflow gauging (triangles) and climate stations (red full circles) analyzed in observed climate changes.

Table 3.1 : Information about the streamflow gauging stations used in the study (Note: E: Euphrates and T: Tigris).

Station No.	Name	Latitude	Longitude	Altitude (Basin average) [Highest elevation] (m)	Drainage area (km^2)	Mean annual flow (m^3/s) [b]	Median annual flow (m^3/s) [b]	Fraction of MAMJ[c] discharge (%)	Center Time Date
2102	E. - Palu	38°41`18``	39°55`52``	852 (1856) [4032]	25515	242.75	230.11	77	Apr 18
2122	E. - Tutak	39°32`19``	42°46`49``	1552 (2142) [3505]	5882	48.24	47.35	79	Apr 26
2133	E. - Melekbahçe	39°02`45``	39°31`34``	875 (1861) [3338]	3284	85.72	87.73	64	Apr 28
2156	E. - Bağıştaş	39°26`05``	38°27`04``	865 (1937) [3530]	15562	148.95	150.16	58	Apr 26
2157	E. - Karaköprü	38°47`02``	41°29`43``	1250 (1636) [2919]	2173	25.14	23.17	77	Apr 8
2164	E. - Çayağzı	38°48`31``	40°33`17``	990 (1753) [2824]	2232	33.43	31.75	79	Apr 11
2610	T. - Baykan	38°09`41``	41°46`57``	910 (1620) [2601]	640	18.22	17.48	70	Apr 8
2620	T. - Üzümcü	37°29`11``	43°33`56``	1072 (2420) [3894]	5270	58.80	58.35	72	May 8

[a] Station number used in General Directorate of Electrical Power Resources Survey and Development Administration in Turkey.

[b] Mean and median monthly flows and center time dates are calculated for the period 1972 -2006.

[c] MAMJ stands for March, April, May and June

E: Euphrates

T: Tigris

In addition to CT methodology, which provides a time-integrated view of the changes in the streamflow, daily and monthly differences in the streamflow averages between two periods were provided in order to show when the changes actually occur. In the second part of the analysis, the NCEP/NCAR reanalysis data was used (surface temperature, 10 m wind fields, 850 hPa level temperature, and 500 hPa level temperature and wind fields) to investigate the changes in the large-scale surface and atmospheric fields that may be related to the striking increase in the discharges at the beginning of the major spring pulse in the second period.

3.2 Analyses and Results

3.2.1 Temperature

Figure 3.4 shows time series and the MK trend analysis of CRU-based annual maximum, mean and minimum temperature in the highlands of the basin for the period of 1961-2002 (see Figure 2.3 for the highlands and lowlands of the basin). The time series were formed bu averaging the CRU stations within the highlands, and then the MK test was applied to the time series (see Figure 3.1 for the CRU stations distributed in the basin).
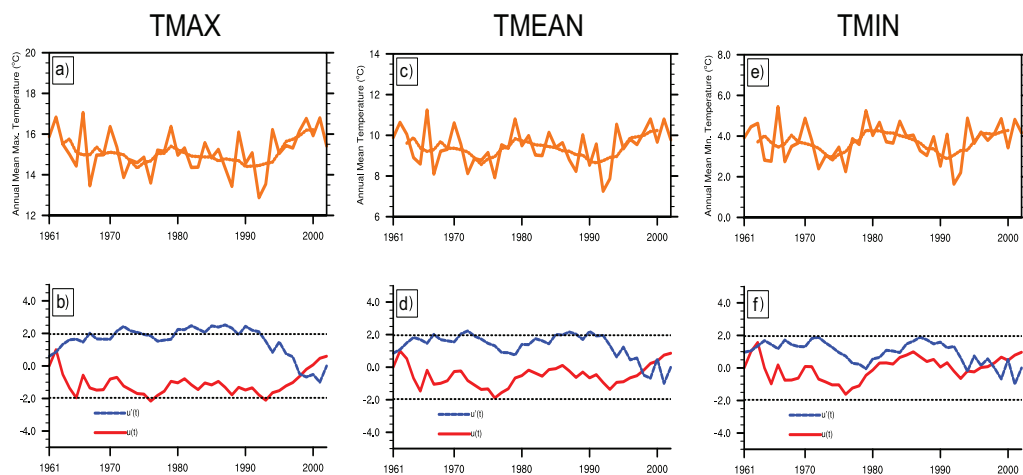
Figure 3.4 : Averaged ime series and Mann-Kendall trend analysis of CRU-based annual maximum, mean and minimum temperature (^{o}C) in the highlands for the period of 1961-2002.

After filtering Ranges of annual maximum, mean and minumum temperatures are between 14-16 ^{o}C, 8-10 ^{o}C, 2-4 ^{o}C, respectively. There is a stkriking warming period beginning from the early 1990s, which is not statistically significant. However, although the CRU dataset is treated as the primary observational dataset to assess the

observed climate changes, this dataset might have poor representation of main climate variables over the mountainous region. Therefore, in addition to trend analysis of the CRU dataset, a regional dataset of TSMS which has relatively dense network over the mountainous region was used. Figure 3.5 demonstrates time series and the MK trend analysis of the TSMS stations in the main headwaters of the basin (see Figure 3.2 for the TSMS stations distributed in the main headwaters of the basin). The most striking point is that warming period beginning from the early 1990s has lead to statistically significant warming trend in the main headwaters region, which is more pronounced for minimum temperature (Figure 3.5f). This is crucially important because the snow-covered mountans are dominated over the main headwaters of the basin and statistically warming trend especially in the minimum temperature in that region may have profound implications for the snow cover and runoff.
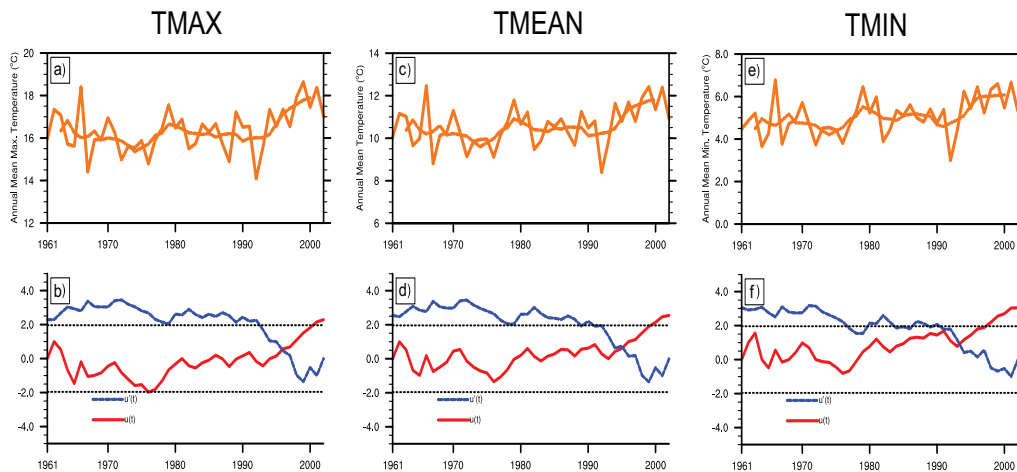
Figure 3.5 : Averaged ime series and Mann-Kendall trend analysis of annual maximum, mean and minimum temperature (^{o}C) of Turkish State Meteorological Service stations in the main headwaters of the basin for the period of 1961-2002.

Figure 3.6 demonstrates time series and the MK trend analysis of CRU-based annual maximum, mean and minimum temperature in the lowlands of the basin for the period of 1961-2002. Annual maximum, mean and minumum temperatures for the lowlands range between 26-29 ^{o}C, 19-21 ^{o}C, 12-14 ^{o}C, respectively. As it is observed in highlands temperature, annual maximum, mean and minimum temperature in the lowlands indicate a striking warming in recent years, which are statistically significant for the mean and minimum temperatures (Figure 3.6d, f).

22
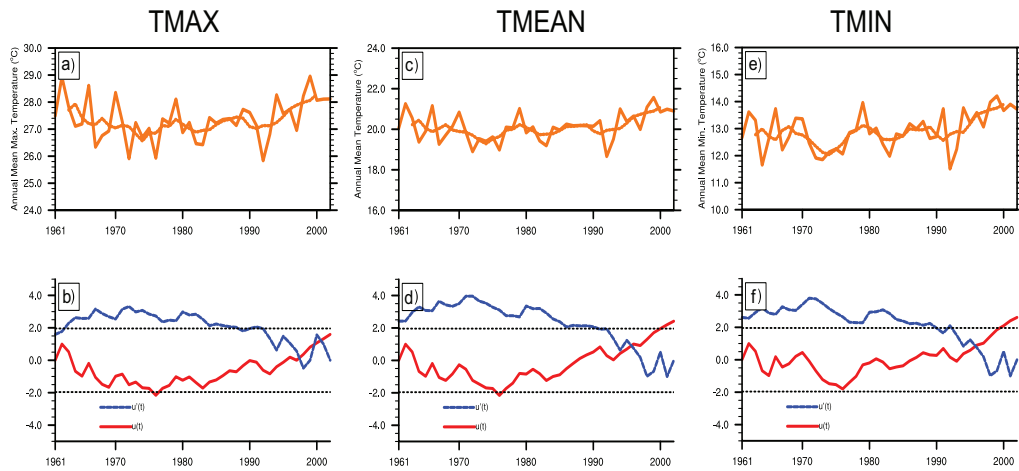
Figure 3.6 : Averaged time series and Mann-Kendall trend analysis of CRU-based annual maximum, mean and minimum temperature (^{o}C) in the lowlands for the period of 1961-2002.

3.2.2 Precipitation

Figure 3.7 shows time series and the MK trend analysis of CRU-based annual precipitation in the highlands and lowlands of the basin for the period of 1961-2002. Annual precipitation amount is higher in the highlands because of high elevation and orography. Annual precipitation amount for the highlands ranges between 500 and 800 mm, while it ranges between 200 and 400 mm for the lowlands. MK trend analysis indicates no statistically significant changes in precipitation for both highlands and lowlands. MK trend analysis of the TSMS stations for precipitation in the main headwaters of the basin also indicates no statistically significant changes.
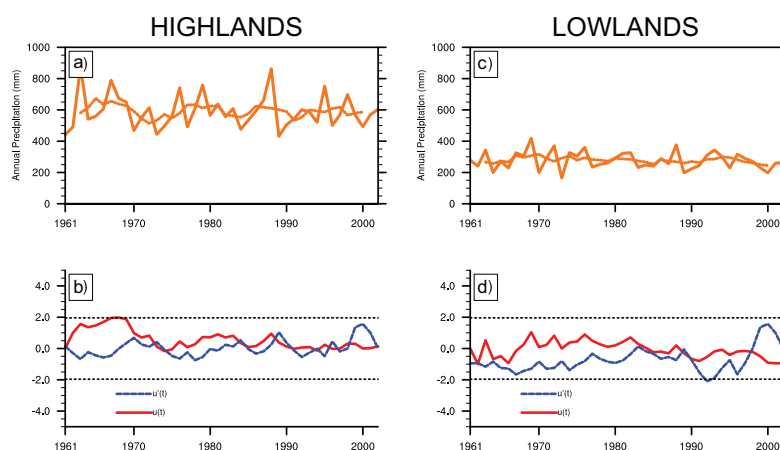
Figure 3.7 : Averaged time series and Mann-Kendall trend analysis of CRU-based annual precipitation (mm) in the highlands and lowlands for the period of 1961-2002.

23

3.2.3 Streamflow

Monthly discharges of all stations between 1972 and 2006, which indicate year-to-year variability in peak discharges, are given in Figure 3.8a. Monthly streamflow fraction (monthly streamflow over annual streamflow) and air temperature averages from the first period (1972-1988) and the changes in these variables in the second period are presented in Figures 3.8b through 3.8e.
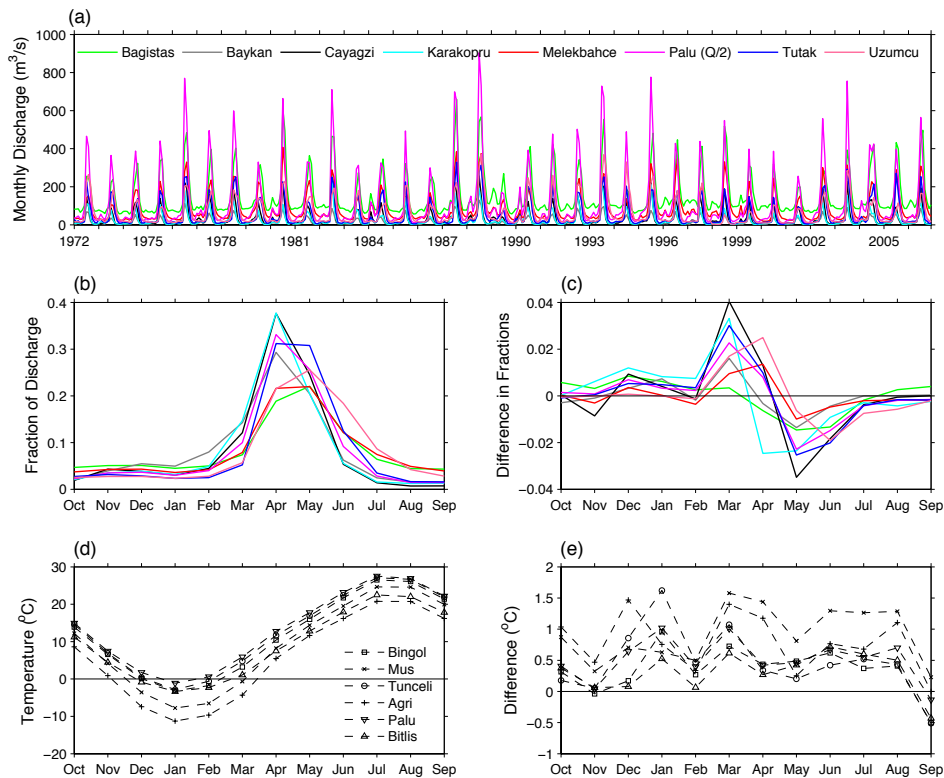
Figure 3.8 : (a) Monthly discharges (m^3/s) from the eight stations halves shown for Palu). Monthly averages of the hydroclimatic variables for the first period [1972-1988] and the changes in the second period (i.e., [1990-2006] minus [1972-1988]) (b) Streamflow fraction (monthly streamflow over annual streamflow), (c) change in streamflow fraction, (d) air temperature (^{o}C), and (e) change in air temperature (^{o}C).

All the rivers show the typical snowfed river characteristics (Figure 3.8b). The monthly fractions of the river discharges indicate that significant melting starts in March, and ends in June and July. Majority of the peaks occur in April with 20-40% of the annual discharge. The peaks of Uzumcu and Bagistas, however, take place in May. The difference plot (Figure 3.8c) shows increases mostly occurring in March while decreases mostly happening in May, balancing each other. Monthly average temperatures (Figure 3.8d) are usually near or below 0 ^{o}C at all meteorological

24

stations in December, January and February. March seems to be the transition month from below-zero to above-zero temperatures in the region. The monthly differences between the temperatures of the two periods indicate consistent warming in almost all months (Figure 3.8e). There are substantial increases in winter temperatures (up to 1.7 °C), but they are probably not adequate to raise the temperatures over zero in large areas in the region. On the other hand, the increases in March (ranging from 0.5 °C to 1.7 °C) seem to be adequate to expose large lower-elevation areas in the basins to positive temperatures.

The significance of the changes in the annual flows using the same methodology applied to the CT data. As can be seen in Table 3.2, differences between two periods (1972-1988 and 1990-2006) are not significant at a significance level of 0.1 which suggests that there are no statistically significant changes in the annual flow data. The differences in CTs of both periods are also provided in Table 3.2 along with the significance test results. Except for Baykan and Melekbahce, differences in CTs are found to be statistically significant at a significance level of 0.1. Among significant sites, the average shift in the CT is 5.2 days. The longest shifts are calculated for Karakopru on Euphrates and Uzumcu on Tigris (both 6.8 days). The 4.8-day shift in Palu whose drainage area is the largest amongst the stations is also statistically significant.

Table 3.2 : Differences in annual discharges and Center Times, and their Monte Carlo (MC) probabilities.

Station	Annual Runoff		Center Time	
	Diff* (m^3/s)	MC prob.	Diff* (days)	MC prob.
Palu	8.46	0.63	4.8	0.97
Cayagzi	1.14	0.64	5.8	0.98
Karakopru	0.49	0.56	6.8	0.98
Tutak	1.63	0.64	3.5	0.92
Melekbahce	-0.53	0.46	1.9	0.79
Baykan	0.76	0.62	3.1	0.80
Bagistas	-6.86	0.24	3.5	0.91
Uzumcu	2.03	0.60	6.8	0.99

* Difference of the second period [1990-2006] from the first period [1972-1988]

The differences in daily discharges indicate a noticeable increase in the discharges during the first half of March, and it is observed at all stream gauging sites. Figure 3.9 shows the differences in daily discharges and surface temperatures between two

periods for four station pairs. The stream gauging stations are the Palu and thos of its three sub-basins, and the temperature stations are the nearest ones to the gauging stations. It is clear from the plot that the discharge of the second period increases in the rising limb while decreases in the recession limb of the major spring pulse (Figures 3.9a, c, e and g). The pulse-type increase in the discharges during the first half of March in the second period is intriguing. The daily surface temperature observations from the nearby climate stations indicate mostly increases in the second period (Figures 3.9b, d, f and h).
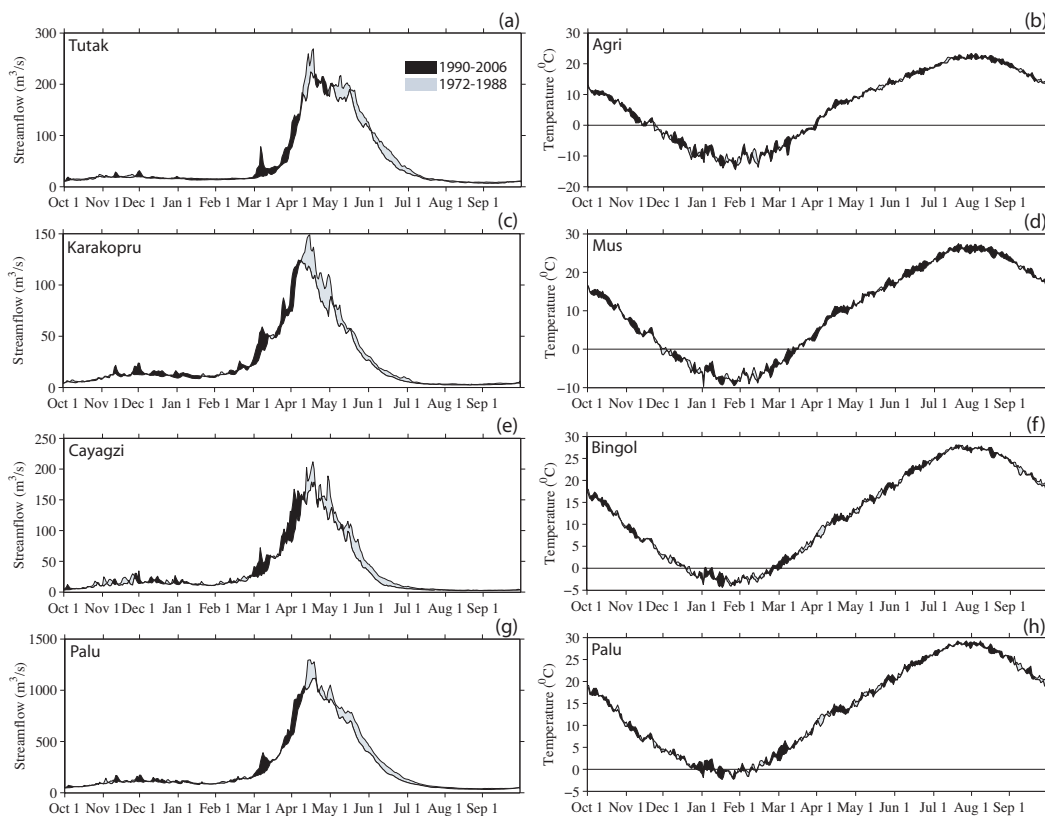
Figure 3.9 : Daily average discharges (m³/s) (left column) and surface temperatures (°C) (right column) from two periods (black shading indicates the excess daily discharge or surface temperature in the second period and the gray shading indicates the excess daily discharge or surface temperature in the first period): (a) for Tutak, (b) for Agri, (c) for Karakopru, (d) for Mus, (e) for Cayagzi, (f) for Bingol, (g) for Palu, and (h) for Palu.

In order to investigate the causes such substantial increases in surface temperatures, average large scale atmospheric fields obtained from the NCEP/NCAR Reanalysis data for both periods were compared for the time period between February 25 and March 5 (Figure 3.10). In the first period (1972-1988), the Siberian High is strong over eastern Europe causing easterly and northeasterly surface winds to blow over

the Black Sea, the Aegean Sea and the western and northeastern parts of the Anatolian Peninsula (Figure 3.10a, c). Typically, the easterly and northeasterly winds carry cold and dry air over these areas (Bozkurt and Sen, 2011). In the second period (1990-2006), the Siberian High weakens over Europe and the sea level pressures over the Anatolian Peninsula increase slightly. The surface winds start to blow from the western to southern directions (i.e. westerly, southwesterly, and southerly winds) over the aforementioned areas in response to the changes in the sea level pressures. At 500 hPa level, the negative heigh anomaly over the Scandinavian Peninsula and positive height anomaly over the eastern Mediterranean-Black Sea region weaken the ridge-trough pattern and result in more westerly flow over Europe and the Mediterranean Sea in the second period (Figure 3.10b, d).
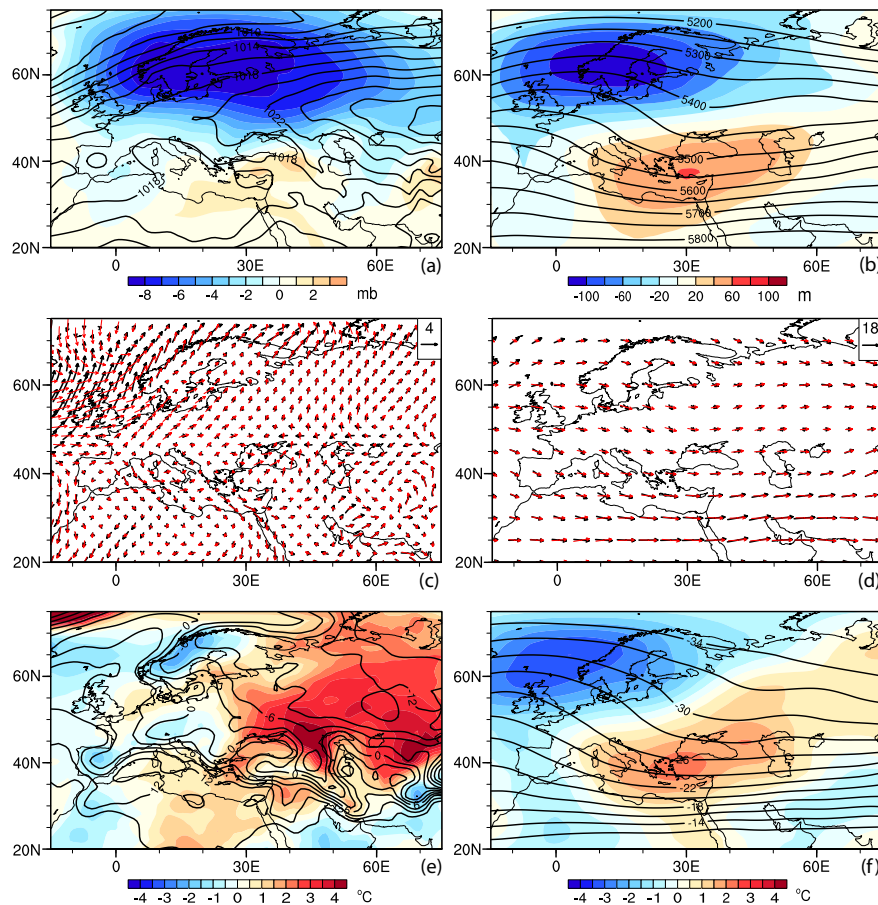
Figure 3.10 : Average (25 February-5 March) large-scale surface and atmospheric fields calculated for the first period (1972-1988) (contours or wind vectors in black) and the changes (i.e. (1990-2006) minus (1972-1988)) (shaded or the wind vectors (in red) in the second period: (a) sea level pressure (hPa), (b) 500 hPa level geopotential height (m), (c) surface wind vectors (m/s), (d) 500 hPa wind vectors (m/s), (e) surface temperature (°C), and (f) 500 hPa level temperature (°C).

Because of its relatively high elevation, eastern Anatolia is subject to negative or near-zero surface temperatures between 25 February and 5 March (Figure 3.10e). In the second period, the surface temperatures increase (up to 2 $^{\circ}$C) over this region. The temperature change at the 500 hPa level reveals a consistent pattern with the geopotential height changes, indicating cooling over a region centered at the Norwegian Sea and warming over a region elongated from the Mediterranean Sea to the northwestern Asia (Figure 3.10f). The largest warming (over 2 $^{\circ}$C), however, occurs over the Aeagean Sea and western Turkey. A time-longitude diagram of 850 hPa temperature differences (i.e. the second period minus the first period) clearly illustrates the propagation of warmer air from over the Balkans and Aegean Sea toward eastern Anatolia after about 25 February (Figure 3.11). The largest warming in the region occurs on the first three days of March.
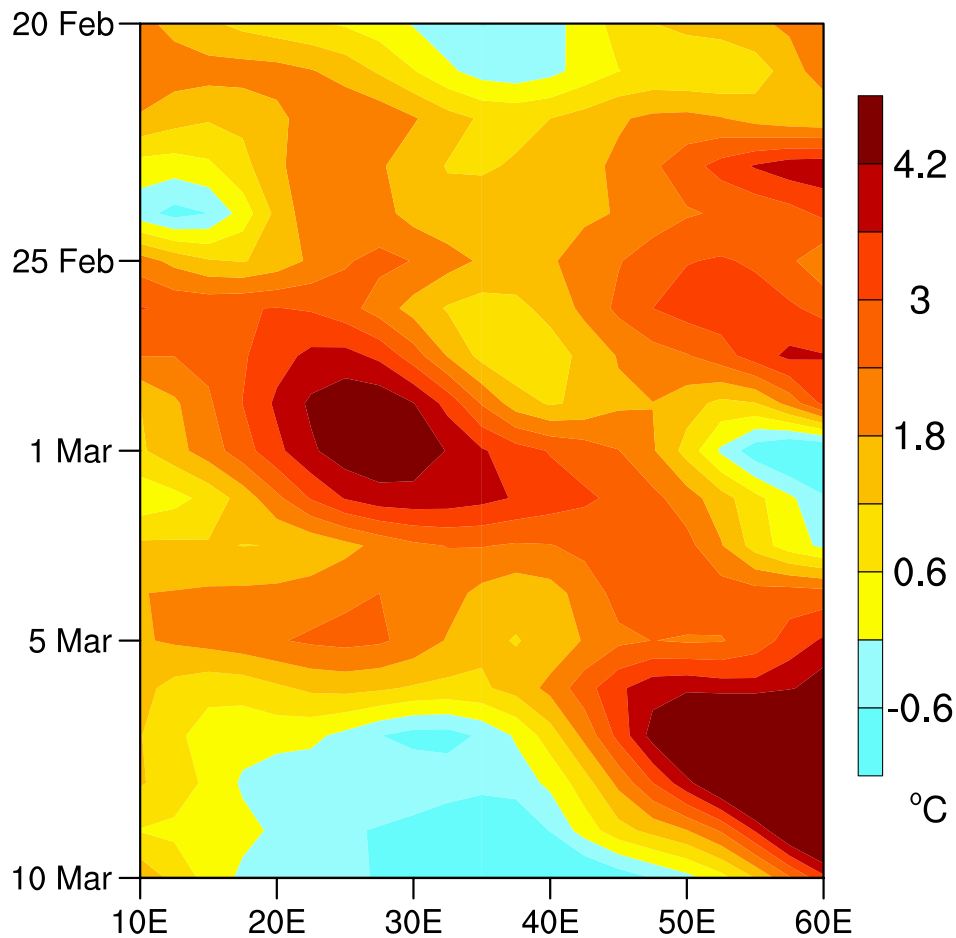
Figure 3.11 : Time-longitude diagram of 850 hPa level temperature difference ($^{\circ}$C) between two periods (i.e. (1990-2006) minus (1972-1988)) along the latitude 39°N, which passes through the headwaters area of the Euphrates Rivers between approximately 40 and 42°E.

It is recognized that the teleconnections may help identify changes in the circulations and the climate characteristics of certain regions in the world. For this reason, the daily values of the NAO and the NCP indices, which are known to influence the climate of Europe and the Mediterranean basin (e.g. Hurrel, 1995; Kutiel and Benaroch, 2002), were analyzed. When the NAO index is positive (i.e. low-pressure anomalies over the Icelandic region and high-pressure anomalies over the subtropical Atlantic), the conditions are wetter and warmer than average over northern Europe and drier and colder than average over the Mediterranean regions (Visbech et al., 2001). Cullen and deMenocal (2000) report that winter temperature and precipitation records in Turkey will reflect a cooler and drier climate during a positive phase of NAO. In the present study, the daily SLP differences obtained using the nearest grid points to Ponta Delgado (37.8° N, 25.7° W), Azores and Reykjavik (64.1° N, 21.9° W), Iceland were standardized using the 1948-2010 climatological daily mean and standard deviation. The NAO index is found to have mostly positive or near-zero values for both periods (Figure 3.12a). It does not show a noteworthy difference between two periods and it most likely has little or no effect on the changes.
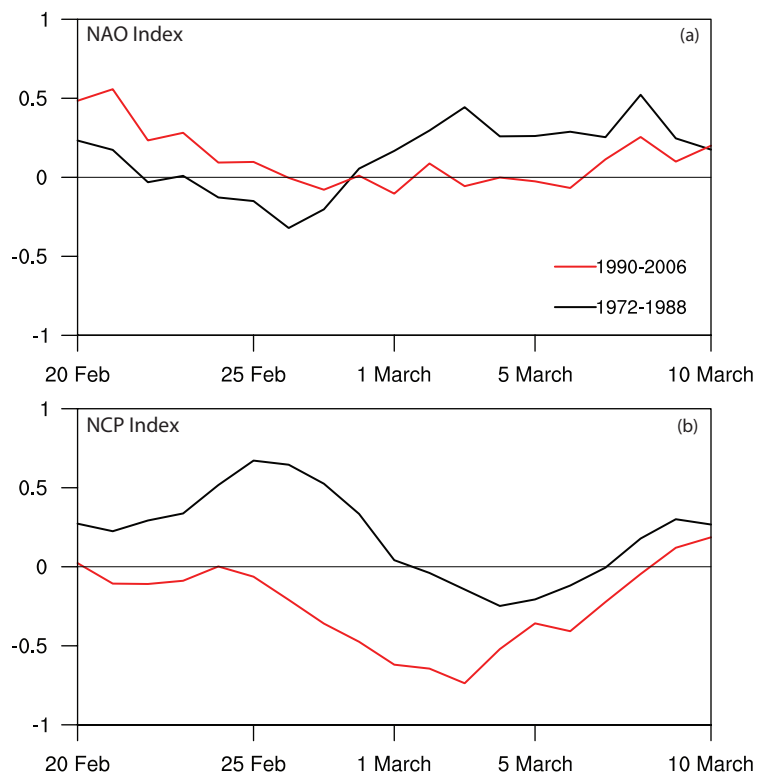
Figure 3.12 : Daily values of the North Atlantic Oscillation index (a) and North-Sea Caspian Pattern index (b).

In general, the positive NCP index implies northeasterly flow toward the Balkans and the western parts of the Anatolian Peninsula, resulting in cooler temperatures, while the negative NCP index implies increased southwesterly anomaly circulation toward these areas, resulting in above normal temperatures (Kutiel and Benaroch, 2002). Kutiel et al. (2002) identifies the continential Anatolian Plateau as the region where the NCEP has the maximum impact on surface temperatures. More recently, Türkeş and Erlat (2009) suggest that extreme phases of the NCP index are more capable than those of the NAO index for explaining the variability in average winter temperatures in Turkey. In the present study, the differences in the average 500 hPa geopotential heights for the boxes of (0°, 55° N; 10° E, 55° N) and (50° E, 45° N; 60° E, 45° N) were calculated, and then, standardized by using the 1948-2010 climatological daily mean and standard deviation. The NCP index tends to have negative values (negative phase) for the days after February 25 in the second period (Figure 3.12b). There are important differences between the index values of both periods. The difference is especially remarkable from 25 February to 4 March. As suggested by Kutiel and Benaroch (2002), the negative NCP index values imply enhanced southwesterly anomaly circulation toward the Anatolian Peninsula resulting in higher surface temperatures there. Therefore, a mostly negative NCP index could be the reason behind the remarkable increase in the early-March snowmelt discharges in the eastern Anatolia in the second period.

4. CLIMATE MODEL SIMULATIONS

In order to determine the second research question of this study (see Figure 1.1), hydro-climatic effects of future climate change in the basin have been investigated using dynamically downscaled outputs of different GCM (ECHAM5, CCSM3 and HadCM3)-emissions scenario (A1FI, A2 and B1) simulations via a regional cliamte model (RegCM3), obtained from a UNDP project (MDG-F 1680) entitled with "Enhancing the capacity of Turkey to adapt to climate change". This chapter of the thesis consists of two parts: (i) Evaluation of the reference period and (ii) The future climate change impact assessments. Evaluation of the reference period was achieved through a compherensive evaluation of the both RCM and GCMs used in this study. The future climate change impact assessments were then achieved through a comparison of the projected climate changes with the corresponding modeled climatology for the reference period. The suite of simulations (total five) enables an analysis taking into account the A2 emission scenario simulations of three different GCMs (ECHAM5, CCSM3 ve HadCM3) and another analysis based on the three different emissions scenario (A1FI, A2 and B1) simulations of one GCM (CCSM3).

4.1 Evaluation of the Reference Period

GCMs are the main tools to generate climate change projections based on emission scenarios. These projections are widely used to study the impacts of the climate change on different components of the climate system at global and continental scales (e.g. Russel et al., 2000; Gregory et al., 2002; Hu and Wu, 2004; Wang, 2005). The GCMs, on the other hand, provide limited information about the climate change impacts at regional and sub-regional scales. This is primarily due to their coarse spatial resolutions, which do not adequately resolve the structure of the earth's surface at these scales (Busuioc et al., 1999). One common procedure for obtaining fine scale regional information is to dynamically downscale the GCM outputs using a RCM. In recent years, the RCMs have been increasingly used in climate change studies (e.g. Giorgi et al., 1994; Huntingford et al., 2003; Giorgi et al., 2004b; Önol

31

and Semazzi, 2009) as well as climate research including diagnostic studies (e.g. McGregor, 1997; Wang et al., 2004) and climate sensitivity studies (e.g. Messager et al., 2004; Martinez-Castro et al., 2006; Sen et al., 2004a; Sen et al., 2004b; Bozkurt and Sen, 2011).

The model-based climate change studies usually include a present-day simulation in addition to a future simulation. The main reasons to have present-day simulations are, first, to demonstrate the performance of the model in comparison with the observations, and second, to have a reference simulation over which the future simulations could be evaluated consistently. Although there is considerable confidence that climate models are capable of representing many important mean climate features, they still harbor uncertainties (IPCC, 2007). Because the RCMs are driven by the GCM outputs, the uncertainties propagate down to the RCM outputs in a regional climate change study. Therefore, a thorough evaluation of GCM outputs on the regional scale together with the performance evaluation of the RCM is needed to provide more reliable and accurate assessments of the regional climate change simulations. Giorgi and Francisco (2000) carried out a comprehensive assessment of uncertainties in regional climate change projections by five-coupled atmosphere-ocean GCMs (AOGCMs) for different anthropogenic forcing scenarios over different regions. They found that intermodel variability with inter-scenario is dominant source of uncertainty in the regional climate change simulations by AOGCMs. They also stated that uncertainties in predicted regional changes by AOGCMs would be transmitted to any regionalization technique used to get fine scale regional information from AOGCMs. Duffy et al. (2006) assessed how well the different RCM/GCM combinations simulate aspects of the present climate in the Western U.S. by using four RCMs and two different GCMs. Their results indicated similar precipitation overestimation in both driving GCM and RCM results, which suggests that the GCMs play a substantial role in regional model precipitation bias. It is also virtually conventional to provide the performance of an RCM that is generally forced by a reanalysis dataset, in order to evaluate the role of the RCM as a source of bias (e.g., Han and Roads, 2004; Sylla et al., 2010). Bergant et al. (2007) stated that an evaluation of an RCM through an investigation of systematic errors in model simulations provides an overview of the model performance in dynamical downscaling studies. Furthermore, an evaluation of an RCM is needed to provide a

valid baseline statistics for the assessment of seasonal predictions and climate change scenarios simulated with RCMs (Seth et al., 2007). Giorgi et al. (2004a) examined climatic means, interannual variability and trends for the 30-year period between 1961 and 1990 with an RCM driven by the Hadley Centre global model (HadAMH). It is stated that the model successfully reproduces not only the basic features of the observed mean surface climate over Europe but also its seasonal evolution.

The eastern Mediterranean - Black Sea region (hereafter EMBS) includes southeastern Europe, Anatolian Peninsula, Caucasus, northeast Africa and the ETB. The fourth assessment report of Intergovernmental Panel on Climate Change (IPCC AR4) highlights the Mediterranean Basin as one of the most vulnerable zones in the world in terms of climate change. Likewise, Giorgi (2006) defined the Mediterranean region as one the most vulnerable climate change "hotspots" in future climate change projections. The GCM simulations largely agree on a basinwide precipitation reduction in the Mediterranean (IPCC, 2007). The RCM simulations, which provide higher detail about the changes, indicate precipitation reductions in the basin as well; however, they also show increases to the north of the basin, which is usually not resolved by the GCMs (e.g., Gao et al., 2006). Within the UNDP project, we have carried out a climate change study that involves the downscaling of the present-day and future simulations of different GCM outputs with different scenarios for the EMBS region. In addition, a reanalysis-data forced simulation with the same RCM for the same present-day period was performed. The subject of the evaluation of the reference period is, therefore, twofold: first to present and evaluate the high-resolution climatology of the dynamically downscaled outputs from three global circulation models, the MPI-ECHAM5, NCAR-CCSM3 and HadCM3; second to demonstrate, for this region, the performance of the RCM (RegCM3), which is used in all downscaling runs of this study.

4.1.1 Model descriptions, data, and experiment design

4.1.1.1 Regional climate model

In this study, RegCM3 of the International Centre for Theoretical Physics in Italy was used. RegCM3 is an upgraded version of RegCM2 (Giorgi et al., 1993a,b), and it is a primitive equation, hydrostatic, compressible, limited area model with sigma-pressure vertical coordinate. RegCM3 includes the land surface model BATS

(Biosphere-Atmosphere Transfer Scheme; Dickinson et al., 1993), the non-local boundary layer scheme of Holtslag et al. (1990), the radiative transfer package of CCM3 (Community Climate Model Version 3; Kiehl et al., 1996), the ocean surface flux parameterization of Zeng et al. (1998), a simplified version of the explicit moisture scheme of Hsie et al. (1984), a large-scale cloud and precipitation scheme which accounts for the sub-grid scale variability of clouds (Pal et al., 2000), and several options for cumulus convection (Anthes, 1977; Grell, 1993; Emanuel and Zivkovic-Rothman, 1999). Grell (1993) with Fritsch and Chappell (1980) closure was selected as cumulus convection scheme for the model simulations. Brief descriptions of the main physical schemes used in the RegCM3 are given below. More detailed descriptions of physical parameterizations and model dynamics of the RegCM3 model can be found in Pal et al. (2007).

Radiation scheme

The radiation scheme of the RegCM3 is the same as that of the NCAR-CCM3. δ-Eddington approximation (Kiehl et al., 1996) is used for solar radiation component that accounts for the effect of O_3, H_2O, CO_2, and O_2. The cloud scattering and absorption parameterizations are also included in order to determine cloud influence on solar radiation. The infrared calculation accounts for effect of CO_2, H_2O, O_3 gases.

Land surface model

The interactions between the soil, vegetation, and atmosphere are parameterized using BATS1e, which is described in detail by Dickinson et al. (1993). BATS describe the role of vegetation and interactive soil moisture in modifying the surface-atmosphere exchanges of momentum, energy, and water vapor (Figure 4.1). 20 vegetation types are avaliable in the present version.

For the water content of the soil layers the soil hydrology calculations are performed. The soil hydrology calculations include predictive equations accounted for precipitation, snowmelt, canopy foliage drip, evapotranspiration, surface runoff, infiltration below the root zone, and diffusive exchange of water between soil layers for the water content of the soil layers. The near surface turbulent fluxes of sensible heat, moisture, and momentum are calculated using a standard surface drag coefficient formulation based on surface-layer similarity theory. The atmospheric

stability in the surface layer and the surface roughness length are the factors that affect the drag coefficient.
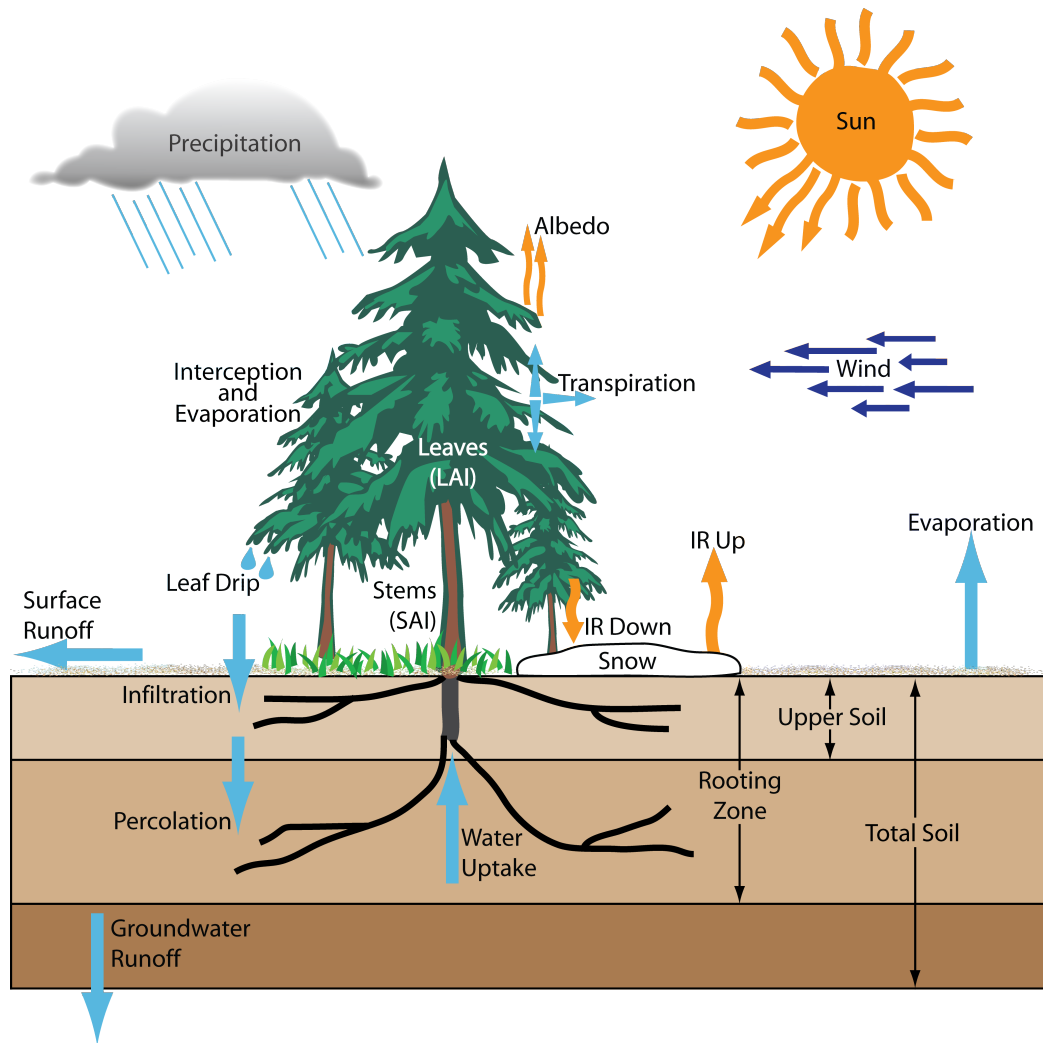
Figure 4.1 : Representation of BATS (Url-2).

Planetary boundary layer scheme

The planetary boundary layer (PBL) scheme of Holtslag et al. (1990) is the scheme used in the RegCM3 model. The scheme is used for calculation of turbulent transports of sensible heat, momentum, and water vapor in the PBL over land and ocean. The PBL scheme is based on non-local diffusion that takes into account countergradient fluxes resulting from large-scale eddies in an unstable, well-mixed atmosphere. Refer to Holtslag et al. (1990) and Holtslag and Boville (1993) for a more detailed description.

Convective precipitation scheme

There are three convective schemes in order to compute convective precipitation: Grell scheme (Grell, 1993), Modified-Kuo scheme (Anthes, 1977), and MIT-Emanuel scheme (Emanuel, 1991; Emanuel and Zivkovic-Rothman, 1999). Grell's cumulus convection parameterization is used as convective precipitation scheme in this study. In this scheme, clouds are defined as two steady state circulations; an updraft and a downdraft. There is no direct mixing between the cloudy air and the environmental air except at the top and bottom of the circulations.

The Grell scheme convective closure assumption can be of two typess. In the Fritsch and Chappell (1980) closure assumption (FC80) convection removes the avaliable buoyant energy at a given time scale. It is designed to represent convections which typically occur in mid-latitudes. In the Arakawa and Schubert (1974) closure assumption (AS74) convection stabilizes the environment as fast as the large-scale destabilizes it. It is designed to represent convections which tend to be the most common form of convection.

Large-scale precipitation scheme

The subgrid explicit moisture scheme (SUBEX) developed by Pal et al. (2000) is used as large-scale precipitation scheme in RegCM3. SUBEX considers the subgrid variability in clouds by linking the average grid cell relative humidity to the cloud fraction and cloud water following the work of Sundqvist (1989). For a more detailed description and formulation of SUBEX refer to Pal et al. (2000).

Model structure

Figure 4.2 demonstrates the schematic representation of the model structure. RegCM3 is mainly composed of two parts: pre-processing and post-processing. In pre-processing part, it is necessary to complete two steps before performing the model. In the first step, the domain with grid intervals is defined and landuse and elevation data are interpolated to the model grids, which are carried out in "Terrain" part. The landuse and elevation data from a latitude-longitude grid to the cartesian grid of the chosen domain are horizontally interpolated by the Terrain program. The elevation data is used from the United States Geological Survey (USGS). Both the landuse and elevation data files are available at 60, 30, 10, 5, 3, and 2 minute resolutions. In this study, the topography and land use are interpolated to the model grids from a global dataset at 10 minute resolution.

Land cover and vegetation classes of the domain are important for determining atmospheric properties of the domain. Atmospheric paramteres such as temperature, precipitation and moisture are affected by not only the topography of the domain but also land cover of the domain. The Global Land Cover Characterization (GLCC) datasets are used for the vegetation/landuse data. The GLCC dataset is derived from 1 km Advanced Very High Resolution Radiometer (AVHRR) data spanning April 1992 through March 1993, for the 20 types of vegetation/landuse data.
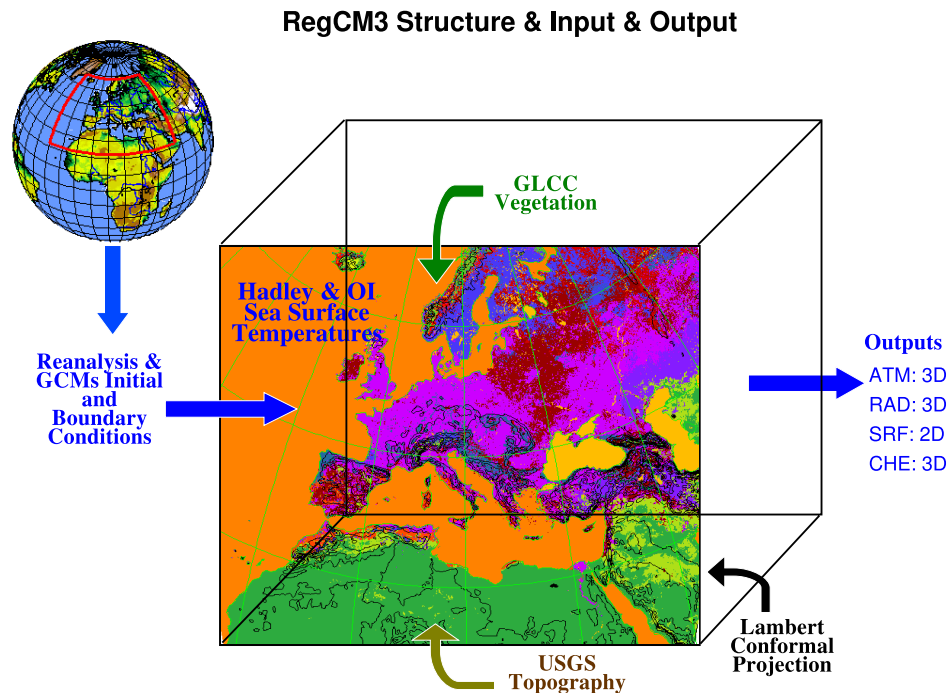
Figure 4.2 : Structure of RegCM3 (Figure adopted from Önol, 2007).

In the second step, the initial and boundary condition (ICBC) program interpolates global reanalysis data or GCM outputs and SST data into the RegCM3 grid. The available options for SST data are: the Global Sea Surface Temperature (GISST; 1871-2002; monthly mean) data from the Hadley Centre, UK and the Optimum Interpolation Sea Surface Temperature (OISST; 1981-2005; weekly and monthly) from the National Ocean and Atmosphere Administration, USA. For the ICBC fields, several reanalysis datasets (NCEP-NCAR, ERA40, ECMWF) and GCM outputs (ECHAM, HadCM, fvGCM, CCSM etc.) can be used in the RegCM3. The boundary condition data files are prepared for every at 00, 06, 12, 18 UTC, and these data are used to up-date model time integration at the lateral boundaries.

Post-processing part of is responsible for producing suitable output files of averaged variables in commonly used formats such as NetCDF or GrADS. Raw outputs of RegCM3 simulations are composed of four types: atmospheric (ATM, 3-dimensional: westerly and southerly wind, air temperature, geopotential height etc.), radiation (RAD, 3-dimensional: solar radiation, cloud cover etc.), surface (SRF, 2-dimensional: precipitation, 2-m temperature, evapotranspiration, etc.) and chemistry (CHE, 3-dimensional: surface emission, tracer mixing etc.). The re-analysis and GCM outputs data files used in this study, are described in the next section. These files are used for the initial affected by not only the topography of the domain but also land cover of the domain.

4.1.1.2 GCMs

MPI-ECHAM5

European Centre Hamburg Model version 5 (ECHAM5) is the fifth generation of the ECHAM atmospheric general circulation model, developed at the Max Planck Institute for Meteorology (MPI), Hamburg, Germany. Its development based on a global numerical weather prediction model developed at the ECMWF (Simmons et al., 1989), and since then, it has been continually developed at the MPI.

Main components of the ECHAM5 are briefly described as follows. Detailed information can be found in Roeckener et al. (2003, 2004). The part describing the main components of ECHAM5 is based on the Roeckener et al. (2003, 2004).

ECHAM5 is based on spectral dynamical core. Vertical structure of the model is described by a hybrid coordinate system. The sigma system at the lowest model level gradually transforms into a pressure system in the lower stratosphere. Troposphere-lower stratosphere depth reaches to 10 hPa with a total of either 19 or 31 levels. In the middle atmosphere the computation level reaches to 0.01 hPa with either 39 or 90 levels. A truncated series of spherical harmonics is employed to represent vorticity, divergence, temperature and the logarithm of surface pressure in the horizontal. A flux-form semi-Lagrangian scheme (Lin and Rood, 1996) is used for passive tracer transport, i.e., for the water components (vapor, liquid, solid) and for chemical substances.

Shortwave radiation used in ECHAM5 for calculating radiative transfer of solar energy within the atmosphere (Foquart and Bonnel, 1980) uses the Eddington

approximation for the integration over the zenith and azimuth angles and the delta-Eddington approximation for the reflectivity of a layer. The scheme includes Rayleigh scattering, absorption by water vapor and ozone, both varying in space and time, and $CO_2+N_2O+CO+CH_4+O_2$ as uniformly mixed gases. Interactions between scattering processes and absorption are considered for water vapor and for the uniformly mixed gases, but not for ozone, because gaseous absorption is assumed to dominate in the stratosphere. The computation of transmissivities and reflectivities across a vertical column is split into two separate calculations for the cloud-free part and the cloudy part. The scheme has four spectral bands, one for visible+UV range, and three for the near infrared. The interaction of scattering processes and gaseous absorption is considered only in the near infrared bands. Single scattering properties of clouds have been determined on the basis of Mie calculations using idealized size distributions for both cloud droplets and ice crystals (Rockel et al., 1991).

Longwave radiation scheme in ECHAM5 is based on Rapid Radiative Transfer Model (RRTM) developed by Mlawer et al. (1997). The RRTM scheme computes fluxes in the spectral range 10 cm^{-1} to 3000 cm^{-1}. The computation is organized in 16 spectral bands and includes line absorption by H_2O, CO_2, O_3, CH_4, N_2O, CFC-11, CFC-12 and aerosols. Aerosols are considered in all spectral bands.

In terms of cumulus convection, a mass flux is employed for shallow, mid-level and deep convection (Tiedtke, 1989) with modifications for deep convection according to Nordeng (1994). The scheme is based on steady state equations for mass, heat, moisture, cloud water and momentum for an ensemble of updrafts and downdrafts including turbulent and organized entrainment and detrainment. Turbulent entrainment and detrainment rates are specified differently for the three types of cumulus convection. Organized entrainment (for deep convection only) takes place as inflow of environmental air into the cumulus updraft when the cloud parcels accelerate upwards, that is, when the buoyancy is positive. Organized detrainment occurs where the air parcels decelerate, that is, when the buoyancy becomes negative. Thus, organized entrainment and detrainment is related to cloud activity itself.

The turbulent surface fluxes for momentum, heat and moisture are obtained from bulk transfer relationships involving the difference of the respective model variable

(wind components, potential temperature, humidity) between the surface and the lowest model level (about 30m above ground), the wind velocity at that level and the transfer coefficients. Approximate analytical expressions in terms of roughness length and bulk Richardson number, are employed for momentum and heat, respectively. Over land, the roughness length is a function of subgrid-scale orography and vegetation. Transpiration is limited by stomatal resistance, and bare soil evaporation is limited by the availability of soil water. Above the surface layer the eddy diffusion method is applied.

The surface temperature is obtained from the surface energy balance equation using an implicit coupling scheme that is unconditionally stable and allows to synchroneously calculate the respective prognostic variables and surface fluxes (Schulz et al., 2001). The surface temperature is used as boundary condition to determine the vertical profile within the 5-layer soil model assuming vanishing heat fluxes at the bottom (10m). For snow covered land a mass-weighted mixture of soil and snow is applied to determine the thermal properties. Four reservoirs are defined for the water components: (1) snow at the canopy, (2) snow at the surface, (3) liquid water at the canopy, and (4) soil water. Surface runoff and drainage are obtained from a scheme, which takes into account the heterogeneous distribution of field capacities within a grid-cell (Dümenil and Todini, 1992). For diagnostic purposes and for coupling to an ocean model, a hydrological discharge model is applied (Hagemann and Dümenil-Gates, 2001). A simple scheme is used for calculating the water temperature, ice thickness and ice temperature of lakes. Changes in water level are not considered. The dataset of land surface parameters utilized in ECHAM5 has been compiled by Hagemann (2002) from a global distribution of major ecosystem types that was made available by the U.S. Geological Survey with a basic resolution of 1 km. These parameters are the background albedo of snow-free land (with corrections for the Sahara desert according to satellite data), vegetation effect on roughness length (in addition to that of subgrid-scale orography), fractional vegetation cover, fractional forest cover, leaf area index, plant available and total soil water holding capacity.

NCAR-CCSM3

The Community Climate System Model version 3 (CCSM3) is a coupled model of the atmosphere, ocean, sea ice, and land surface linked through a coupler that exchanges fluxes and state information among these components. It was released in 2004 and information about the model given below is based on Collins et al. (2006a).

The main components of the CCSM3 system are based on: the Community Atmosphere Model version 3 (CAM3) (Collins et al., 2004, 2006b), the Community Land Surface Model version 3 (CLM3) (Oleson et al., 2004; Dickinson et al., 2006), the Community Sea Ice Model version 5 (CSIM5) (Briegleb et al., 2004), and the Parallel Ocean Program version 1.4.3 (POP) (Smith and Gent, 2002).

Atmospheric component of CCSM3 is based upon the Eulerian spectral dynamical core with triangular spectral truncation at 31, 42, and 85 wavenumbers. The zonal resolution at the equator ranges from 3.75^{o} to 1.41^{o} for the T31 and T85 configurations. The vertical structure employs 26 levels with a hybrid terrain-following coordinate. The developed atmospheric core of the CCSM3 system includes signficant changes to the dynamics, cloud and precipitation processes, radiation processes, and treatment of aerosols. The cloud and precipitation processes include separate prognostic treatments of liquid and ice condensate; advection, detrainment, and sedimentation of cloud condensate; and separate treatments of frozen and liquid precipitation (Boville et al., 2006). The radiation scheme includes a generalized treatment of cloud geometrical overlap (Collins et al., 2002a; 2006c). A prescribed distribution of sulfate, soil dust, carbonaceous species, and sea salt derived from a three-dimensional assimilation (Collins, 2001; Rasch et al., 2001) is used to calculate the direct effects tropospheric aerosols on the radiative fluxes and heating rates (Collins et al., 2002b). The corresponding effects of stratospheric volcanic aerosols are parameterized following Ammann et al. (2003). Indirect effects of aerosols on cloud albedo and cloud lifetime are not incorporated in CAM3.

The ocean core employs a dipole grid with a nominal horizontal resolution of 3° or 1°. The vertical dimension is treated using a depth coordinate with 25 levels extending to 4.75 km in the 3° version and 40 levels extending to 5.37 km in the 1° version. The 1° grid has 320 zonal points and 384 meridional points.

The land model is integrated on the same horizontal grid as the atmosphere, although each grid box is further divided into a hierarchy of land units, soil columns, and plant types. There are 10 subsurface soil layers in CLM3. Land units represent the largest spatial patterns of sub-grid heterogeneity and include glaciers, lakes, wetlands, urban areas, and vegetated regions. CLM3 simulates energy and moisture exchanges between land and atmosphere. Radiative transfer, turbulent fluxes, and heat storage in soil are the main processes of the energy exchange between land and atmosphere (Figure 4.3). In addition to this, CLM3 has detailed representation of the hydrologic cycle, including infiltration, runoff, multi-layer snow accumulation and melt, 10-layer soil water, soil evaporation and transpiration (Figure 4.4). The new land model of CCSM3 is based upon a nested subgrid hierarchy of scales representing land units, soil or snow columns, and plant functional types (Bonan et al., 2002; Oleson et al., 2004). CCSM3 includes the effects of competition for water among plant functional types in its standard configuration.
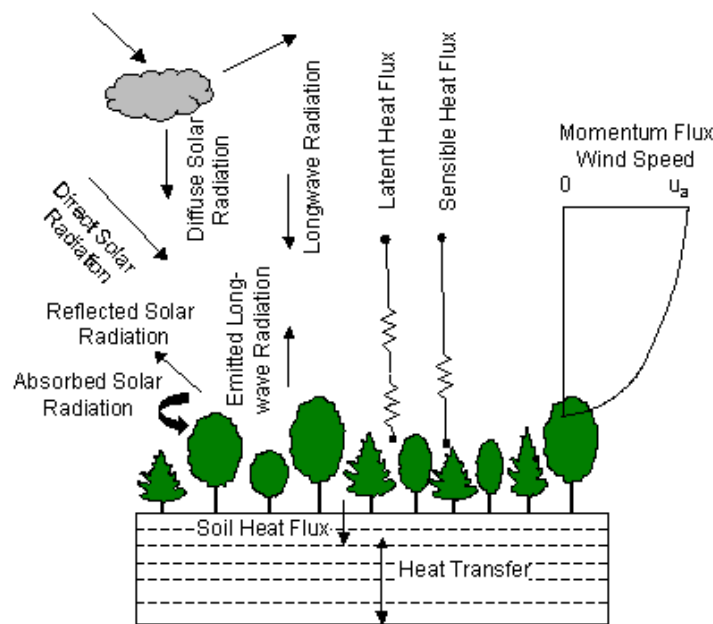
Figure 4.3 : Biogeophysics scheme of CLM3 (Bonan, 2002).

Sea-ice component of CCSM3 includes modifications to the formulation of ice dynamics, sea ice albedos, and exchanges of salt between sea ice and the surrounding ocean. The horizontal advection of sea ice is treated with incremantal remapping (Libscomb and Hunke, 2004). The momentum equation has been modified using scaling arguments to better simulate marginal ice under drift (Connolley et al., 2004).

Salt and freshwater exchange between the sea ice and surrounding ocean are calculated using a nonzero, constant reference salinity of sea ice in CCSM3 (Schmidt et al., 2004). The albedo parameterization in CCSM3 matches observations of the seasonal dependence of the albedo on snow depth, ice thickness, and temperature within the uncertainty of the measurements in the Arctic and Antarctic (Perovich et al., 2002; Brandt et al., 2005).
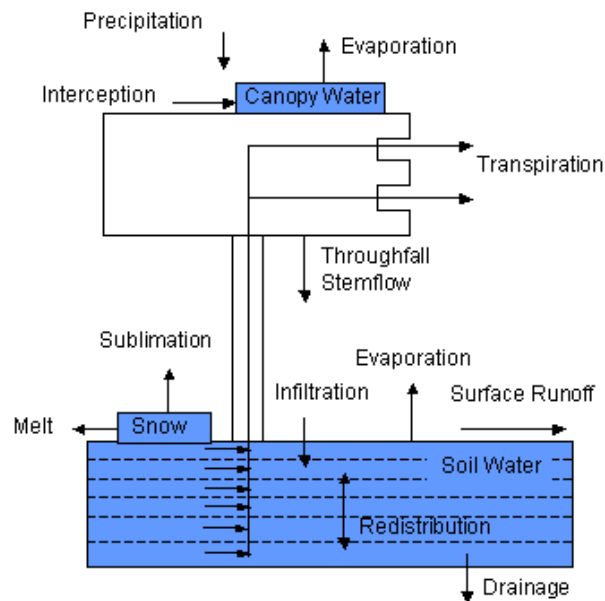
Figure 4.4 : Hydrological cycle in CLM3 (Bonan, 2002).

HadCM3

Hadley Centre Coupled Model version 3 (HadCM3) is a coupled atmosphere- ocean GCM developed at the Hadley Cenre in the United Kingdom. Information about the model given below is based on Gordon et al. (2000).

HadCM3 is composed of two main components: the atmospheric component and the ocean component. Hadley Centre Atmosphere Model version 3 (HadAM3) is a version of the UKMO unified forecast and climate model run with a horizontal resolution of 2.5^o x 3.75^o. The horizontal grid is based on Arakawa-B grid and it has 96 x 73 grid points on the scalar grid (pressure, temperature and moisture); the vector grid is offset by 1/2 a grid box. The vertical structure employs 19 levels with a hybrid vertical coordinate. The radiation scheme consists of two parts, solar (shortwave) and thermal (longwave) (Edwards and Slingo, 1996), using six shortwave bands and eight longwave bands. The radiation scheme includes the

effects of greenhouse gases of H_2O, CO_2, O_3, CH_4, N_2O, CFC-11 and CFC-12. A parameterisation of a simple background aerosol climatology (Cusack et al., 1998) is also included. In the convection scheme, all processes related with heat exchange, updrafts and downdrafts including turbulent and organized entrainment and detrainment are implemented in the convective cloud model, and lead to an increment of the cloud potential temperature. After updating the cloud properties, the scheme finds out the impact on the environment. The expressions for the net change of environmental potential temperature and specific humidity are quite involved and can be found in Gregory and Rowntree (1990). Moreover, the convection scheme has been improved by adding a parametrisation of the direct impact of convection on momentum (Gregory et al., 1997). There are five boundary layer levels and the boundary layer scheme is based on Smith (1993). It determines the transport processes of momentum, latent heat and sensible heat in the lowest atmospheric levels and at the surface. HadCM3 includes a new land surface scheme called MOSES (Met Office Surface Exchange Scheme) (Cox et al., 1998). The land model has T63 resolution, and 6 soil layers (temperature and water/ice). There are 9 soil types and 13 vegetation types (one soil type and one vegetation type per grid point). It includes the representation of the freezing and melting of soil moisture and the formulation of evaporation includes the dependence of stomatal resistance on temperature, vapour pressure and CO_2.

Hadley Centre Ocean Model version 3 (HadOM3) is the core of ocean model in HadCM3. The ocean model has a resolution of 1.25^{o} x 1.25^{o} with 20 levels (Cox, 1984). So, there are six ocean grid points for every atmospheric one and each high latitude ocean grid box can have partial sea ice cover. The vertical levels are distributed to provide enhanced resolution near to the ocean surface and are the same as those in the previous coarser horizontal resolution version of the model (Johns et al., 1997). The topography was taken from the ETOPO5 (1988) $1/12^{o}$ resolution dataset and interpolated onto the model grid. The detailed information about the ocean model can be found in Gordon et al. (2000). The atmosphere and ocean models are coupled once per day. The atmospheric model is run for a day and the fluxes are accumulated each atmospheric model time step. At the end of the day these fluxes are passed to the ocean model and then the ocean model is run for a day. The updated SSTs and sea ice extents are then passed back to the atmospheric model.

4.1.1.3 Data and experiment design

The climate simulations defining the 30-yr climatology between 1961 and 1990 were performed using RegCM3 with lateral boundary conditions derived from one reanalysis dataset - NCEP/NCAR Reanalysis I (Kalnay et al., 1996) - and three different GCMs, IPCC-AR4 simulations of MPI-ECHAM5, NCAR-CCSM3 and HadCM3. The NCEP/NCAR Reanalysis data are available at 6-h intervals with a resolution of 2.5° x 2.5° in the horizontal and 17 pressure levels. The SST data for NCEP/NCAR Reanalysis simulation was prescribed from GISST dataset with a resolution of 1° x 1° (Rayner et al., 2003). Bilinear interpolation method was applied to interpolate the forcing fields horizontally and simple linear interpolation was applied to transfer GCM outputs into the RegCM3 vertical sigma coordinate. Land use and vegetation data were derived from the GLCC data at 10-minute resolution. The properties of input data are given in Table 4.1.

Table 4.1 : Information about the global datasets used in the modeling study.

| Institution | Model | Dataset/Run | SST | Resolution | |
				Spatial	Temporal
NCEP/NCAR	--	Reanalysis I	GISST	T62	6-hour
NCAR	CCSM3	b30.030e	Skin Temp.	T85	6-hour
Max Planck	ECHAM5	EH5.OM.20C.1	Ocean Model	T63/L31	6-hour
Hadley Center	HadCM3	HadAM3P; baseline#1	Ocean Model	2.5°x3.75°	6-hour

The simulations were performed over the EMBS domain with 27 km horizontal resolution resulting in 144 x 100 grid points (Figure 4.5). The number of vertical levels was defined as 18 sigma levels (top of the model at 5 hPa). Due to the extent of the model domain, which has diverse terrain features, five different sub-regions were defined to look into the regional performance of the models (see Figure 4.5). The Fertile Crescent sub-region covers the ETB and it gives a clue about the model performance over the basin. The simulations were performed continuously from 1

45

January 1960 to 31 December 1990. First year of simulations was selected as 'spin-up' period, and thus, discarded in all simulations. For the evaluation of the dynamically downscaled GCM outputs and RegCM3 performance, the simulation results were compared with both the driving fields from NCEP/NCAR Reanalysis data and the gridded datasets of CRU of the University of East Anglia, UK (Mitchell and Jones 2005). The CRU data are available at 0.5^o grid spacing over the land areas only. TSMS climate observations is also used in the analysis. TSMS provided monthly mean temperature and monthly precipitation data from 247 meteorological stations (for the distribution of the stations see Bozkurt and Sen, 2011).
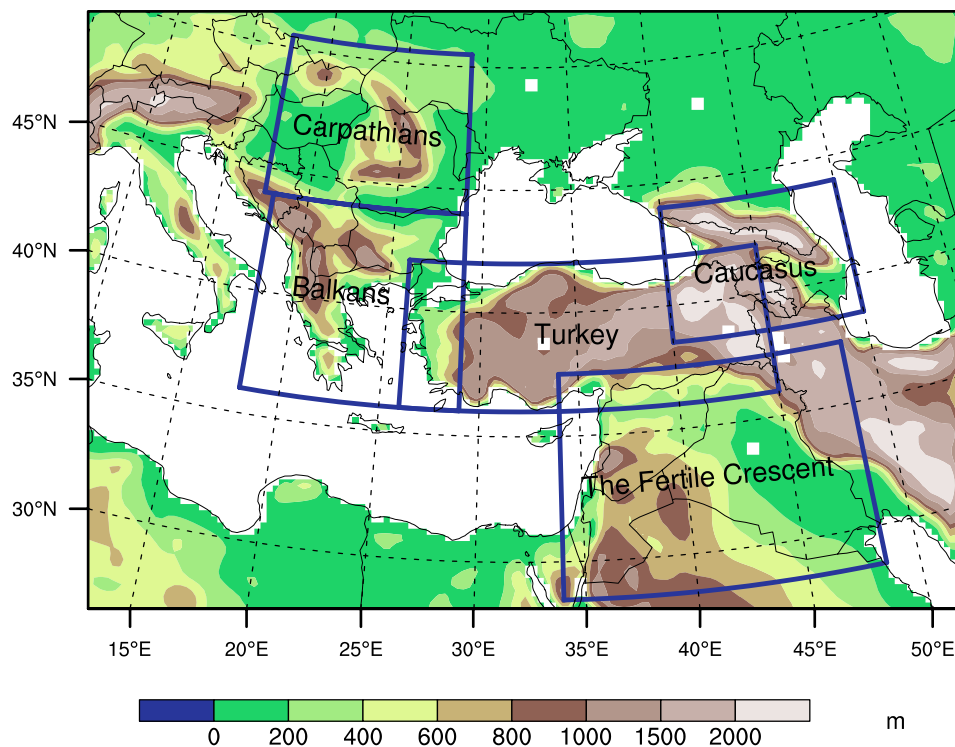
Figure 4.5 : Model domain, topography and sub-regions used in the evaluation.

4.1.2 Results

Results of the evaluation of the reference period was published by Bozkurt et al. (2012). Therefore, the results provided here mainly consist of the analyzes and results in Bozkurt et al. (2012). In this section, climatology of the wet-cold (DJF) and dry-hot (JJA) seasons for large-scale fields of the input data and the model output for the period of 1961-1990 is presented. Wind vectors and specific moisture at 850 hPa are compared in order to assess the ability of the model to simulate typical circulation patterns and moisture fluxes over the domain. Then DJF and JJA comparisons of precipitation and temperature patterns for the entire domain is

presented. For the Fertile Crescent sub-region, area averaged values of all seasons are presented.

4.1.2.1 Low-level wind and moisture

It is conventional to evaluate first the ability of the RCM to simulate the large-scale atmospheric fields so that biases in the regional simulation can be understood well. Figure 4.6 shows the 30-year winter and summer averages of the 850-hPa moisture and wind vectors from NCEP/NCAR Reanalysis (interpolated to RegCM3 grids in the model domain) and the differences in the same fields between downscaled (using RegCM3) and interpolated reanalysis data. In winter (Figure 4.6a), the ETB and its surroundings are under the influence of westerly airflow carrying moisture from the North Atlantic region, and this situation is illustrated in the NCEP/NCAR Reanalysis data. In summer (Figure 4.6b), Azores High and Monsoonal Low extend towards Mediterranean Sea, and thus, their northwesterly winds dominate the air circulation of the 850-hPa level over the basin. The NCEP/NCAR Reanalysis data indicate moister conditions over the highlands of the basin and relatively dryer conditions over the lowlands. The difference plots (Figure 4.6c and d) indicate, in general, that the RegCM3 simulation driven by the reanalysis reproduces consistently the main characteristics of the moisture distribution and wind vectors at 850 hPa for both seasons. The RegCM3 simulation does not generate any domain-wide positive or negative bias in the large-scale fields. However, it tends to yield slightly dryer conditions over eastern Turkey and the ETB in both winter and summer.

It could be said that the major uncertainty in the regional climate modeling comes from the GCMs whose outputs are used to drive the RCMs. It is therefore important to first quantify the differences between the outputs of different GCMs used in a multi-GCM downscaling study. Figure 4.7 illustrates the winter and summer differences in the large-scale fields (i.e., 850-hPa moisture and wind fields) between the three GCMs and NCEP/NCAR Reanalysis by treating the latter as reference. Despite some substantial differences in the large-scale fields, which could cause important differences in the simulated climate parameters, it could be said that the GCM fields broadly agree amongst themselves as well as with the same reanalysis fields. All three models tend to simulate a dryer 850-hPa level over the Middle East,

which covers the ETB, in winter (Figure 4.7a, c, e) and a dryer 850-hPa level for the whole domain in summer (Figure 4.7b, d, f) compared to the reanalysis data.
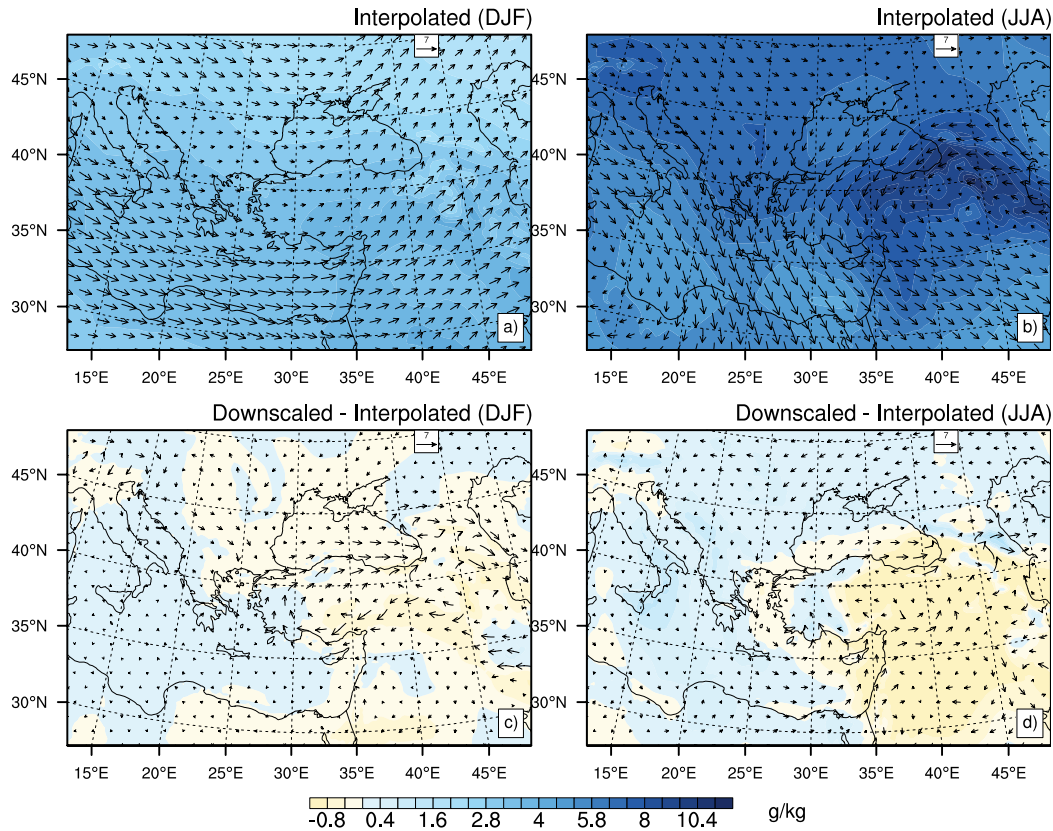
Figure 4.6 : Thirty-year winter (a) and summer (b) averages of the 850-hPa specific moisture (g/kg) and wind vectors (m/s) from NCEP/NCAR Reanalysis (interpolated to the RegCM3 grids), and the winter (c) and summer (d) differences of them from the same fields generated by RegCM3 simulation that is driven by NCEP/NCAR Reanalysis.

4.1.2.2 Surface variables

Precipitation

The EMBS region receives much of the precipitation in winter. Figure 4.8 shows the distribution of 30-year average winter (DJF) precipitation from the dynamically downscaled outputs of NCEP/NCAR Reanalysis, ECHAM5, CCSM3 and HadCM3 together with gridded observation data of CRU. The figure also includes 30-year average winter surface wind vectors from the same RegCM3 simulations. The CRU data illustrate the fact that the western looking sides of the mountain ranges receive more precipitation in the EMBS region (Figure 4.8a). These mountain ranges lift and cool the moisture laden westerly flow and cause orographic precipitation. The NCEP/NCAR Reanalysis simulation produces a similar but more pronounced

precipitation pattern compared to that of CRU (Figure 4.8b). Overall, the RegCM3 simulations driven by GCM outputs agree with the CRU precipitation, but they also generate higher precipitation amounts over mountainous areas in which the ETB is included too as does the reanalysis simulation (Figure 4.8c, d, e). The positive bias could be caused by the insufficient station network, especially in the mountainous regions, resulting in the underestimation of the precipitation for such regions in CRU data as well as by the problems in the model itself. Previous studies (e.g., Önol and Semazzi, 2009; Bozkurt and Sen, 2011) noted the observational deficiency over the complex terrain in Turkey.
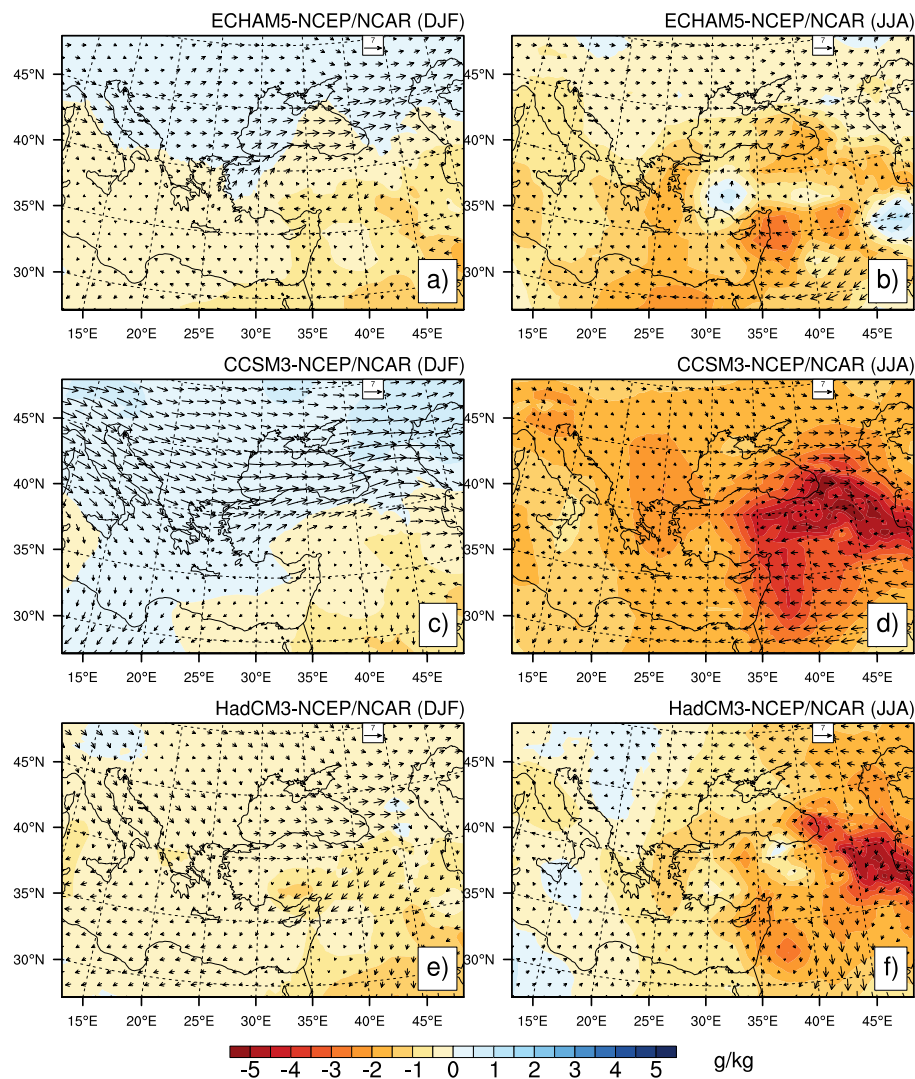
Figure 4.7 : 30-year average differences in the 850-hPa specific moisture (g/kg) and wind vectors (m/s) between GCMs and NCEP/NCAR Reanalysis (all are interpolated to RegCM3 grids). The first row is for the winter (a) and summer (b) differences of ECHAM5, the second row for the winter (c) and summer (d) differences of CCSM3, and the third row for the winter (e) and summer (f) differences of HadCM3.
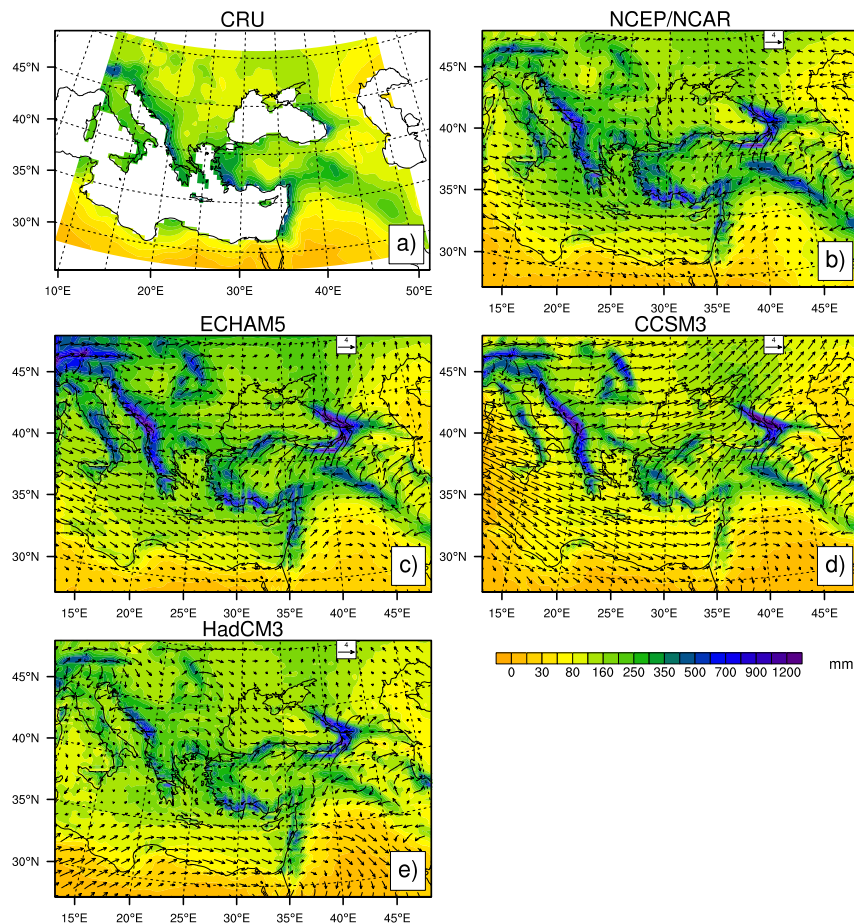
Figure 4.8 : Distribution of 30-year winter precipitation (mm) from the gridded observation data of CRU (a), the dynamically downscaled outputs of NCEP/NCAR Reanalysis (b), ECHAM5 (c), CCSM3 (d) and HadCM3 (e). Also included is 30-year winter average of surface wind vectors (m/s) from the model simulations.

The CRU data indicate relatively wet conditions in the areas in the north of 40°N and dry conditions in the south of this latitude during the summer season (Figure 4.9a). This pattern is fairly well simulated by the reanalysis simulation although it is again more pronounced because of the higher precipitation amounts in the wet areas (Figure 4.9b). The reanalysis simulation demonstrates the prevalence of the northerly winds in most of the domain. Note that the relatively high Anatolian Peninsula (average elevation is around 1000 m) acts like a barrier in front of the northerly flow causing orographic precipitation in the northern sections while dry conditions in the interior and southern parts. Note also that the peninsula divides the northerly airflow into two branches; one blows towards east forming a cyclonic circulation over the eastern Black Sea, which causes abundant precipitation along the mountains of northeastern Turkey and Caucasus, and another one that uses the Aegean Sea as an

easy passage to reach to the eastern parts of the Mediterranean Sea. The precipitation and surface wind fields of the ECHAM5 simulation look substantially like those of the reanalysis simulation (Figure 4.9c). The CCSM3 simulation generates comparatively dry conditions for all over the domain (Figure 4.9d). It should be mentioned that the CCSM3 output of 850 hPa specific humidity that is interpolated to model grids indicates quite dry conditions all over the domain compared to the same field from other models as well as that of reanalysis (see Figure 4.7d). Therefore, the dryness could be related to the poor performance of this GCM in simulating the summer moisture fields in the EMBS region as well as in the ETB. The precipitation pattern yielded by the HadCM3 simulation agrees with that of the CRU, in general (Figure 4.9e). As in the reanalysis and ECHAM5 simulations, it also simulates the wet areas wetter compared to the CRU data.
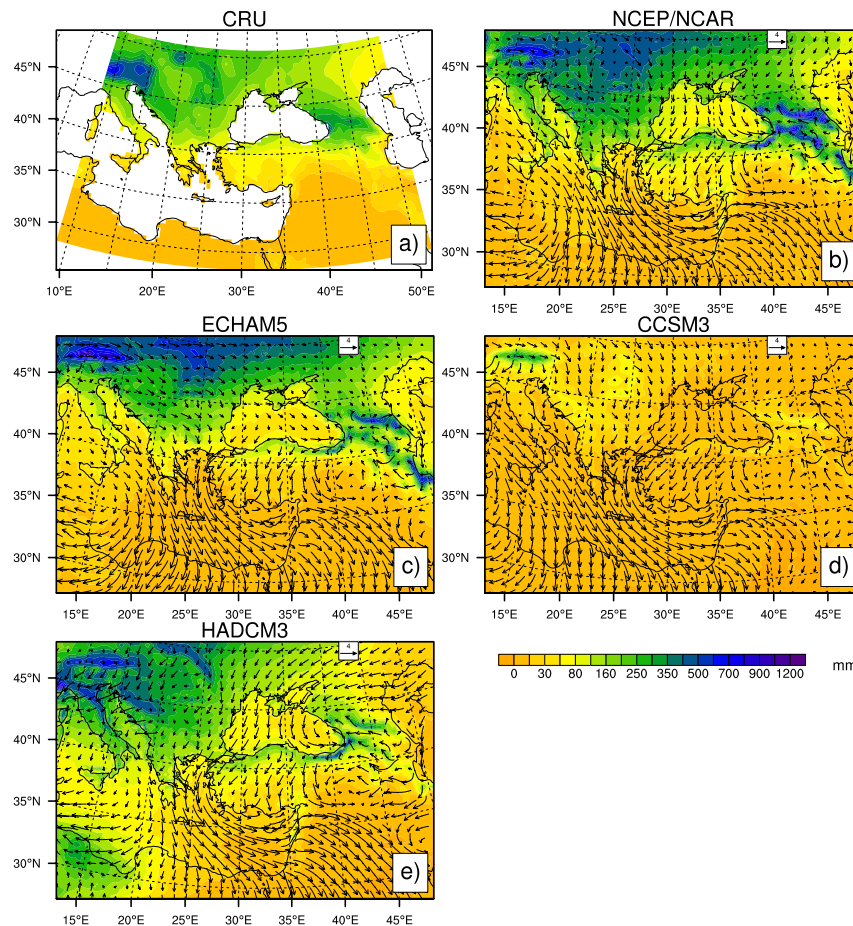
Figure 4.9 : Distribution of 30-year summer precipitation (mm) from the gridded observation data of CRU (a), the dynamically downscaled outputs of NCEP/NCAR Reanalysis (b), ECHAM5 (c), CCSM3 (d) and HadCM3 (e). Also included is 30-year winter average of surface wind vectors (m/s) from the model simulations.

For a more quantitative analysis, the simulated seasonal precipitations for the Fertile-Crescent sub-region with the CRU data (see Figure 4.5 for the sub-regions). Figure 4.10 presents the simulated and observed seasonal precipitations averaged for the Fertile-Crescent sub-region over the 1961-1990 period (the averaging includes only the land grids in the sub-region). The figure also includes the root-mean-square (RMS) differences between the model estimated precipitation and CRU precipitation for the same sub-region. There are seasonality differences between the observed precipitation amounts of the region.
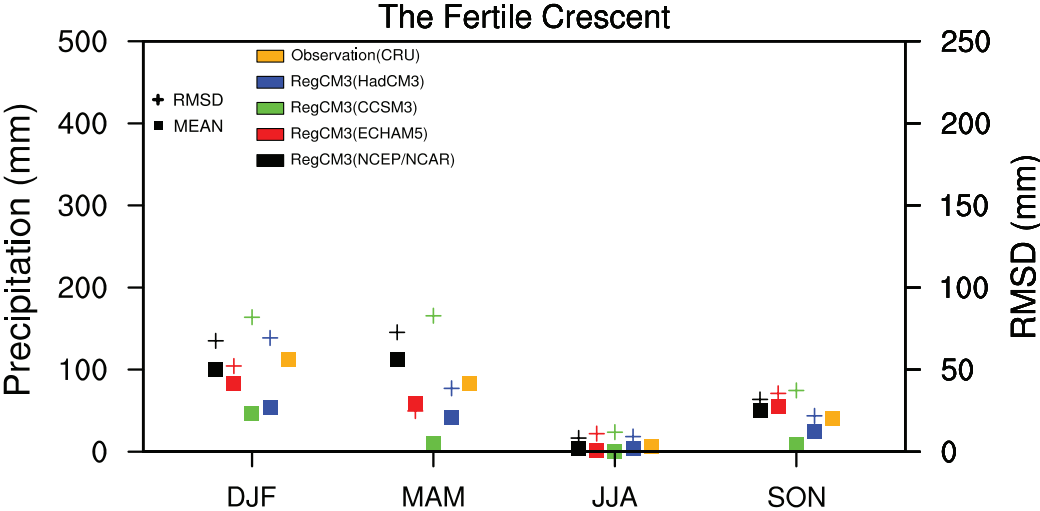
Figure 4.10 : Thirty-year seasonal precipitation (mm) averaged for the Fertile-Crescent sub-region from dynamically downscaled outputs of NCEP/NCAR Reanalysis, ECHAM5, CCSM3 and HadCM3 together with gridded observation data of CRU (full squares). Also shown are the root-mean-square differences (RMSD; mm) for the model estimated precipitations (crosses).

The Fertile Crescent is characterized by winter maximum and summer minimum in precipitation seasonal distribution. The peak seasonal precipitation amount is around 100 mm in the Fertile Crescent. Figure 4.10 clearly shows that the reanalysis simulation tends to overestimate the precipitation in almost all seasons. The overestimation is usually larger in the spring than the other seasons. The seasonal RMS differences in the reanalysis simulation are large in the Fertile Crescent regions. The performance of the two GCM simulations (ECHAM5 and HadCM3) in estimating the seasonal precipitation is mostly comparable for the Fertile Crescent region, and they mostly agree with the reanalysis simulation. The same could be stated for the CCSM3 simulation of winter precipitation. Differing largely from other GCM simulations, however, the CCSM3 simulation tends to underestimate the

precipitation in other seasons. The RMS difference, which is comparatively large, is also an indication of the poor performance of the CCSM3 simulation.

Temperature

The EMBS region region lies in the mid latitudes where atmospheric vortexes carry cold polar air from high latitudes to lower latitudes in winter. Furthermore, the Siberian High occasionally extends towards Europe and brings cold air to the Black Sea region (Bozkurt and Sen, 2011). Figure 4.11 demonstrates the spatial distribution of 30-year average winter temperature (2 meter) from the dynamically downscaled outputs of NCEP/NCAR Reanalysis, ECHAM5, CCSM3 and HadCM3 together with gridded observation data of the CRU.
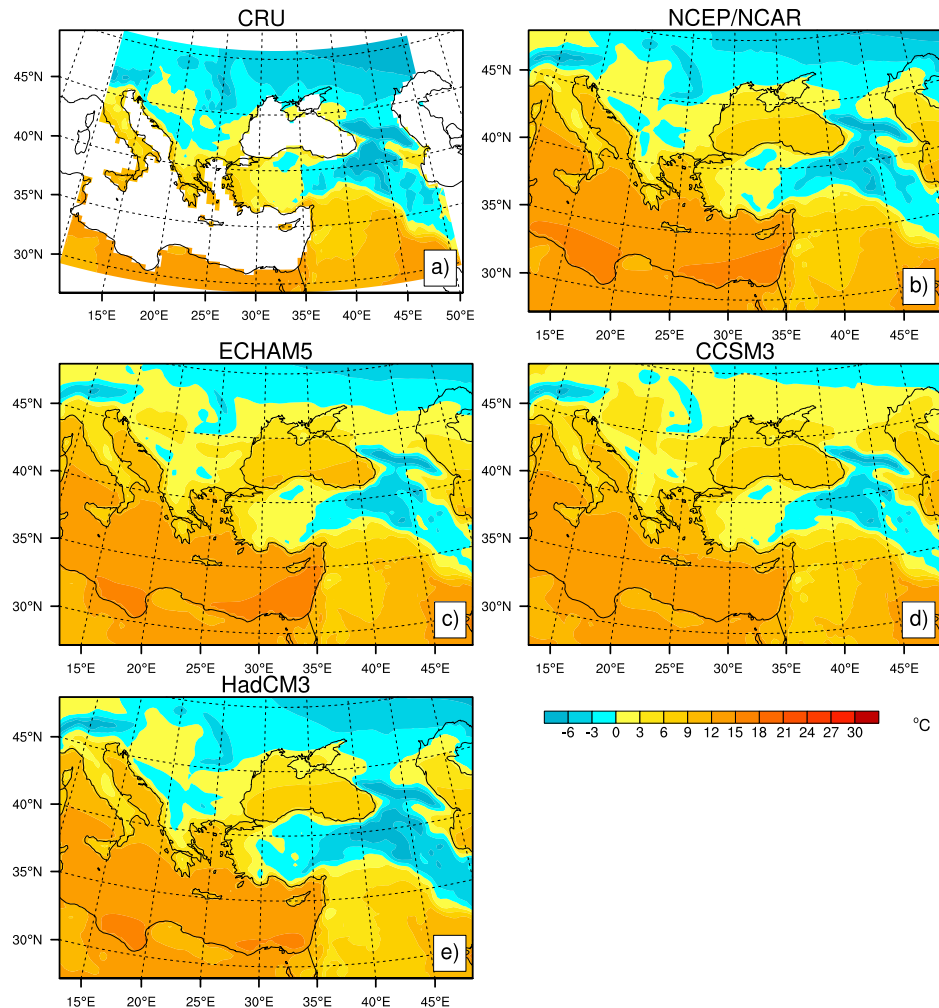
Figure 4.11 : Distribution of 30-year winter temperature (^{o}C) from the gridded observation data of CRU (a), the dynamically downscaled outputs of NCEP/NCAR Reanalysis (b), ECHAM5 (c), CCSM3 (d) and HadCM3 (e).

The average winter temperatures are typically below zero in the north of the 45°N latitude (Figure 4.11a). In addition, they are below zero over the mountainous areas in the ETB. The average winter surface temperatures are between 0 °C and -3 °C in the highlands of the ETB that are usually under the influence of the Siberian High. Average winter temperatures can rise to around 15°C in the lowlands of the ETB. The reanalysis simulation yields a very consistent temperature pattern with the CRU data (Figure 4.11b). Overall, the downscaled simulations of the three GCM outputs capture well the average winter temperature distributions (Figure 4.11c, d, e). Nonetheless, there are noticeable differences between the modeled and observed temperatures. For instance, the ECHAM5 simulation estimates warmer temperatures for the Balkans and the northern parts of the domain. Likewise, the temperature estimations of the CCSM3 simulations are also higher than the gridded observations over the same areas. The HadCM3 simulation yields cooler temperatures over the Anatolian Peninsula and the Zagros region.

In addition to the factors such as the insolation, elevation and the distance from the seas, the circulations related to the Azores High and the Monsoonal Low determine the summer temperature distribution in the EMBS region. Figure 4.12 shows the 30-year average summer temperatures from the model simulations as well as the CRU data. The typical summer temperatures are over 30 °C in the large inland parts of the ETB (Figure 4.12a). Despite its proximity to this area, the highlands of the ETB observes relatively cooler temperatures (usually less than 24 °C) because of its higher elevation. The reanalysis simulation yields a temperature distribution that is highly consistent with that of the CRU data (Figure 4.12b). Despite some differences, the ECHAM5 and HadCM3 simulations agree well with both the CRU data and the reanalysis simulation (Figure 4.12c, d). The CCSM3 simulation captures well the spatial distribution of the summer temperatures, but it has an obvious positive bias throughout the domain, especially over the ETB (Figure 4.12e). This may be related to the comparatively dry conditions in the outputs of the CCSM3 model that are used to drive the RegCM3 simulation.

Figure 4.13 illustrates the simulated and observed seasonal temperatures averaged for the Fertile-Crescent sub-region over the 1961-1990 period. RMS differences between the model estimations and CRU data are also included in the figure. Seasonal cycle of temperature is fairly well simulated by the reanalysis simulation

54

and the seasonal RMS difference is usually low for the reanalysis simulation (between 1°C and 2 $^\circ$C).

The seasonal temperatures estimated by the ECHAM5 simulation are generally in good agreement with those of both the observations and reanalysis simulation. The HadCM3 simulation strikingly underestimates the winter and autumn temperatures. The summer temperature bias for the CCSM3 simulation is remarkable and it is around 4 $^\circ$C. The RMS differences are usually comparable in magnitude for the three GCM downscaling simulations. Few exceptions include the higher RMS difference for summer for the CCSM3 simulation and the higher difference for winter for the HadCM3 simulation in the Fertile Crescent.
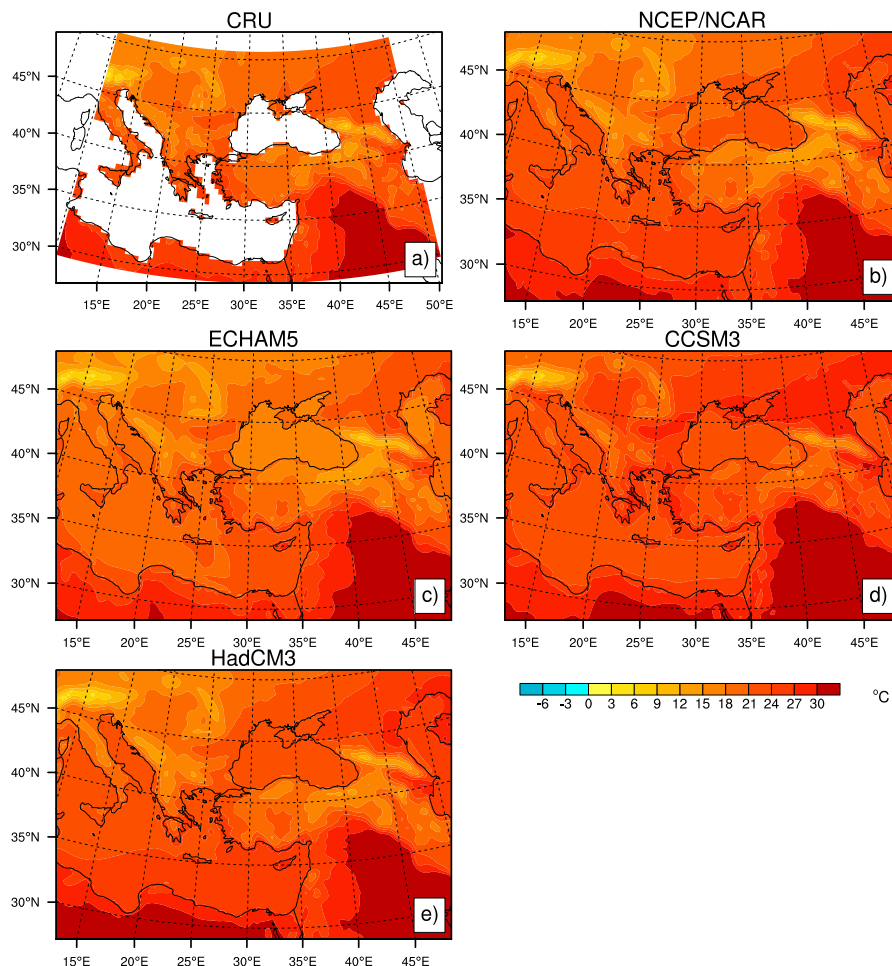
Figure 4.12 : Distribution of 30-year summer temperature ($^\circ$C) from the gridded observation data of CRU (a), the dynamically downscaled outputs of NCEP/NCAR Reanalysis (b), ECHAM5 (c), CCSM3 (d) and HadCM3 (e).
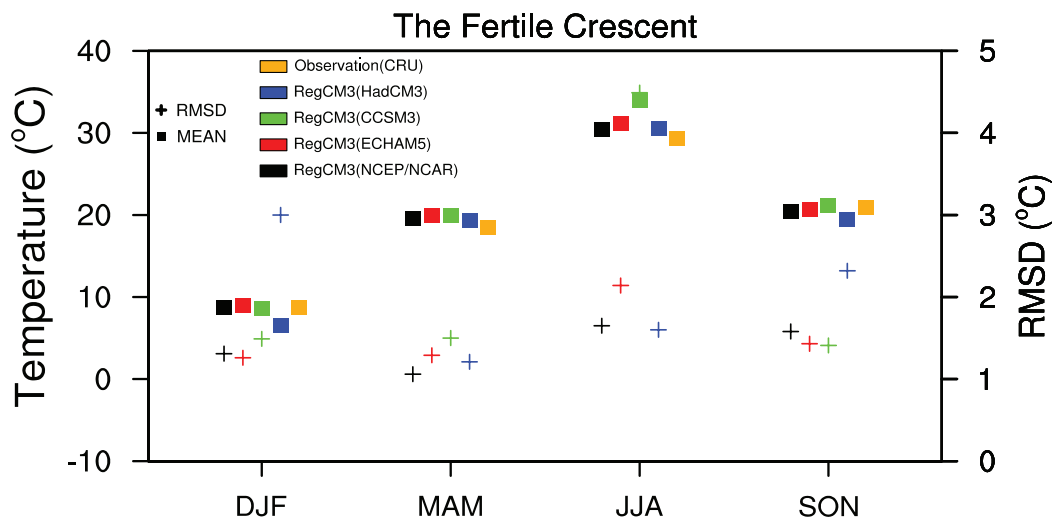
Figure 4.13 : Thirty-year seasonal temperature (^{o}C) averaged for the Fertile-Crescent sub-region from dynamically downscaled outputs of NCEP/NCAR Reanalysis, ECHAM5, CCSM3 and HadCM3 together with gridded observation data of CRU (full squares). Also shown are the root-mean-square differences (RMSD; ^{o}C) for the model estimated precipitations (crosses).

4.2 Hydro-Climatic Effects of Future Climate Change

4.2.1 Approach

After performing a comprehensive reference period evaluation, dynamically downscaled outputs from three GCMs, the MPI-ECHAM5, NCAR-CCSM3 were then used to assess the future hydro-climatic changes in the ETB. Three different GCM simulations (MPI-ECHAM5, NCAR-CCSM3 and HadCM3) based on A2 (mid-high) emissions scenario and three different emissions scenario (A1FI (higher), A2 (mid-high), and B1 (lower)) simulations of one GCM (NCAR CCSM3) (see Table 4.2 for the relevant datasets) were used. Based on the analysis of evaluation of the reference period for all three GCMs, and the performance of RegCM3 in simulating the climatology of the eastern Mediterranean - Black Sea region, including the ETB, it was highlighted that RegCM3 driven by the reanalysis data is able to simulate the precipitation and surface temperature as well as the upper level fields reasonably well. It, however, tends to overestimate the precipitation in the mountainous areas in the region. The evaluation of the reference period further suggests that the RegCM3 simulations forced by the GCM outputs reproduce the

56

regional climate fairly well. Differing largely from other GCM simulations, however, the CCSM3 simulation underestimates the precipitation in seasons other than winter, which is most likely a result of the dryness in the upper levels of the original outputs.

Table 4.2 : Information about the global datasets used in the modeling part.

Institution	Model	Dataset/Run	Emission Scenario	Period
NCEP/NCAR	--	Reanalysis I	Observation	1961-1990
NCAR	CCSM3	b30.030e	Observation	1961-1990
			A2	2001-2099
			A1FI	2001-2099
			B1	2001-2099
Max Planck	ECHAM5	EH5.OM.20C.1	Observation	1961-1990
			A2	2001-2099
HADLEY	HadCM3	HadAM3P:base line#1	Observation	1961-1990
			A2	2071-2099

Scenarios for possible Greenhouse Gases (GHG) such as carbon dioxide, methane and nitrous oxide concentration changes that are based on Special Report on Emissions Scenarios (SRES) are stated in the Third Assessment Report (2000). The SRES scenarios were defined to explore future developments in the global environment with special reference to the production of GHGs. The SRES are composed of four narrative storylines (Figure 4.14), labelled A1, A2, B1 and B2. Each storyline corresponds different social, economic, technological, and environmental developments. The storylines are summarized as follows (Nakicenovic et al., 2000):

- A1 storyline and scenario family: a future world of very rapid economic growth, global population that peaks in mid-century and declines thereafter, and rapid introduction of new and more efficient technologies.
- A2 storyline and scenario family: a very heterogeneous world with continuously increasing global population and regionally oriented economic growth that is more fragmented and slower than in other storylines.
- B1 storyline and scenario family: a convergent world with the same global population as in the A1 storyline but with rapid changes in economic structures toward a service and information economy, with reductions in

material intensity, and the introduction of clean and resource-efficient technologies.

- B2 storyline and scenario family: a world in which the emphasis is on local solutions to economic, social, and environmental sustainability, with continuously increasing population (lower than A2) and intermediate economic development.
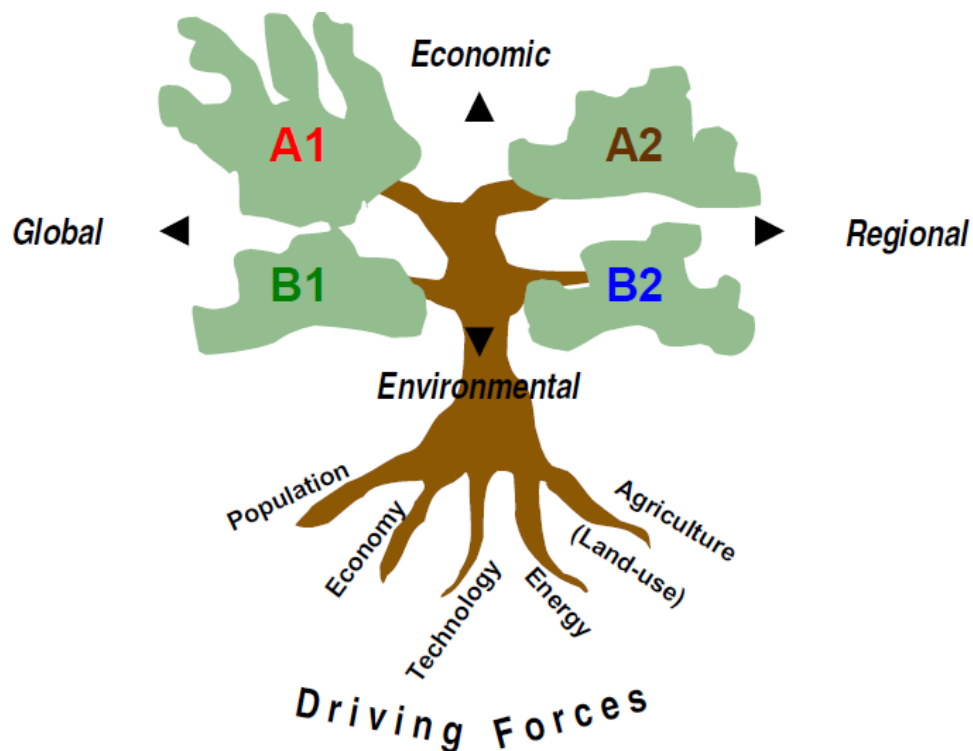
Figure 4.14 : Schematic illustration of the SRES storylines (figure adopted from Nakicenovic et al., 2000).

Different emission scenarios have been applied in various climate models to predict future atmospheric conditions. IPCC (2007) states that the best estimate of projected global average surface warming for the higher scenario (A1FI) is 4.0 $^{\circ}$C (likely range is 2.4 $^{\circ}$C to 6.4 $^{\circ}$C) and for the mid-high scenario (A2) is 3.4 $^{\circ}$C (likely range is 2.0 $^{\circ}$C to 5.4 $^{\circ}$C). The likely range of temperature increase for the lower scenario (B1) is between 1.1 $^{\circ}$C and 2.9 $^{\circ}$C. Figure 4.15 demonstrates the multi-model temperature variability of six different projections from 20th to 21th centuries (IPCC, 2007).

The ETB is investigated in two parts as highlands and lowlands (see Figure 2.3) by mainly considering the elevation differences that depict two primary precipitation regimes. A shapefile including the borders of the ETB was used to identify the

boundaries of the ETB on the elevation map of RegCM3 with a spatial resolution of 27 km. Using the same map, lowlands are classified as the areas where the elevation is below 1000 m and highlands corresponding to the areas where the elevation is greater than 1000 m, mainly constituting the headwaters of the ETB. In addition to the elevation-based analysis, projected changes in the surface runoff are also assessed according to the territories of the four major countries (Iraq, Iran, Syria and Turkey) within the ETB.
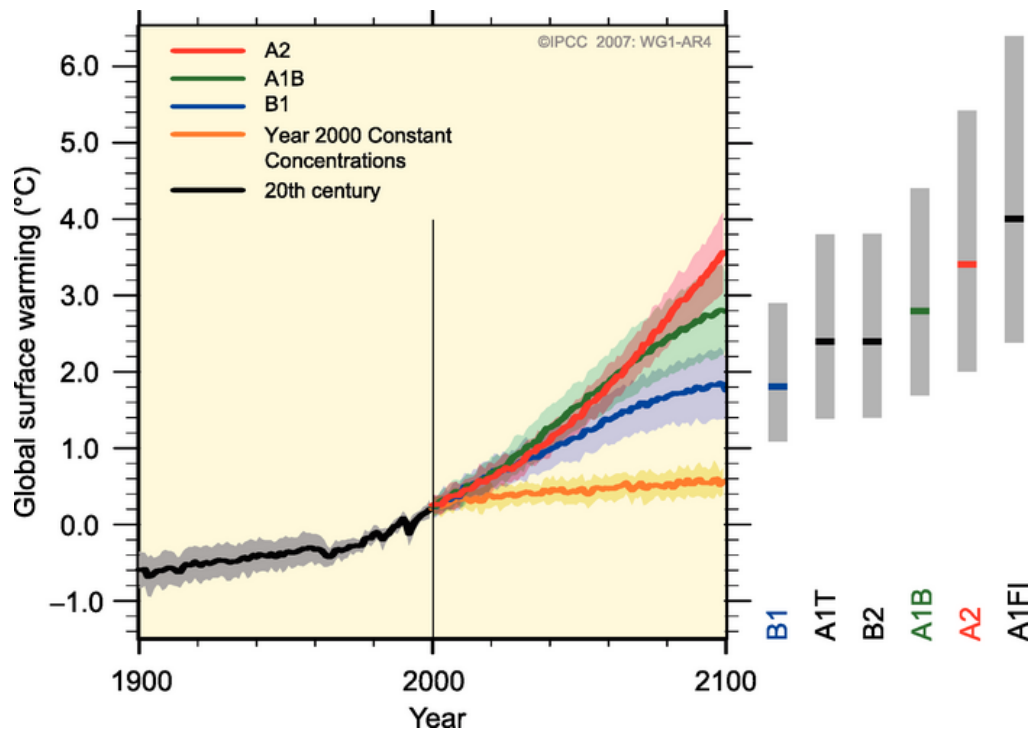
Figure 4.15 : Multi-model global anomalies relative to 1980-1999 mean are shown as solid lines. Shaded areas correspond to one standard deviation range. Four different scenarios are shown in different colors (IPCC, 2007).

4.2.2 Projected climate change scenarios

In this section, hydroclimatic parameters (i.e., surface temperature, precipitation, surface runoff, evapotranspiration, and snow water equivalent (SWE)) from the outputs of the downscaled GCM climate simulations for two 30-year periods, 2041-2070 and 2071-2099 are analyzed. In addition to a spatial analysis, assessments of the changes in these parameters based on elevation (as lowlands and highlands) and countries that have territories in the ETB (i.e., Iraq, Iran, Syria and Turkey) are provided.

4.2.2.1 Spatial changes

Temperature

Increase in winter (DJF) temperatures over the mountainous regions has the potential to impact the regional hydrological cycle leading to snow cover decrease and temporal shifts in snowmelt surface runoff. It could also affect the climate dynamics of the region by perturbing the regional-scale snow-albedo feedbacks. Figure 4.16 shows the projected changes in winter mean surface temperatures of five different simulations for the 2071-2099 period relative to the reference period of 1961-1990.
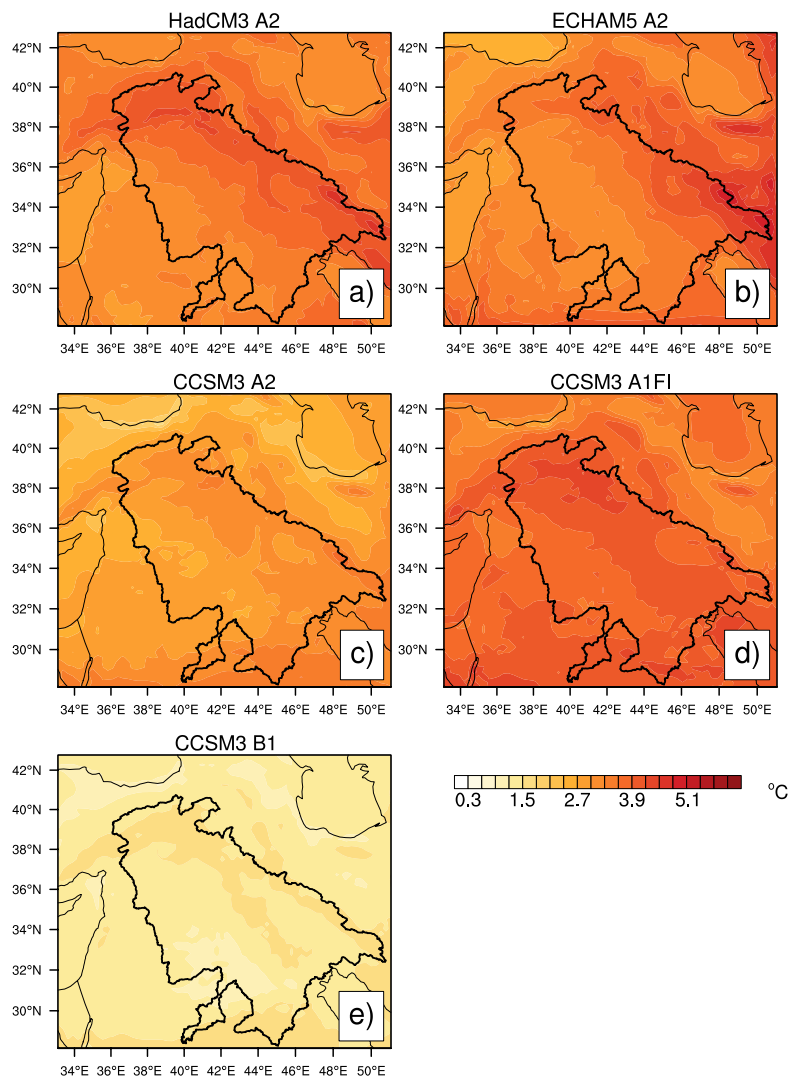
Figure 4.16 : Dynamically downscaled 2-m winter temperature changes (°C) by the end of the century (2071-2099) relative to 1961-1990 reference period for (a) HadCM3 A2 scenario, (b) ECHAM5 A2 scenario, (c) CCSM3 A2 scenario, (d) CCSM3 A1FI scenario and (e) CCSM3 B1 scenario.

Surface temperatures are projected to increase by about 1.5-5 ^{o}C across the entire ETB. It is apparent that the projected temperature changes indicate more warming in the highlands of the ETB. The A2 scenario simulations reveal that the HadCM3 and ECHAM5 simulations yield more pronounced winter warming in the highlands of the ETB with increment values of about 4-4.5 ^{o}C. The increases simulated by CCSM3 for the same scenario have slightly lower values than the other models. The CCSM3 simulations of different scenarios indicate greater increases under A1FI and A2 scenarios compared to B1 scenario in winter temperatures by the end of the century. The A1FI scenario simulation has the greatest increase in winter temperatures, as expected, and the amount of warming is more pronounced in the eastern Anatolian highlands with approximately 4.5 ^{o}C. Projected increase in winter temperatures in the ETB for B1 scenario ranges between 0.9-1.8 ^{o}C by the end of this century. The summer temperatures are usually projected to increase more than the winter temperatures (not shown here). It should be also noted that warm season temperature increases will most likely lead to increases in temperature extremes, by increasing the number of days that fall above the present-day high temperature thresholds for warm temperatures and decreasing the days that fall below cold temperature thresholds (Hayhoe et al., 2007). Indeed, as being influenced by the subtropical high-pressure system during summer that leads to summer dryness in lowlands, the ETB seems to be one of the most vulnerable basins to drought and extreme heat events. For instance, A2 scenario simulation of ECHAM5 indicate substantial increase in the summer largest number of consecutive days when daily maximum temperature is larger than 35 ^{o}C in the lowlands (more than 25 days) by the end of the present century.

Precipitation

Highlands of the ETB receive much of the precipitation in winter season, which falls mostly in the form of snow. During the winter, moisture flux towards the ETB with an airflow moving from west to east over the Mediterranean indicates a greater likelihood of orographic precipitation in the Taurus and Zagros mountain ranges (Evans, 2004). Thus, any change in precipitation in the winter season has a direct impact on the amount of snowpack that stores the water in winter. Figure 4.17 indicates the projected changes in winter precipitation of five different simulations for the 2071-2099 period relative to the 1961-1990 reference period. Statistically

significant changes in precipitation were determined using the Student's t test with 95% confidence level for every model grid for each simulation, and the areas were hatched accordingly. General information for the Student's t test and its algoritgm are provided in Appendix B.
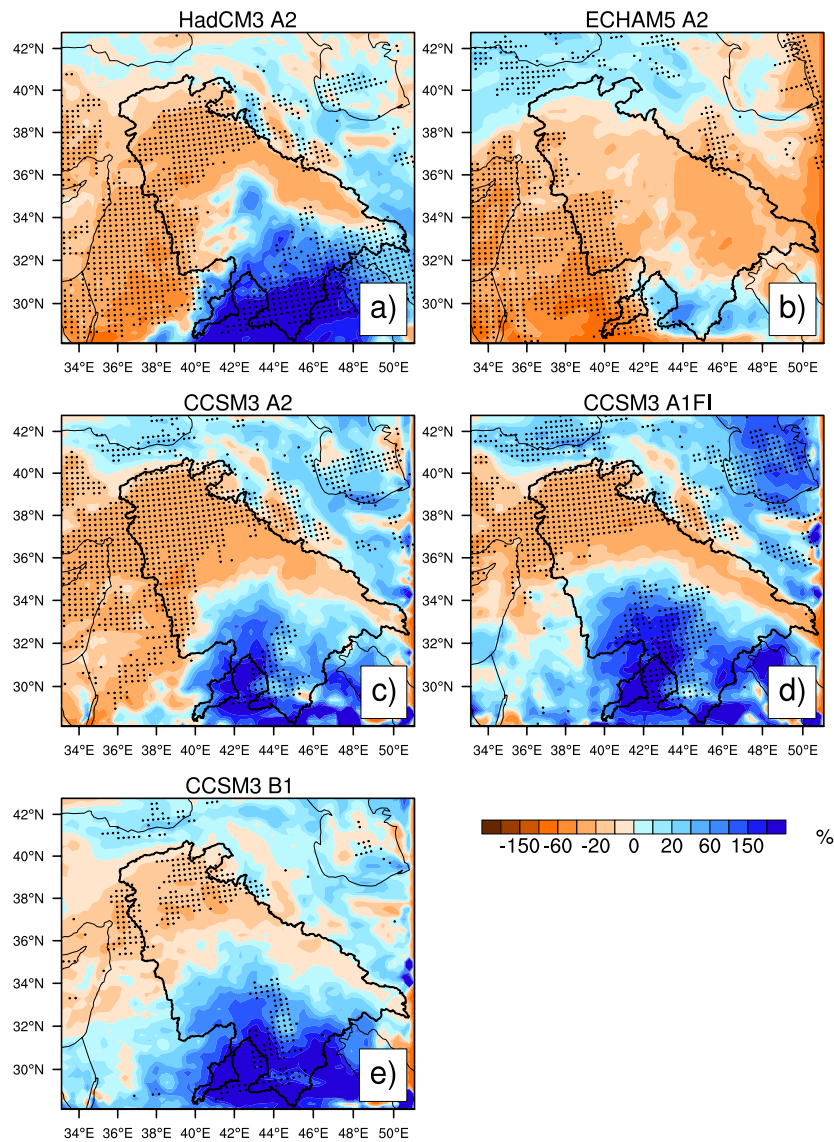
Figure 4.17 : Dynamically downscaled winter precipitation changes (mm) by the end of the century (2071-2099) relative to 1961-1990 reference period for (a) HadCM3 A2 scenario, (b) ECHAM5 A2 scenario, (c) CCSM3 A2 scenario, (d) CCSM3 A1FI scenario and (e) CCSM3 B1 scenario.

In general, there is a broad agreement in the changes among the simulations, which indicate decreases in the precipitation in the highlands and northern parts of the ETB and increases in the southern parts of the basin where the changes are mostly statistically significant in the HadCM3 and CCSM3 simulations. The statistically

significant changes are mostly confined to the western parts of the ETB in the ECHAM5 simulation. By the end of the present century, the winter precipitation is projected to decrease between 20 and 30% in the highlands of the ETB and some parts of the lowlands in the A2 scenario simulations. Precipitation increases in the southern parts of the ETB is more pronounced in the HadCM3 simulation, with high percentage increments (Figure 4.17a). The different scenario simulations of CCSM3 demonstrate similar patterns for the changes in the precipitation, with more pronounced precipitation increases in the southern parts of the ETB under A1FI scenario. Precipitation decreases in the northern parts of the ETB and eastern Anatolian mountains under A2 and A1FI scenarios are about 20%. These changes are mostly significant at 95% confidence level. Lower percentage decrements (between 5 and 20%) with less statistically significant areas are depicted under B1 scenario.

Snow water equivalent (SWE)

Snow cover over the highlands of the ETB plays a key role in the regional hydrological cycle. Majority of the water resources of the basin is fed by snowmelt runoff from the snow-capped eastern Taurus and Zagros mountains. The response of the snow cover to climate warming is, therefore, crucially important to assess the impacts of climate change on the water resources of the ETB. Figure 4.18 shows the projected absolute and relative changes in the winter SWE of five different simulations for 2071-2099 period relative to the reference period of 1961-1990. In terms of absolute changes (mm), each simulation indicates substantial decreases across the eastern Anatolian mountains of Turkey, which majorly constitutes the headwaters of the Euphrates and Tigris Rivers. By the end of the century, according to the A2 scenario simulations, SWE reductions larger than 100 mm are projected to occur in the headwaters of the Euphrates and Tigris rivers. Relative decreases in SWE in the highlands of the ETB are mostly from 70% to 90% in the A2 scenario simulations. The CCSM3 simulation for B1 scenario indicates 30 - 50% decreases in SWE in the mountainous regions. The relative changes (%) at the higher elevations are generally less than those at the lower elevations, which means that higher regions are distinguishably less affected by warming. The SWE reductions in the headwaters of the ETB have a direct impact on the discharges of the Euphrates and Tigris rivers, which will be discussed later. Based on all scenario simulations, it could be said that

the altitudinal gradient of SWE response to climate change will likely result in the disappearance of snow cover at the lower elevations (under 1000 m).
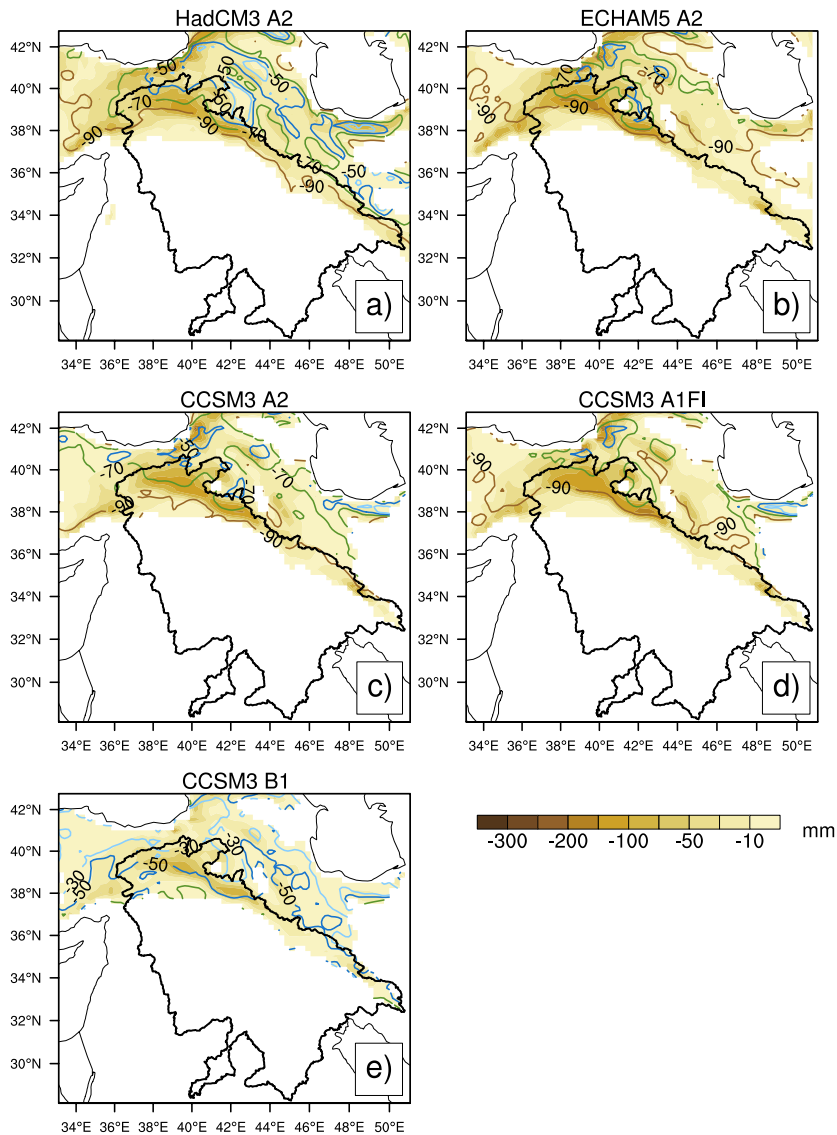
Figure 4.18 : Dynamically downscaled absolute winter snow water equivalent changes (background color pattern; in mm) and relative changes (contour lines; %) by the end of the century (2071-2099) relative to 1961-1990 reference period for (a) HadCM3 A2 scenario, (b) ECHAM5 A2 scenario, (c) CCSM3 A2 scenario, (d) CCSM3 A1FI scenario and (e) CCSM3 B1 scenario.

4.2.2.2 Elevation-based analysis

For a more quantitative assessment, the ETB is investigated in two parts, highlands (> 1,000 m) and lowlands (< 1,000 m), due to marked areal differences in topography and corresponding contrasting features in landscape. Figure 4.19 demonstrates precipitation-temperature cross-plot of the projected annual

64

temperature and precipitation differences of five different simulations for 2071-2099 period relative to the 1961-1990 reference period. The values correspond to the changes of grid-averaged values in the highlands and lowlands (^{o}C for temperature, % for precipitation).
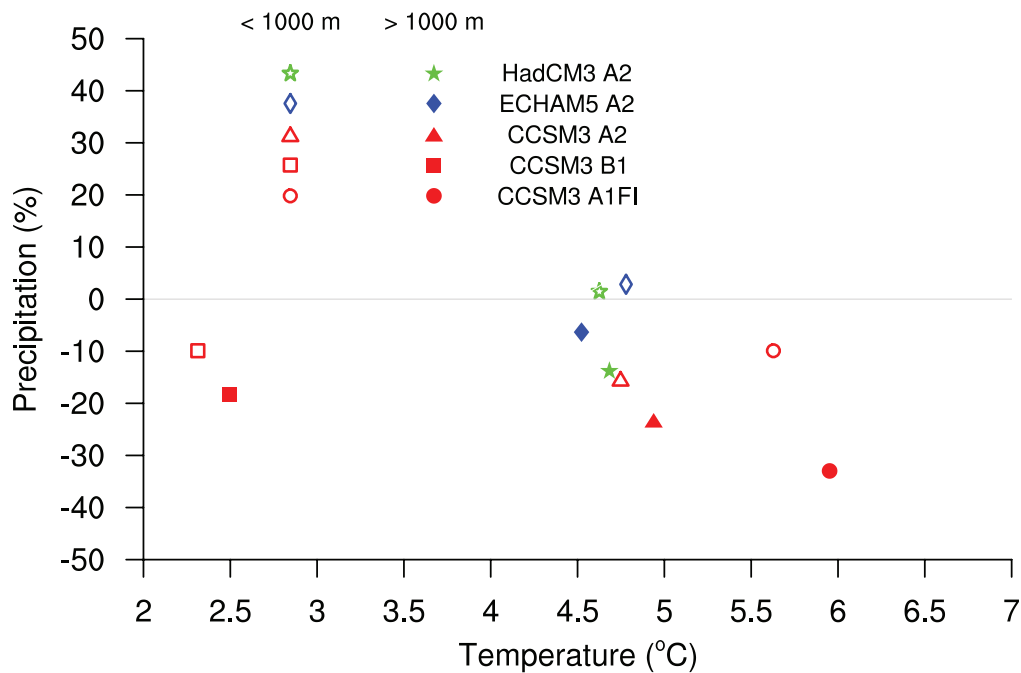
Figure 4.19 : Annual average elevation-based changes in 2-m temperature (°C) and precipitation (%) by the end of the century (2071-2099) relative to the 1961-1990 reference period. Empty markers denote the average values below 1000 m and solid markers denote the average values over 1000 m. Red colors represent different scenario outputs of CCSM3 simulations (triangle for A2 scenario, square for B1 scenario and circle for A1FI scenario). Green star denotes HadCM3 A2 scenario changes and blue quadrilateral denotes ECHAM5 A2 scenario changes.

The A2 scenario simulations indicate a broad agreement in the annual temperature increases in the highlands by the end of the century, with the greatest increment in CCSM3 (5 ^{o}C) and the lowest increment in ECHAM5 (4.5 ^{o}C) (see Table 4.3). The A2 scenario simulations also indicate that temperature increases in the highlands are slightly larger than those in the lowlands, except ECHAM5 simulations. The greatest increases in annual temperature by the end of the century belong to the CCSM3 A1FI simulation with an increment of 6.1 ^{o}C in the highlands (Table 4.3). The CCSM3 simulations depict a 3.5 ^{o}C difference between the A1FI and B1 scenarios in both the highlands and lowlands. In terms of annual precipitation change, one of the most

striking points is that the A2 scenario simulations of ECHAM5 and HadCM3 yield slight increase in precipitation in the lowlands by the end of the century. All the others indicate a consistent decrease in precipitation. In the highlands, the A2 scenario simulations indicate a consistent decrease in precipitation ranging from 6 to 24% (see Table 4.3). The most pronounced decrease in precipitation is demonstrated in the CCSM3 simulations in the highlands (33% for A1FI, 24% for A2 and 18% for B1).

In addition to the projected changes for temperature and precipitation, we look into the changes in the surface runoff timing in the water year as well as in the amount of annual surface runoff in the highlands, especially in the region covering the headwaters of the Euphrates and Tigris Rivers in Turkey. Figure 4.20 shows reference and projected fractions of accumulated surface runoff for the headwaters based on ECHAM5 A2 simulation. Vertical arrows correspond to the days when 50% of annual surface runoff is reached. This methodology, which is analogous to the center time (CT) concept (Stewart et al., 2005), is used to detect the shifts in the surface runoff timing. Note that the surface runoff is not routed to the basin outlet.
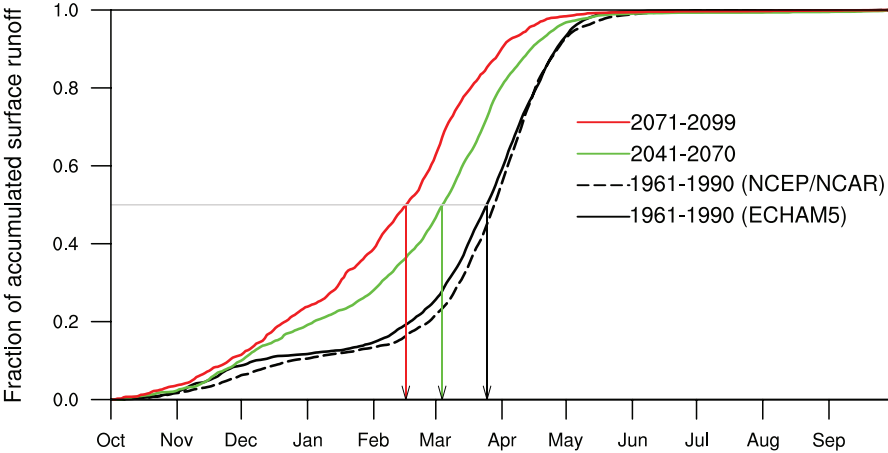
Figure 4.20 : Long-term area averaged fraction of accumulated surface runoff in the headwaters of the Euphrates and Tigris Rivers in the eastern Anatolia mountains of Turkey. Black solid line denotes the fractions in reference period (1961-1990) of the ECHAM5 simulation, and black dashed line denotes the NCEP/NCAR Reanalysis simulation for the same period. Projected future fractions are shown with green and red lines for the periods of 2041-2070 and 2071-2099, respectively. Vertical arrows correspond the days when 50% of annual surface runoff is reached.

For the reference period, fraction of the accumulated surface runoff is in good agreement with that of reanalysis simulation. CT date of the reference period is marked as the 24th of March. Projected fractions for the 2041-2070 period indicate a shift to the 4th of March. As the increase in temperature is more pronounced by the end of the century, which means earlier melting of snow, the temporal change is found to be 38 days corresponding to the 14th of February (temporal changes are found to be between 18 days (B1 scenario) and 39 days (A1FI scenario) in the other simulations). It should be also noted that these changes are statistically significant at 95% confidence level based on the Student's t test. Figure 4.21 illustrates the average annual surface runoff from the ECHAM5 simulations for the same region. The model simulates an average annual total surface runoff of 228 mm for the reference period, and it is clearly seen that the annual surface runoff is projected to decrease in both future periods. The reduction is more pronounced in the last period, with a statistically significant reduction of about 25% (all other simulations also indicate reduction in the annual surface runoff ranging from 35 to 55%).
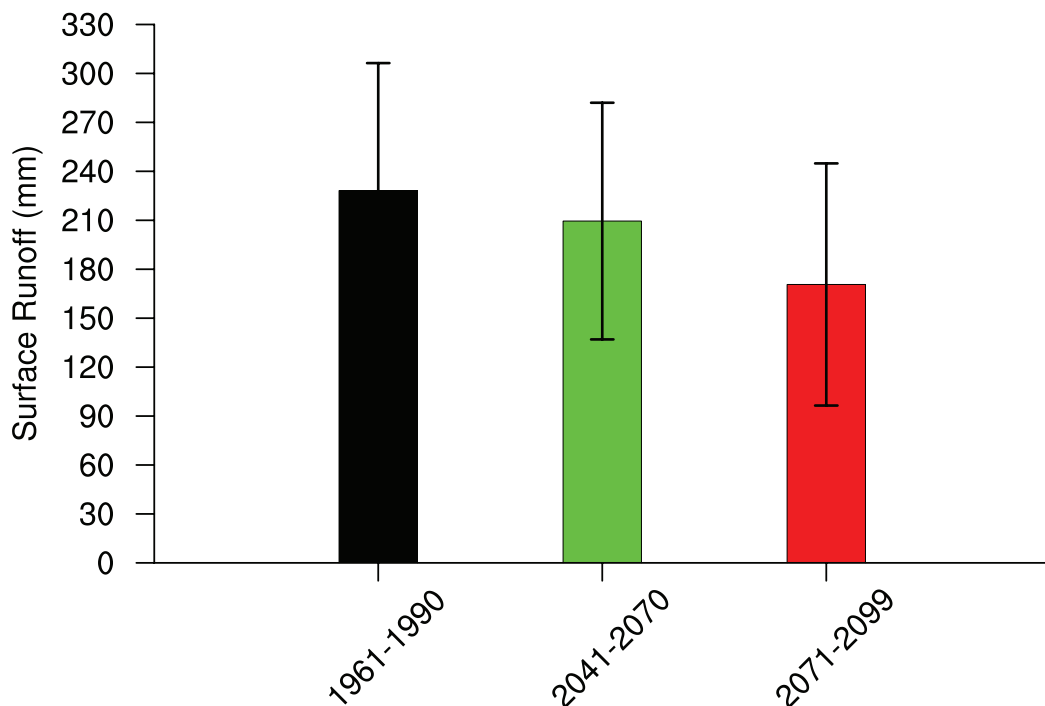
Figure 4.21 : Annual area averaged surface runoff values from the ECHAM5 simulations for the headwaters of the Euphrates and Tigris Rivers in the eastern Anatolia mountains of Turkey. Color bars represent the periods: black for 1961-1990, green and red for 2041-2070 and 2071-2099 respectively. Lines indicate the standard deviations for corresponding periods.

Table 4.3 summarizes the projected changes of annual temperature, precipitation, evaporation and SWE in the highlands and lowlands of the entire basin. Annual temperature increases in all simulations are statistically significant at 99.9% confidence level. Annual precipitation is generally projected to decrease in the highlands and to increase in the lowlands. Some of these changes are found to be statistically significant at different confidence levels, whereas changes in ECHAM5 simulations are found to be mostly insignificant. Projected changes in annual evapotranspiration indicate generally statistically significant decreases in the basin by the end of the century. Such decreases should be primarily related with the projected decreases in precipitation in these regions. A more striking impact of warming could be seen on the SWE in the highlands. All simulations point out substantial decreases in SWE in the highlands for both periods of 2041-2070 and 2071-2099, and these reductions are found to be statistically significant.

Much of the highlands of the ETB lies in Turkey, therefore, the values for the highlands given in Table 4.3 broadly reflect the projected changes in the highlands in the territory of Turkey. The changes in the lowland areas of Turkey within the basin, however, differ largely from those of the lowland areas of the whole basin (see Table 4.3). Major differences appear in precipitation and evaporation. Apparently, the lowland areas within Turkey will be subject to more drying in comparison to the lowlands of the whole basin.

4.2.2.3 Country-based analysis

Water resources availability, which will be affected greatly by the climate change especially in the arid and semi-arid regions, is a sensitive issue for the countries within the ETB. For this reason, a country-based analysis of the changes in the surface water of the basin is included. The country borders within the ETB are determined and then reference and projected annual surface runoff (mm) of four countries (Iran, Iraq, Syria and Turkey) based on the ECHAM5 A2 simulation for 2041-2070 and 2071-2099 periods are demonstrated (Figure 4.22). The relatively high annual surface runoff in the territory of Turkey within the ETB for the reference period (approximately 150 mm) indicates that this part of ETB is the main source of water in the basin, and it is apparent that the annual surface runoff is projected to decrease substantially for both 2041-2070 and 2071-2099 periods.

Table 4.3 : Annual absolute values of reference period (1961-1990) and future periods (2041-2070 and 2071-2099) for temperature, precipitation, evaporation and snow water equivalent in the highlands and lowlands of the whole basin and in the lowlands of Turkey within the basin. Red, green and blue colors are for significant changes at 99.9%, 95%, and 90% confidence levels, respectively.

	WHOLE BASIN						TURKEY		
	HIGHLANDS			LOWLANDS			LOWLANDS		
	HISTORICAL (1961-1990)	2041-2070	2071-2099	HISTORICAL (1961-1990)	2041-2070	2071-2099	HISTORICAL (1961-1990)	2041-2070	2071-2099
Temperature									
ECHAM5 A2	9.5 °C	11.8 (+2.3°C)	14 (+4.5°C)	21.4 °C	24 (+2.6°C)	26.2 (+4.8 °C)	15.7 °C	17.9 (+2.2°C)	20.1 (+4.4 °C)
HadCM3 A2	8.7 °C		13.4 (+4.7°C)	20.2 °C		24.9 (+4.7°C)	14.9 °C		19.6 (+4.7°C)
CCSM3 A2	10.9 °C	13.9 (+3°C)	15.9 (+5 °C)	22.4 °C	25.4 (+3°C)	27.2 (+4.8°C)	17.1 °C	20 (+2.9°C)	22 (+4.9°C)
CCSM3 A1F1	10.9 °C	15 (+4.1°C)	17 (+6.1°C)	22.4 °C	26.2 (+3.8°C)	28.1 (+5.7°C)	17.1 °C	21.1 (+4°C)	23.1 (+6°C)
CCSM3 B1	10.9 °C	13 (+2.1°C)	13.5 (+2.6°C)	22.4 °C	24.4 (+2°C)	24.7 (+2.3°C)	17.1 °C	19.1 (+2°C)	19.5 (+2.4°C)
Precipitation									
ECHAM5 A2	653 mm/yr	663 (+1.5%)	613 (-6.1%)	190 mm/yr	219 (+15.3%)	196 (+3.1%)	430 mm/yr	429 (-0.2%)	382 (-11.2%)
HadCM3 A2	553 mm/yr		477 (-13.7%)	95 mm/yr		97 (+2.1%)	376 mm/yr		313 (-16.7%)
CCSM3 A2	410 mm/yr	370 (-9.8%)	313 (-23.6%)	54 mm/yr	57 (+5.5%)	46 (-14.8%)	218 mm/yr	201 (-7.8%)	162 (-25.7%)
CCSM3 A1F1	410 mm/yr	293 (-28.5%)	273(-33.4%)	54 mm/yr	42 (-22.2%)	49 (-9.2%)	218 mm/yr	145 (-33.5%)	141 (-35.3%)
CCSM3 B1	410 mm/yr	379 (-7.6%)	334 (-18.5%)	54 mm/yr	47 (-13%)	49 (-9.2%)	218 mm/yr	197 (-9.6%)	172 (-21.1%)
Evaporation									
ECHAM5 A2	427 mm/yr	463 (+8.4%)	457 (+7.0%)	158 mm/yr	172 (+8.9%)	155 (-1.9%)	368 mm/yr	367 (-0.3%)	333 (-9.5%)
HadCM3 A2	374 mm/yr		370 (-1.1%)	85 mm/yr		84 (-1%)	329 mm/yr		284 (-13.7%)
CCSM3 A2	274 mm/yr	282 (+2.9%)	258 (-5.8%)	52 mm/yr	56 (+7.7%)	47 (-9.6%)	192 mm/yr	181 (-5.7%)	149 (-22.4%)
CCSM3 A1F1	274 mm/yr	238 (-13%)	230 (-16%)	52 mm/yr	43 (-17.3%)	50 (-3.8%)	192 mm/yr	137 (-28.6%)	134 (-30.2%)
CCSM3 B1	274 mm/yr	279 (+1.8%)	257 (-6.2%)	52 mm/yr	47 (-9.6%)	49 (-5.8)	192 mm/yr	179 (-6.8%)	159 (-17.2)
SWE									
ECHAM5 A2	35 mm	15 (-57.1%)	5 (-85.7%)	0 mm	0	0	0 mm	0	0
HadCM3 A2	34 mm		6.8 (-80%)	0 mm	0	0	0 mm	0	0
CCSM3 A2	31 mm	12 (-61.3%)	7 (-77%)	0 mm	0	0	0 mm	0	0
CCSM3 A1F1	31 mm	8 (-74.2%)	4 (-87%)	0 mm	0	0	0 mm	0	0
CCSM3 B1	31 mm	21 (-32.2%)	14 (-54.8%)	0 mm	0	0	0 mm	0	0
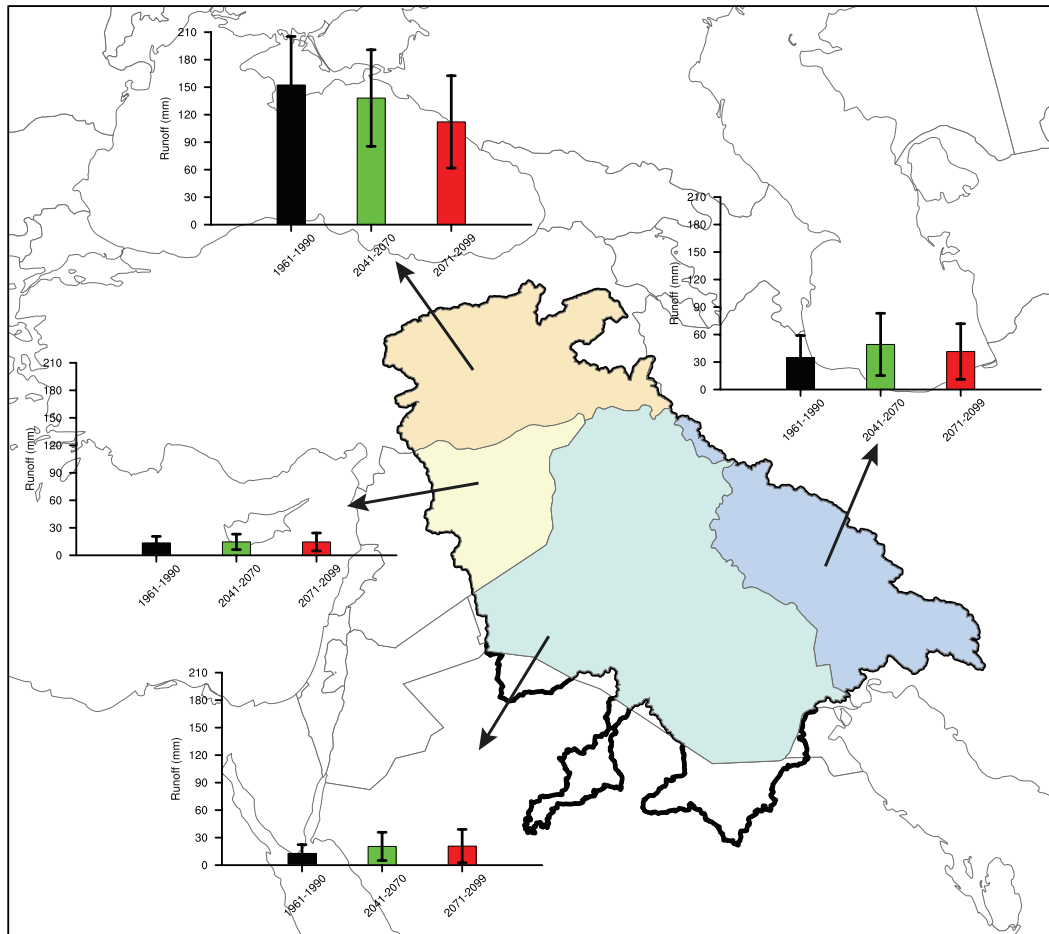
Figure 4.22 : Annual area averaged surface runoff values from the ECHAM5 simulations for the countries (Iran, Iraq, Syria and Turkey) within the Euphrates-Tigris Basin. Color bars represent the periods: black for 1961-1990, green and red for 2041-2070 and 2071-2099 respectively. Lines indicate the standard deviations for corresponding periods.

The annual surface runoff of Syrian territory within the basin (approximately 15 mm) is projected to remain virtually unchanged. For Iranian territory, the annual surface runoff is simulated to increase in the future, however, the increase is more pronounced for the 2041-2070 period. The annual surface runoff is projected to increase for the Iraqi territory for both future periods. The projected increase in precipitation in the southern parts of the ETB is likely the major reason behind the surface runoff increase in this region. Evapotranspiration also increases in this region but the increase is comparatively small. Önol and Semazzi (2009) argue that the enhanced moisture transfer from the regions of Red Sea, Persian Gulf and Mediterranean Sea together with the changes in the low-level circulation is probably responsible for the autumn precipitation increases in the southern parts of the ETB.

70

Using downscaled data from the NCEP/NCAR reanalysis for the present and the CCSM3 A2 scenario simulation for the future, Evans (2008) studied the projected changes in the storms affecting the eastern Fertile Crescent region on the basis of water vapor fluxes. He found a dramatic shift in the water vapor transport courses from westerly to southerly directions largely during the transition seasons, especially autumn, which implies enhanced transportation of water vapor from the Red Sea, Persian Gulf, and Arabian Sea towards the southern parts of the ETB.

Figure 4.23 shows projected changes of annual surface runoff (%) for the four countries (Iran, Iraq, Syria and Turkey) within the ETB from five different simulations for 2071-2099 period relative to the 1961-1990 reference. One of the most striking points is that all the simulations agree on a reduction in the surface runoff for the territory of Turkey in the ETB, which ranges from 25 to 55% for the simulations. Except for the CCSM3 A2 simulation, the A2 simulations point out surface runoff increase (more than 50%) for the Iraqi territory. Together with HadCM3 A2 simulation the CCSM3 simulations indicate substantial decreases in the surface runoff in the Syrian part by the end of the century (between 21 and 39%). In the case of Iranian part of the basin, surface runoff is projected to decrease by 12 to 24% in CCSM3 simulations, whereas it is projected to increase by 11% in ECHAM5 A2 simulation.
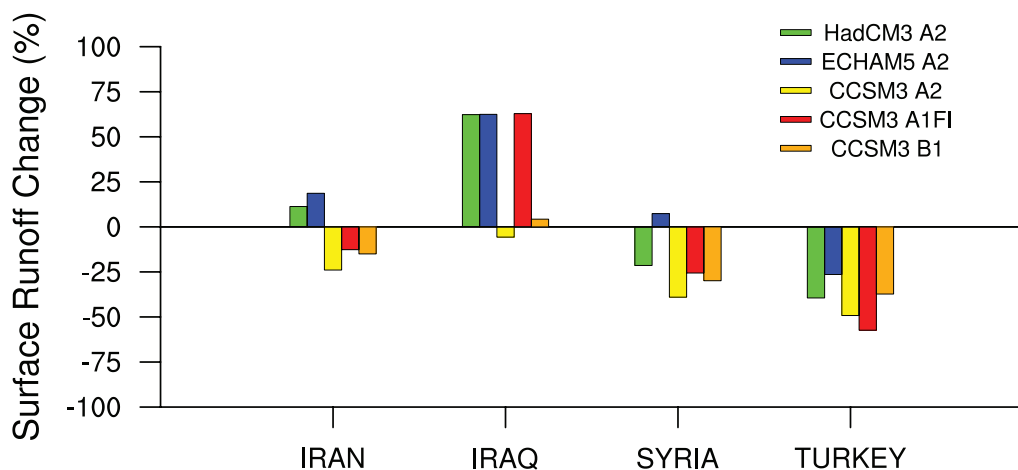
Figure 4.23 : Annual area averaged surface runoff changes (%) for Iran, Iraq, Syria and Turkey by the end of the century (2071-2099) relative to the 1961-1990 reference period. Color bars denote different simulations: green for HadCM3 A2, blue for ECHAM5 A2, yellow for CCSM3 A2, red for CCSM3 A1FI and orange for CCSM3 B1.

5. HYDROLOGICAL DISCHARGE MODEL SIMULATIONS

It has now become more important to use surface outputs of atmospheric models such as snow water equivalence and runoff, which are calculated by using precipitation, temperature, wind speed components, humidity, long wave and short wave radiation, in similar physically-based hydrologic models for hydrometeorological studies (e.g. Xu, 1999; Lin et al., 2006; Bell et al., 2007; Sorooshian et al., 2008). In addition to this, hydrological simulations obtained from atmospheric models by using different climate scenarios are important to demonstrate climate change impacts on the hydrological cycle (Christensen et al., 2004; Sorooshian et al., 2008). Coupled atmosphere-hydrology models are also used for flood and heavy rainfall forecasting (e.g. Bartholmes and Todini, 2005; Tomassetti et al., 2005; Verdecchia et al., 2008).

Hydrological discharge models are mainly used to compute the discharge of a given catchment to a specific point via mathematical expressions (Hagemann and Dümenil, 1998). The ranges of types of hydrological discharge models are based on the spatial representation of the models. For instance, lumped models ignore spatial heterogeneity and act the catchment as a single box. Semi-distributed models consist of smaller sub-catchments based on topography. Fully distributed models take into account spatial heterogeneity and reflect spatial variations of hydrometeorological parameters such as precipitation and temperature as well as spatial occurrence of watershed characteristics such as soils, slope and land cover (Chow et al., 1998). In general, both semi-distributed and fully distributed models have some advantages compared to the lumped models such as better representation of spatial variability within the catchment. On the other hand, because of increased heterogeneity they contain a large number of parameters and in most cases, a model parameterization is needed, which simplifies the representation of sub-grid processes. Moreover, large amounts of input data is are required to drive the semi-distributed and fully distributed hydrological discharge models. Meteorological observations and monitoring data are commonly used to calibrate and to validate the hydrological

discharge models. However, climatological data such as precipitation and temperature derived from climate models are alternatively used to drive the hydrological discharge models in regions where inadequate observational network take place.

In hydrological discharge models, it is extremely important to explain and interpret the effect of topography on the surface (Beven, 1989). Topography affects not only the type of soil, surface cover and rainfall but also the flow path and drainage networks (Yuan and Ren, 2004). By using the topography data to obtain a suitable flow chart for a particular area is the first and the most basic step of hydrological simulations. In many physical and lumped-distributed hydrological models topography data is processed through some software programs such as GIS and flow chart is obtained. Many different approaches have been developed in order to obtain the most accurate flow chart by using the topography data (e.g. Tribe, 1992; Coppola et al., 2007). One of the methods used to develop hydrologic routing algorithm is to define each grid as a reservoir and to calculate the flow from cell-to-cell and finally to reach the basin outlet by collecting the flow. In this method, land is divided into small pieces and each piece is assumed to be homogenous and flow from each piece is transferred to the bottom one (Sausen et al., 1994; Sushama et al., 2004).

5.1 The Hydrological Discharge Model (HDM)

The HDM is a state of the art river routing model developed by Hagemann and Dümenil (1998). The model calculates the river discharge by taking into consideration the lateral waterflow on the land surface grid cells. The main purpose of the model is to employ three water storages for every model grid cell (Figure 5.1):

- Overland flow
- Baseflow
- Riverflow

Overland flow and baseflow use surface runoff and drainage as input from land surface scheme of another model. Both of the input fields are interpolated to HDM grid. Riverflow is fed by inflow from other gridboxes. The sum of the three flow processes gives the total grid box outflow and enters the down-stream box in the next

time step. These different modes of lateral flow are controlled by model parameters, which are defined by topography gradient between gridboxes, the slope within a gridbox, the gridbox length, the lake area and the wetland fraction of a particular gridbox (Hageman and Dümenil, 1998).

The model takes into account the linear reservoir in order to represent the flow processes in hydrology. A linear reservoir denotes the outflow Q as the proportion of actual filling S to retention time k that is defined as the average residence time of water within the reservoir (Singh, 1998) (5.1).

$$Q(t) = \frac{1}{k} \bullet S(t)$$

(5.1)

By relating Q to the inflow I the continuity equation is satisfied (5.2).
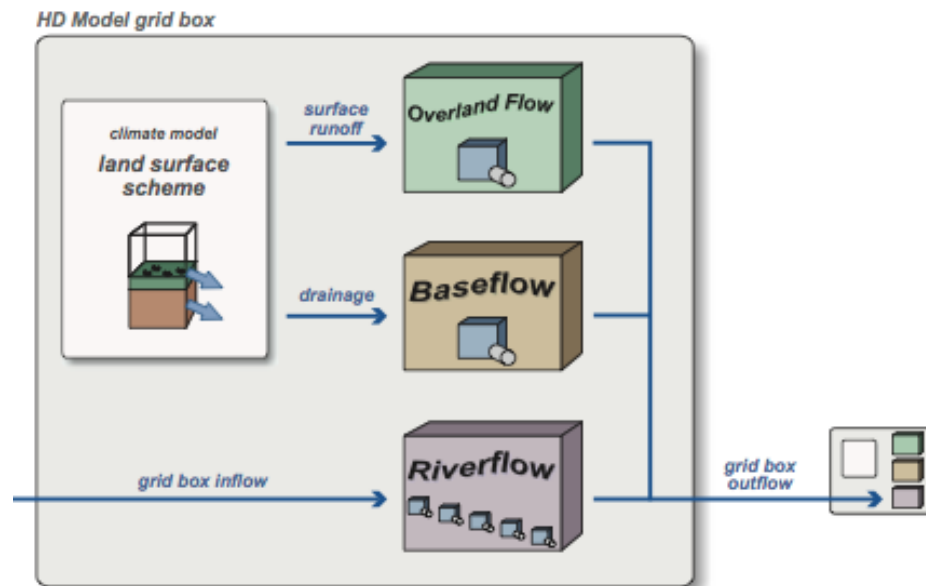
Figure 5.1 : Overview about the general structure of the HDM (Hagemann and Dümenil, 1998).

$$\frac{dS(t)}{dt} = I(t) - Q(t)$$

(5.2)

A linear differential equation for the discharge Q with one parameter k is derived from the Equations (5.1) and (5.2).

$$k\frac{dQ(t)}{dt} = I(t) - Q(t) \tag{5.3}$$

In the HDM, the cascade of *n* equal linear reservoirs (typically 5), which have the same retention coefficient *k,* denotes the riverflow. In this case, the outflow from the reservoir *i* equals the inflow into the reservoir *i+1* and Equation (5.3) is applied to each reservoir. Both the overland flow and the baseflow are represented by a single linear reservoir with retention coefficients.

Besides the different lateral flows, another crucial part of the HDM is a routing scheme that is based on the land surface topography. Drainage network controlled by the surface topography determines the direction of water flow on the surface as well as the catchment boundaries in the model. In the drainage network of the model, it is assumed that every grid cell drains into the neighboring grid cell with the lowest elevation. Derived drainage network by taking into consideration elevation differences should therefore match the actual surface river system. Spatial resolution of the surface topography dataset is the key factor that directly affects the quality of the drainage network. In addition to drainage network, real catchments and their model counterparts should be equal to each other. In the HDM there eight possibilities of outflow directions: the four main directions (N, E, S, W) and the four diagonal directions (NE, SE, SW, NW) (Figure 5.2).
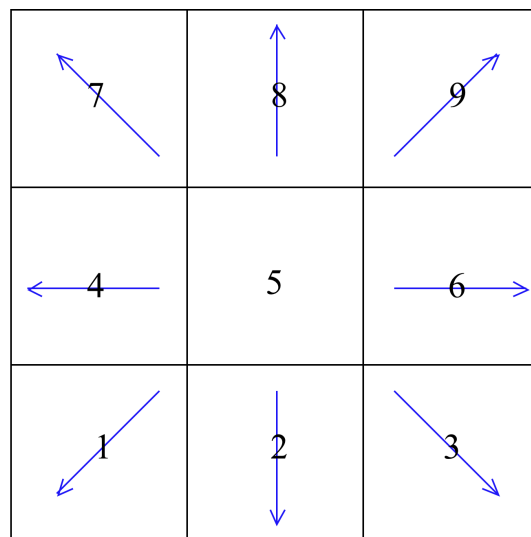
Figure 5.2 : River flow directions in the HDM. Direction 5 corresponds the discharge trap.

Further information about the HDM and its structure can be found in Hageman and Dümenil (1998).

5.2 Modifications, Data and Approach

5.2.1 Modifications

The HDM is applied on a global scale. Daily surface runoff and drainage are the inputs fields required for driving the HDM and they can be derived from the various GCMs with different spatial resolutions. Therefore, their spatial resolutions are interpolated from the respective GCM grid to the HDM grid resolution. Although the HDM has originally been designed for global scale, the input fields derived from the RCMs can be also used for driving the model. RCM fields are interpolated to the 0.5^o x 0.5^o the HDM grid and the model produces discharge on a global scale with "empty" fields over areas outside the RCM domain.

As it is stated in the model description part, the actual river direction flow and its model counterpart must match each other. Therefore, a major task before the analyzing of climate change impacts on Euphrates-Tigris Rivers is to check whether the model represent the actual river network flow and catchment boundary well or not. If needed, an adjustment of the model topography by defining a new river flow directions is carried out via model calibration. For this aim, the HDM was applied to the ETB in the off-line mode using the daily surface runoff and drainage data of GCM-ECHAM5, which has a spatial resolution of 1.875^o x 1.875^o. By using the 30-year reference period (1961-1990) simulations, the HDM was validated against to available streamflow gauges in the basin. Moreover, simulated river flow network was matched with the actual river flow. By taking into consideration the inconsistencies related with river directions, required modifications were done in the model parameter file that contains river direction and riverflow, overflow and baseflow variables. Therefore, in the first stage, two simulations were carried out by using GCM-ECHAM5 driving fields on a global scale for the period of 1961-1990:

- Experiment-1: Simulations done with default parameter file
- Experiment-2: Simulations done with prescribed parameter file

Figure 5.3 represents the real ETB catchment boundary together with river flow network. Murat and Karasu Rivers in the upper parts of the Euphrates Basin, which flow from east to west and merge around Keban, mainly feed the Euphrates River. Then, the Euphrates River flows in the southward and southeastward directions. The Tigris River originates in the eastern Taurus Mountains of southeastern Turkey near Lake Van. It flows across the Mesopotamian lowlands by following the base of the Zagros Mountains. The Euphrates and the Tigris Rivers merge with each other around Al-Basrah before flowing on to the Persian Gulf.
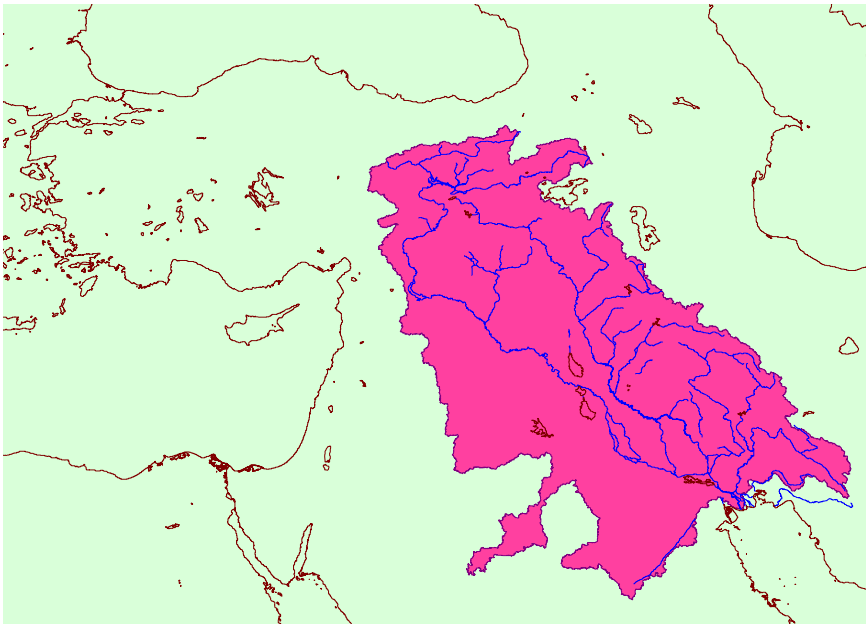
Figure 5.3 : River flow network of the ETB (Zakharova et al., 2007)

Figure 5.4 shows the river direction and corresponding river flow network of the ETB, represented by the HDM from the Experiment1. Comparing with the real river flow network in Figure 5.3, three main inconsistencies can be outlined:

- Murat River has a southwestward direction in the upper parts of the Euphrates Basin and it flows to the Tigris River
- The Tigris River flows to the Euphrates River in Syrian territory
- The Tigris River flows to the Euphrates River around Hindiya

By taking into the three inconsistencies, the river paths of the Euphrates and the Tigris Rivers were prescribed in the parameter file of the HDM. After prescribing

and changing the parameters, the resulting model river flow network from the Experimen-2 has an acceptable degree of reliability and validity (Figure 5.5).
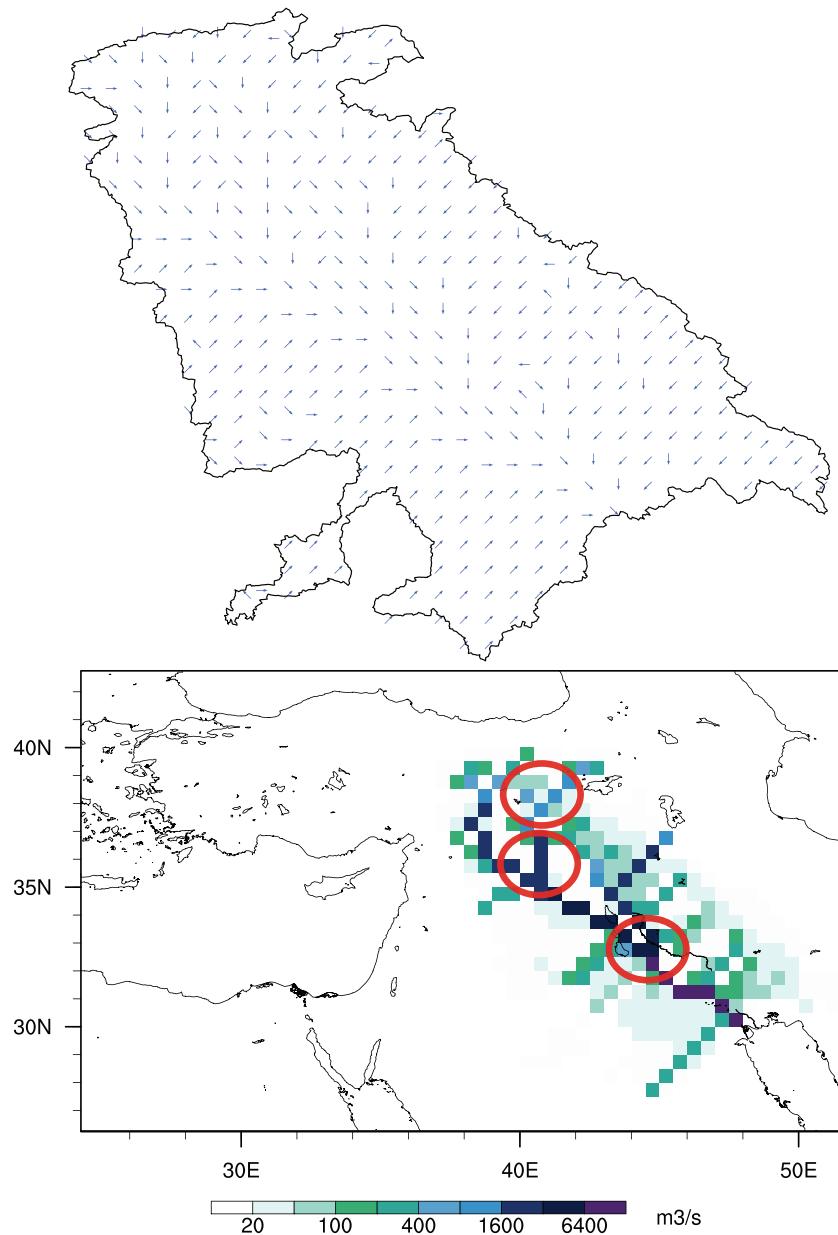
Figure 5.4 : River direction and corresponding river flow network of the ETB represented by the HDM in Experiment-1. Three main inconsistencies are shown with red circles.

The most striking improvement of the river flow network takes place in the upper parts of the Euphrates Basin and it represents well the east to west flows of the Murat and Karasu Rivers. Moreover, the HDM consistently reproduces merging point of the two rivers with the prescribed parameter file. Finally, the Euphrates and the Tigris Rivers merge with each other around Al-Basrah before flowing on to the

Persian Gulf (Figure 5.3) and this property is captured well by the HDM in the Experiment-2.
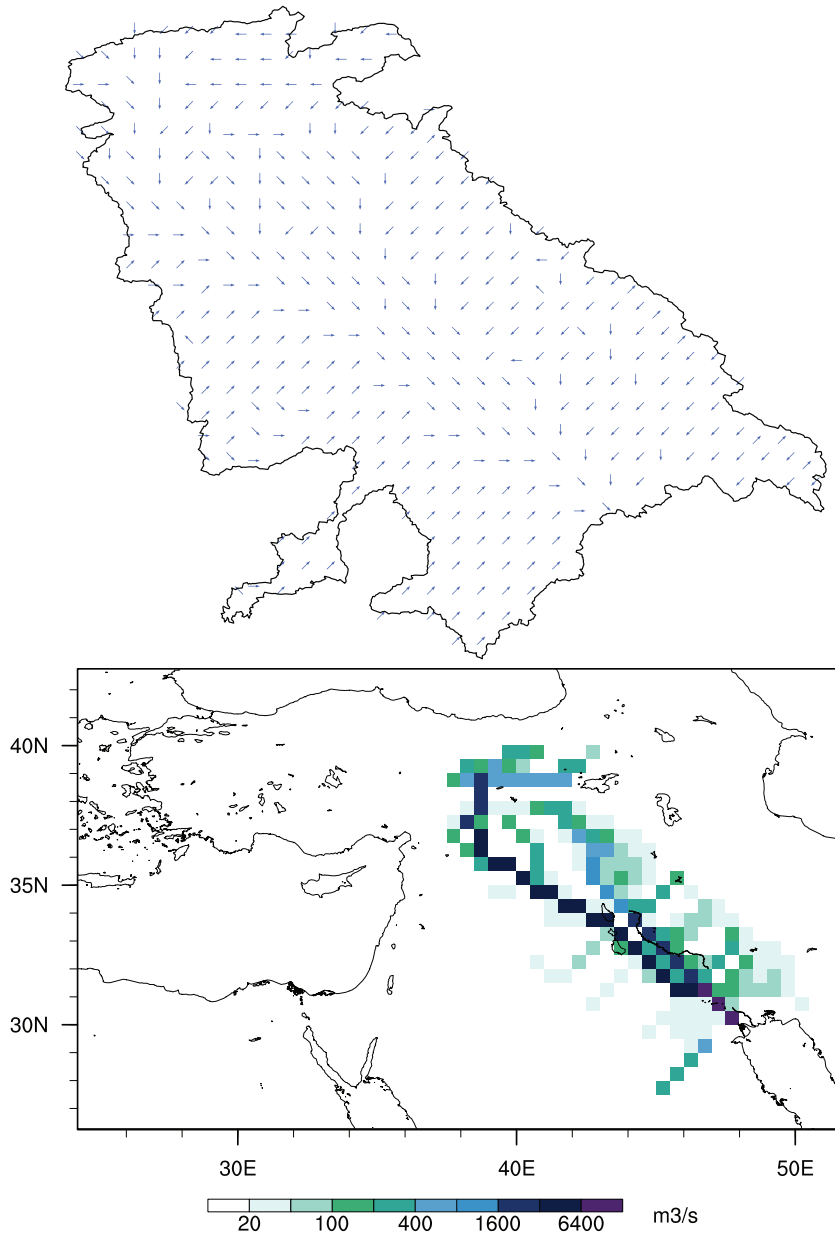
Figure 5.5 : River direction and corresponding river flow network of the ETB represented by the HDM after prescribing and changing the parameters in Experiment-2.

5.2.2 Data and approach

Different input fields from the two GCMs (ECHAM5, MPI-ESM-LR) and from the dynamically downscaled outputs of ECHAM5 and CCSM3, obtained from the UNDP project (MDG-F 1680) entitled with "Enhancing the capacity of Turkey to Adapt to Climate Change", were used to drive the HDM. Detailed information about

the dynamically downscaled outputs and evaluation of the reference period can be found in Bozkurt et al. (2012).

MPI-ESM-LR (Max Planck Institute for Meteorology-Earth System Model-Low Resolution) is a coupled earth system model (Hagemann et al., 2012). It employs the coupling of the atmosphere, ocean and land surface through energy, momentum, water and important trace gases exchanges. It includes ECHAM6 in the atmosphere in T63 resolution (Stevens et al., 2012), MPI-OM in the ocean at approximately 1.6^{o} resolution with 40 vertical layers (Jungclaus et al., 2012) and JSBACH for land surfaces (Brovkin et al., 2009; Brovkin et al., 2012).

A new radiative scheme in the atmosphere, a new aerosol climatology and the incorporation of the carbon cycle including ocean biogeochemistry and and interactive and dynamic vegetation scheme at the land surface are the main differences between the MPI-ESM and its predecessor ECHAM5/MPIOM. In terms of horizontal resolution there is no difference, however, MPI-ESM has 47 vertical atmospheric levels (LR) which has higher atmospheric layers than the ECHAM5/MPIOM with 31 levels.

The period after IPCC-AR4 was released, it was clear that the new scenarios were needed for use by the research community. As a result of several substantial studies and efforts, climate research community pointed out an updated process of scenarios that aims at documenting the emissions, concentrations, and land-cover change projections of the so-called "Representative Concentration Pathways" (RCPs) (Moss et al., 2010). The RCPs are named according to their four different 2100 radiative forcing level (W m^{-2}) as calculated and reported by the individual groups (RCP 2.6 from PBL/IMAGE, RCP 4.5 from PNNL/MiniCAM, RCP 6.0 from NIES/AIM, and RCP 8.5 from IIASA/MESSAGE) (Figure 5.7). The radiative forcing estimates are based on the forcing of greenhouse gases and other forcing agents, however, direct impacts of albedo or the forcing of mineral dust is not included (Moss et al., 2010). The main purpose of the RCPs is to provide time series of radiative forcing, concentration and emissions of greenhouse gases and land-use change for the climate research community to condcut new climate model experiments and produce new climate scenarios (van Vuuren et al., 2011).

The RCP 4.5 scenario of MPI-ESM-LR used to drive the HDM, corresponds a stabilization scenario in which total radiative forcing is stabilized before 2100 via mitigation methods such as employment of a range technologies and strategies for reducing greenhouse gas emissions (Clarke et al., 2007). Detailed information about the RCPs can be found in Moss et al. (2010).
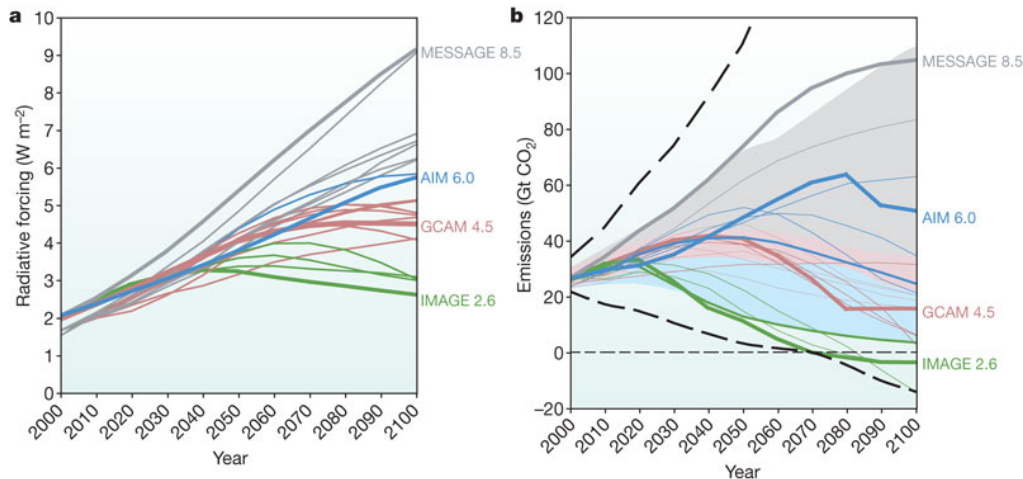
Figure 5.6 : Radiative forcing changes (W m^{-2}) relative to pre-industrial conditions (a). Bold coloured lines show the four RCPs with the corresponding groups; thin lines show individual scenarios. Energy and industry CO_2 emissions for the RCP candidates are presented in right column (b). The range of emissions in the post-SRES literature is presented for the maximum and minimum (thick dashed curve) and 10th to 90th percentile (shaded area). Blue shaded area corresponds to mitigation scenarios; grey shaded area corresponds to reference scenarios; pink area represents the overlap between reference and mitigation scenarios (Moss et al., 2010).

Daily surface runoff and drainage outputs of the RCM simulations that have a spatial resolution of 27 km are used as input fields for the HDM (see Table 5.2). In these cases, the RCM outputs are interpolated to the standard the HDM grid (0.5^{o} x 0.5^{o}) and the discharge simulation is carried out on a global scale, with "empty" input fields over areas outside the RCM domain. The simulations were carried out for both reference period and future period. For all cases, 30-year control climate simulations of present climate were validated against to the observations. Finally, in terms of climate change impacts on the river discharges in the ETB, differences between the future and reference periods are presented. In order to validate the simulation results against to observations, three streamflow gauging stations were used (Figure 5.6). Information about the stations is given in Table 5.1.

Figure 5.7 : Streamflow gauging stations used to validate the HDM.

Since the availability of discharge measurement differs among the stations, the validation period is based on different periods of time for the individual gauging stations. Then, in terms of climate change impacts on the river discharges in the ETB, differences between the future and reference periods are presented. All the input fields used in the HDM simulations are given in Table 5.2.

Table 5.1 : Information about the streamflow gauging stations.

Station Name	Coordinates	Altitude (m)	Drainage Area (km^2)
Palu	38.69N, 39.93E	852	25515
Bağıştaş	39.43N, 38.45E	865	15562
Hindiya	32.72N, 44.27E	28	274100

Table 5.2 : Input files used for driving the HDM.

	Input Fields	Emission Scenario	Period
GCM	MPI-ECHAM5	Observation	1961-1990
		A1B	2071-2100
	MPI-ESM-LR	Observation	1971-2000
		RCP 4.5	2071-2100
RCM	NCEP/NCAR	Observation	1961-1990
	MPI-ECHAM5	Observation	1961-1990
		A2	2040-2100
		B1	2040-2100
	NCAR-CCSM3	Observation	1961-1990
		A2	2040-2100
		A1F1	2040-2100
		B1	2040-2100

5.3 Simulation Results

This section includes the simulation results of the HDM that is forced by GCM and RCM outputs for both reference and future periods. In terms of reference period simulations, 30-year daily surface runoff and baseflow from GCMs, ECHAM5 (1961-1990) and MPI-ESM-LR (1971-2000) and from dynamically downscaled outputs of ECHAM5 (1961-1990) and CCSM3 (1961-1990) were used to drive the HDM. In terms of future period simulations, simulations forced with GCM outputs were carried out for 2071-2100 period, while RCM-forced simulations covered 2040-2609 and 2070-2099 periods. All the simulations were carried out by using the prescribed parameter file.

5.3.1 Reference period simulation results

5.3.1.1 GCM-forced simulations

Figure 5.8 shows the mean annual cycle of the Palu and Bağıştaş streamflow gauging stations together with the HDM simulations forced by ECHAM5 and MPI-ESM-LR. The Palu station has a peak discharge in April, while the Bağıştaş station has in May and this is an indicator of typical snow-fed river characteristics. In general, snow melt-dominated characteristics of the rivers are reproduced by the HDM in both ECHAM5 and MPI-ESM-LR cases. However, ECHAM5-forced simulations have less flow in the peak season and timing of the annual peak discharge corresponds to March for the both Palu and Bağıştaş streamflow gauging stations, which are earlier compared to the observations. Simulations of MPI-ESM-LR input fields yield better match with the observations, especially for the peak season (Figure 5.8b, d). Moreover, timing of the annual peak discharge for the Bağıştaş station is reproduced by the HDM.

It's crucially important to validate the model results over relatively bigger sub-catchments of the ETB. Hindiya streamflow gauging station, which has a drainage area of 274100 km^2, is a good sample for this aim. The validation of the HDM discharge simulations against to the Hindiya gauging station is presented in Figure 5.9. As it is in upper parts of the basin, ECHAM5-forced simulation indicates earlier timing of the annual peak discharge and less flow in the peak season (Figure 5.9a). Although MPI-ESM-LR-forced simulation also reproduces less magnitude of the

observed discharge during the peak season, it reasonably reproduces the annual cycle and the timing of the annual peak discharge (Figure 5.9b).
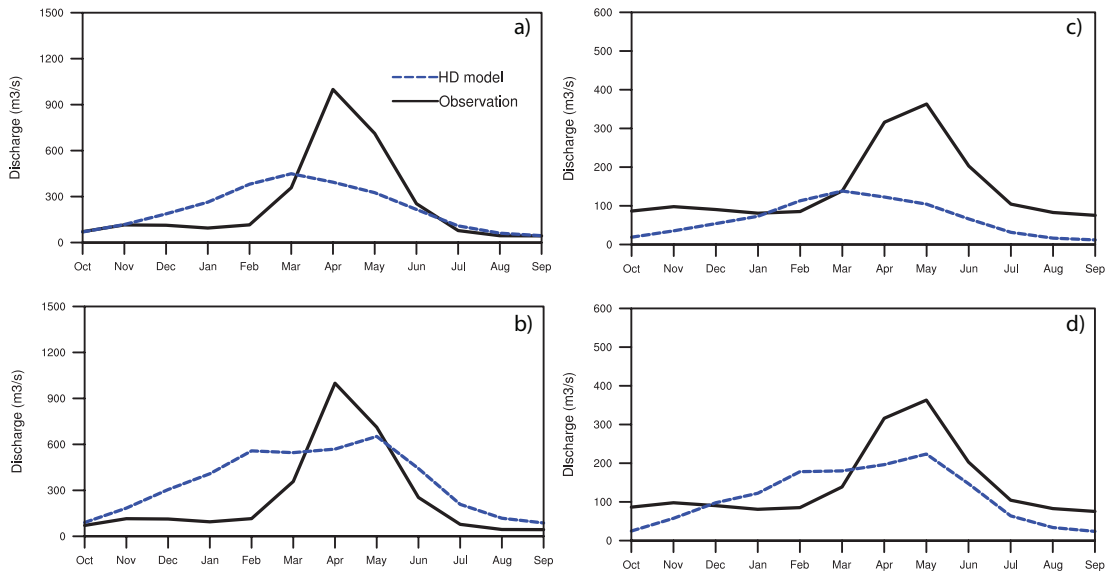
Figure 5.8 : Mean monthly discharge (m^3/s) for the Palu (left column) and Bağıştaş (right column) streamflow gauging stations (solid line) and the HD Model simulations (dashed line). Top panel corresponds to the simulations forced by ECHAM5 input fields. Bottom panel corresponds to the simulations forced by MPI-ESM-LR input fields.
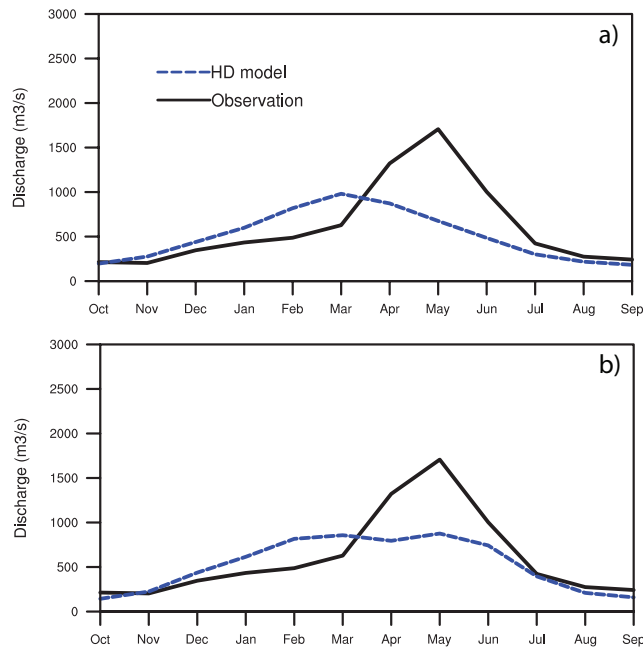
Figure 5.9 : Mean monthly discharge (m^3/s) for the Hindiya streamflow gauging station (solid line) and the HDM simulations (dashed line). Top panel corresponds to the simulations forced by ECHAM5 input fields. Bottom panel corresponds to the simulations forced by MPI-ESM-LR input fields.

The general bias in the timing of the annual peak and peak season discharge in the ECHAM5-forced simulations can be caused by shortcomings of the ECHAM5 input fields. Since the surface orography is the main source of the precipitation over the highlands of the ETB, coarse resolution of the ECHAM5 may not adequate to represent the spatial distribution of precipitation especially over the upper parts of the basin. Indeed, comparison of 30-year average annual precipitation distribution from the ECHAM5 and CRU observation indicates drier conditions in the ECHAM5 (Figure 5.10).
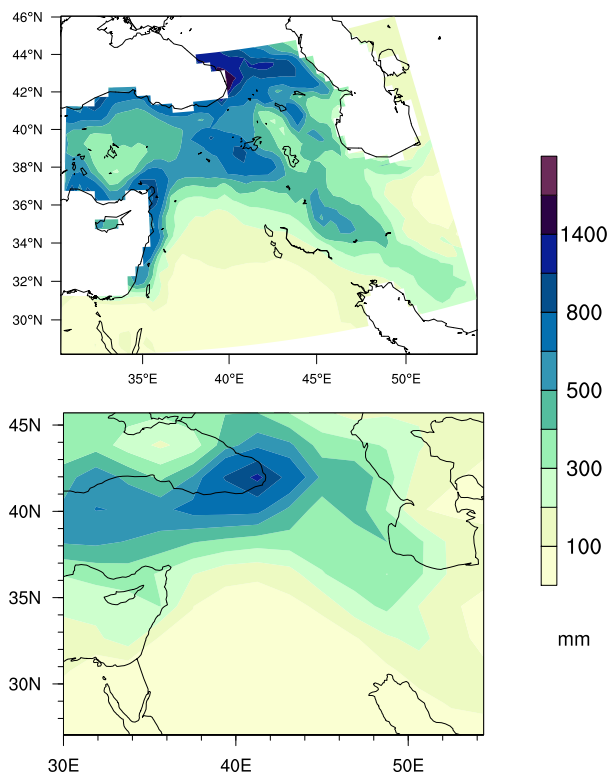
Figure 5.10 : 30-year average annual precipitation (mm) distribution for CRU (top panel) and ECHAM5 (bottom panel).

Moreover, annual cycle of precipitation of the ECHAM5 compared to the Palu meteorological station, yield a poor match in the spring season, which may be accounted for the low peak season discharge in the HDM simulations forced by ECHAM5 input fields (Figure 5.11).

5.3.1.2 RCM-forced simulations

Figure 5.12 shows the mean annual cycle of the Palu, Bağıştaş and Hindiya streamflow gauging stations together with the HDM simulations forced by GCMs (ECHAM5, MPI-ESM-LR) and RCM outputs (NCEP/NCAR, ECHAM5, CCSM3).
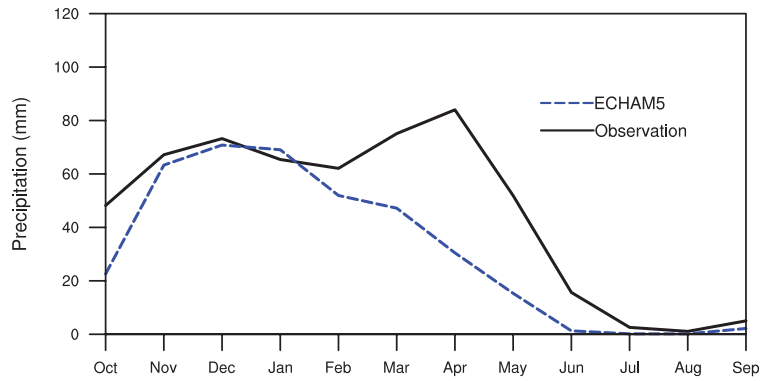
Figure 5.11 : Mean monthly precipitation (mm) for the Palu meteorological station and corresponding grid from ECHAM5.
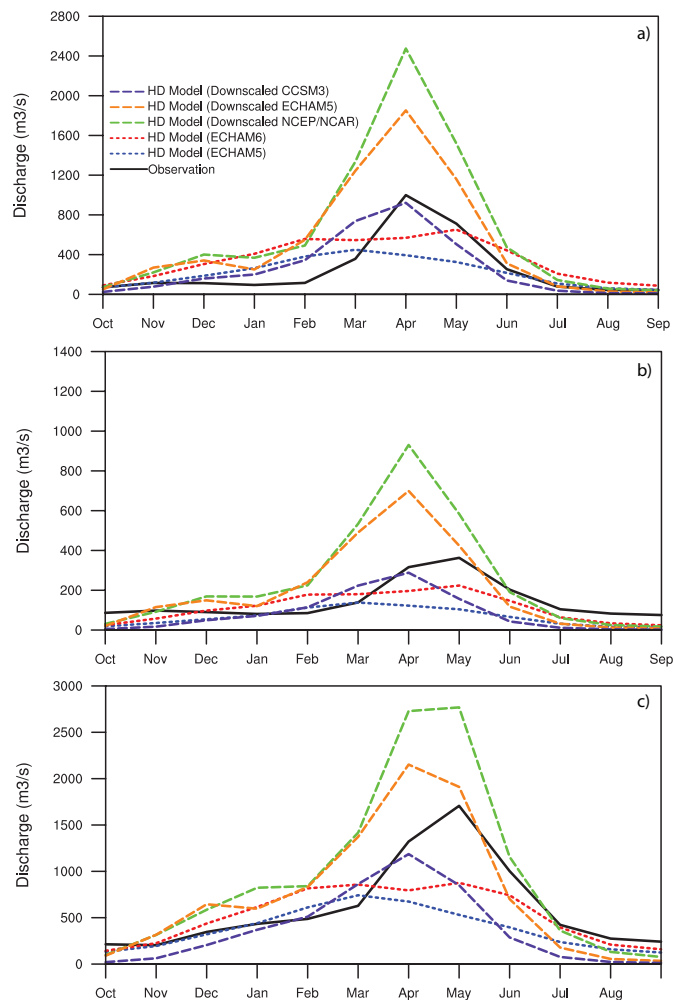
Figure 5.12 : Mean monthly discharge (m³/s) for the Palu (a), Bağıştaş (b) and Hindiya (c) streamflow gauging stations and the HDM simulation results forced by GCMs (ECHAM5, MPI-ESM-LR) and RCM outputs (NCEP/NCAR, ECHAM5, CCSM3).

In contrast to GCM-forced simulations, RCM-forced simulations reasonably reproduce the annual cycle of discharge. Overestimation of the peak of discharge and

bias in the timing of the springtime snowmelt peak of discharge compared to observations persist. In general, overestimation of discharge during the cold season can be caused by shortcomings of the regional climate model, especially related to the annual cycle of precipitation. Indeed, observed annual cycle of precipitation compared with RCM simulations in the upper Euphrates Basin indicate an overestimation of precipitation in the cold season, which is more pronounced in NCEP/NCAR and ECHAM5 simulations (Figure 5.13a).
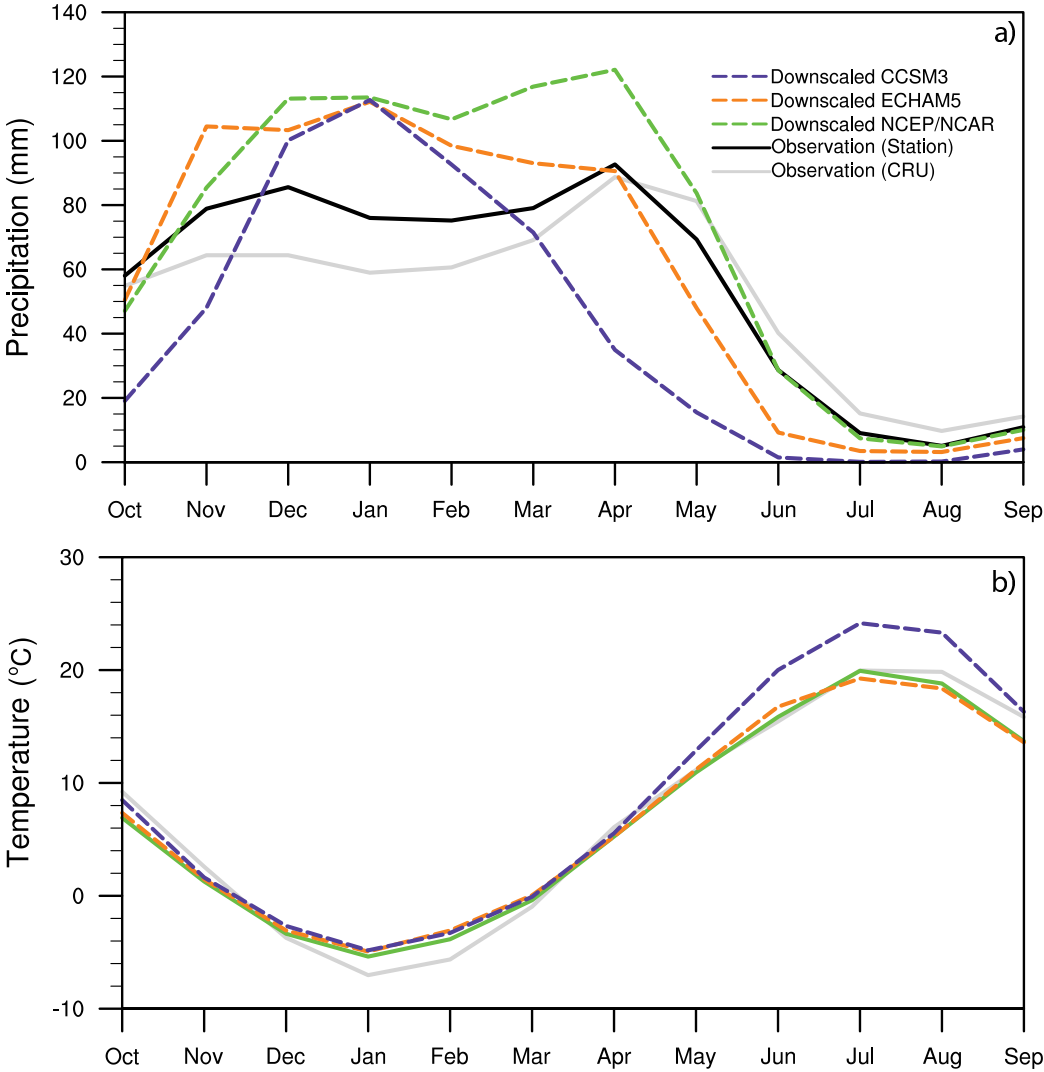
Figure 5.13 : Observed and simulated mean monthly precipitation (mm) and temperature (^{o}C) for the upper Euphrates Basin.

One of the most striking points in Figure 5.12 is that highest differences in discharge take place in March and April months, in which snow melting dominates. In addition to precipitation overestimation in these months, observed annual cycle of temperature compared with RCM simulations point out an overestimation of

temperature during the winter months and early spring (Figure 5.13b). Therefore, warmer temperature values in transition month (March) may be accounted for high discharge values in RCM-forced simulations.

5.3.2 Projected discharge simulations

5.3.2.1 GCM-forced simulations

Figure 5.14 shows the 30-year mean annual discharges of the HDM simulations forced with the ECHAM5 and MPI-ESM-LR input fields (Figure 5.14a, c) for the reference periods, which are 1961-1990 for the ECHAM5 and 1971-2000 for the MPI-ESM-LR driven simulations. The figure also depicts 30-year mean annual discharge differences from the reference period by the end of the century (2071-2100). The ECHAM5 driven simulation of future period is based on SRES A1B emission scenario. The MPI-ESM-LR driven simulation of future period was carried out under RCP 4.5 scenario.

In general, both GCM-forced simulations indicate striking decreases in discharges of the Euphrates and Tigris Rivers. The MPI-ESM-LR forced simulations yield more decrease in the discharges (Figure 5.14d). Mean annual discharge is projected to decrease by 15-20 % in the upper parts of the basin and the main routing paths of the Euphrates and Tigris Rivers for the ECHAM5 forced simulations, while it is projected to decrease by 20-25 % for the MPI-ESM-LR forced simulations. On the other hand, the ECHAM5 forced simulations indicate slightly decrease in discharge over the southeastern parts of the basin by the end of the century under the A1B emission scenario (Figure 5.14b).

Differences in the input fields of the ECHAM5 and MPI-ESM-LR may be accounted for the different behavior of the projected discharges. Indeed, future and reference period differences in total runoff outputs of the raw ECHAM5 and MPI-ESM-LR point out striking differences in the southeastern parts of the basin. Raw ECHAM5 differences indicate an increase in the total runoff over this region Figure 5.15a, while it is projected to decrease in the raw MPI-ESM-LR (Figure 5.15b). Figure 5.16 indicates the mean monthly discharges of the reference and future periods in the corresponding model grids of the Palu ve Bağıştaş streamflow gauging stations from the ECHAM5 and MPI-ESM-LR forced the HDM simulations.
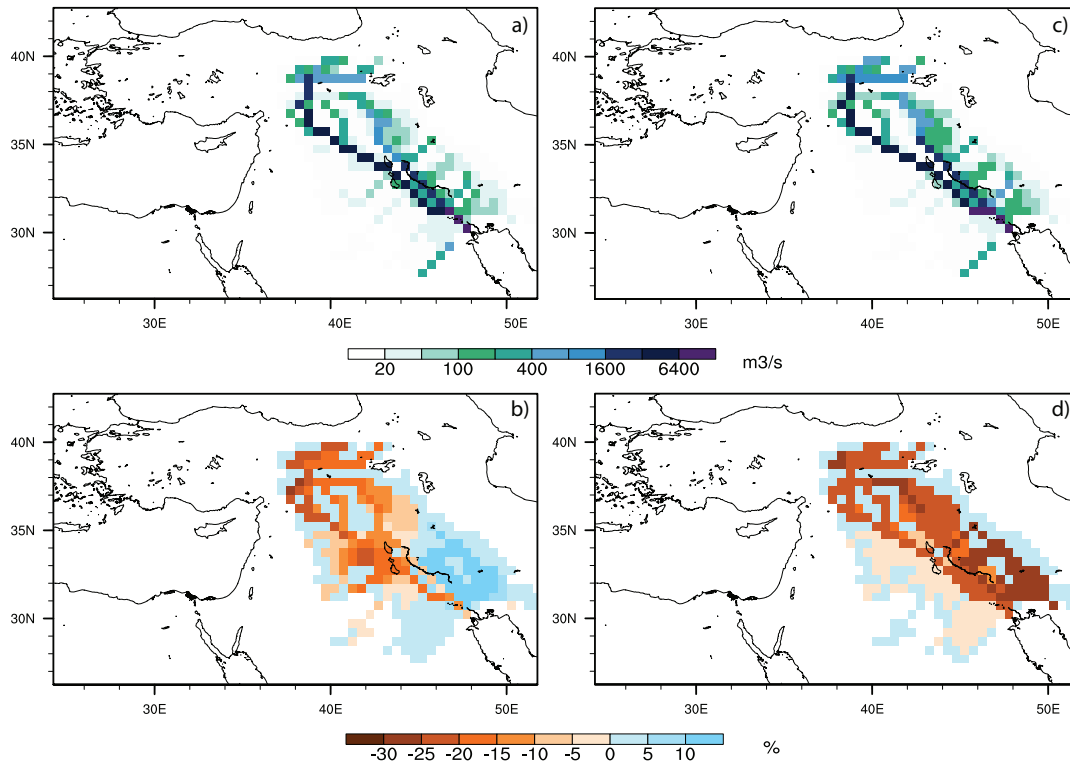
Figure 5.14 : 30-year reference period (1961-1990 for the ECHAM5-forced simulations (a) and 1971-2000 for the MPI-ESM-LR driven simulations (c)) mean annual discharges (m3/s, top panel) and 30-year mean annual discharge differences from the reference period (%, bottom panel). Future projections (2071-2100) of the ECHAM5 (b) input fields are based on SRES A1B emission scenario and the MPI-ESM-LR are based on RCP 4.5 scenario.

In the ECHAM5 forced simulations, the discharge is projected to increase slightly between November and January months for the both Palu and Bağıştaş model grids, however, it tends to decrease in rest of the year under the SRES A1B emission scenario (Fig. 5.16a, c). Overall, the total discharge is projected to decrease for these stations by the end of the century. As the increase in temperature is more pronounced by the end of the century, which means earlier melting of snow, the slightly increase of the discharge between November and January is mainly related with the temporal shifts in snowmelt runoff. In the MPI-ESM-LR forced simulations, discharge is projected to decrease whole year, which is more pronounced after winter season based on RCP 4.5 scenario (Figure 5.16b, d). Moreover, the timing of the annual peak discharge tends to shift to earlier month (from May to April). As it is in the ECHAM5 forced simulations, the total discharge is projected to decrease for these stations by the end of the century.

90
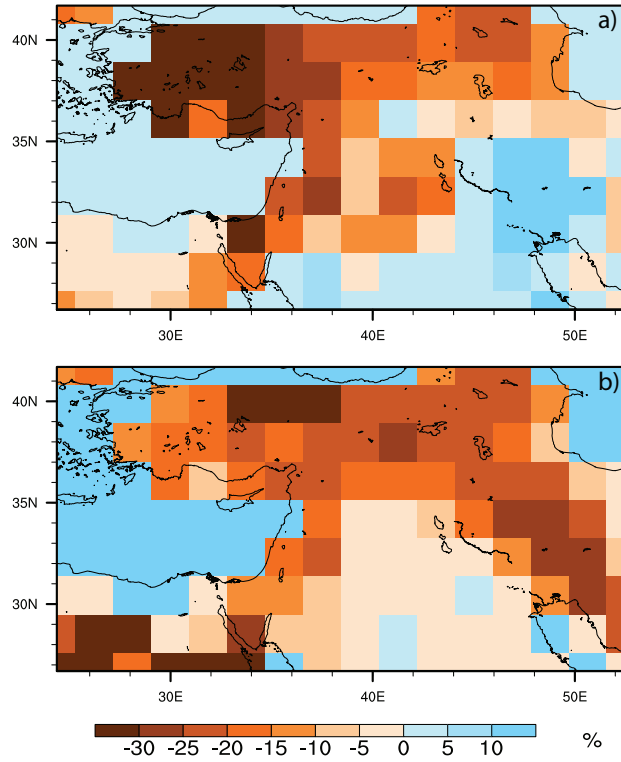
Figure 5.15 : 30-year mean annual total runoff differences (%) from the reference period by the end of the century, (a) for the ECHAM5 and (b) for the MPI-ESM-LR.
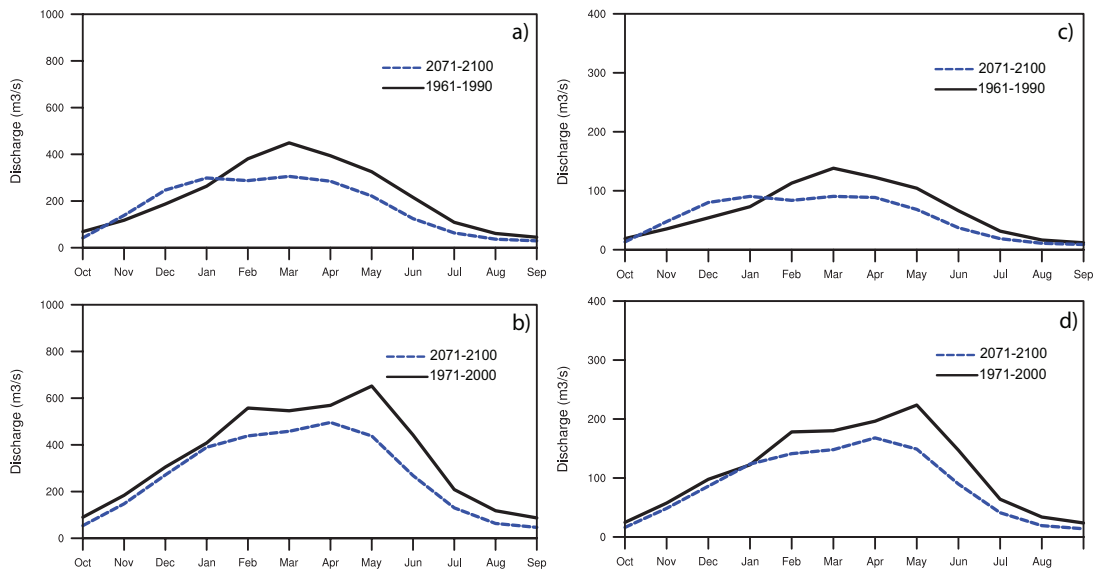
Figure 5.16 : The HDM simulations of mean monthly discharge (m3/s) of the Palu (a, b) and Bağıştaş (c, d) for the reference and future periods. Top panel corresponds to the simulations forced by ECHAM5 input fields and bottom panel corresponds to the simulations forced by MPI-ESM-LR input fields.

As it is in upper parts of the basin, projected discharge simulations of the ECHAM5-SRES A1B and MPI-ESM-LR-RCP 4.5 demonstrate reductions in discharge for the Hindiya too, which is more pronounced for the ECHAM5 forced simulations (Figure 5.17a). Similarly, earlier timing of the annual peak discharge is projected by the simulations.
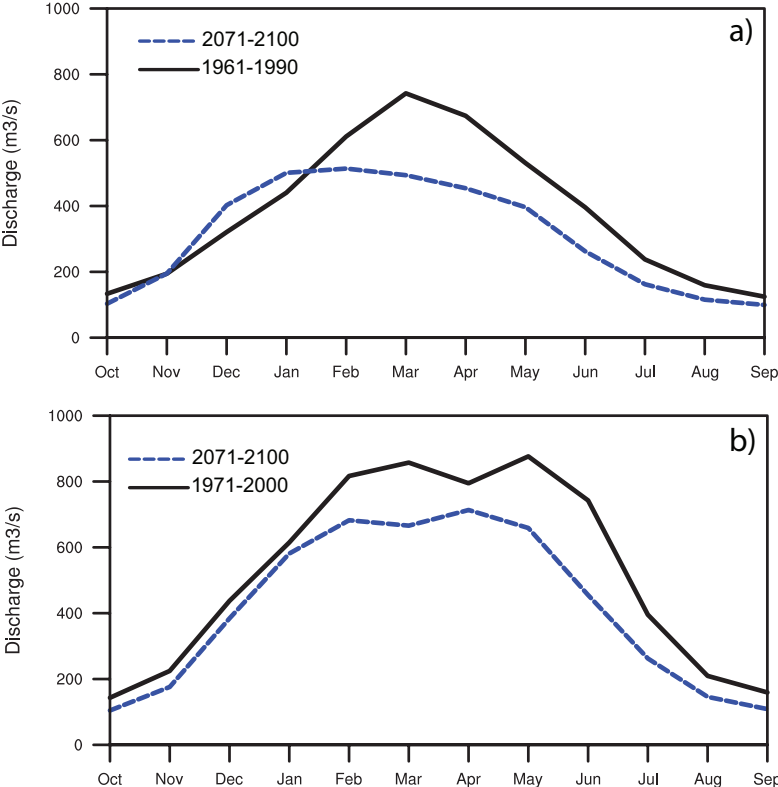
Figure 5.17 : The HDM simulations of mean monthly discharge (m3/s) of the Hindiya for the reference and future periods. Top panel corresponds to the simulations forced by ECHAM5 input fields and bottom panel corresponds to the simulations forced by MPI-ESM-LR input fields.

In addition to projected mean monthly discharges, it is important to look into the changes in the peak discharge timing in the water year. Figure 5.18 shows the reference and projected fractions of accumulated discharge for the Palu, Bağıştaş and Hindiya streamflow gauging stations. Vertical arrows correspond to the days when 50% of annual discharge is reached, which analogous to CT. The detailed information about the method can be found in Chapter 3.

CT date of the reference period is marked as the second half of March for the ECHAM5 forced simulations and it is marked as the beginning of April for the MPI-ESM-LR forced simulations. Projected daily discharges indicate more shifting in CT dates of each station for the ECHAM5-forced simulations.
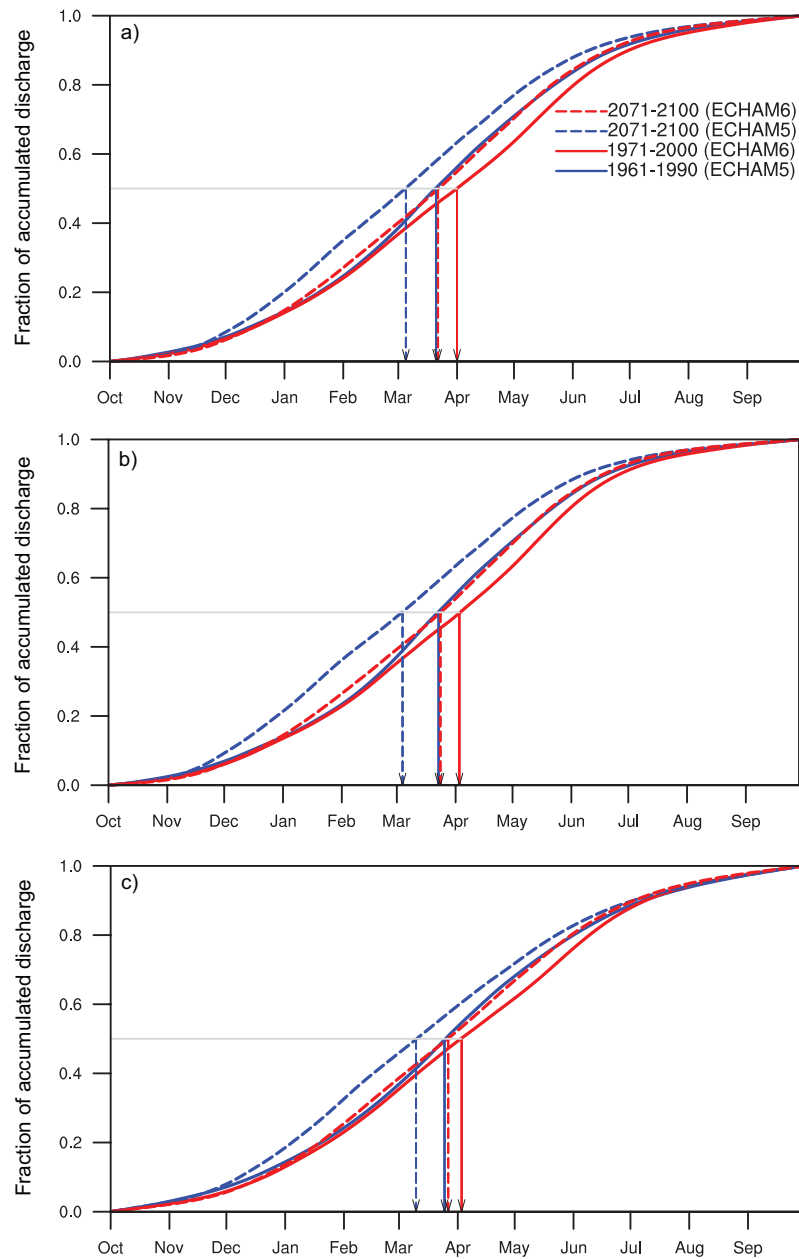
Figure 5.18 : Fraction of accumulated discharge of reference periods (solid line) and future periods (dashed line) from the ECHAM5 forced (blue) and MPI-ESM-LR forced simulations (red) for the Palu (a), Bağıştaş (b) and Hindiya (c). Vertical arrows correspond the days when 50% of annual discharge is reached.

5.3.2.2 RCM-forced simulations

Figure 5.19 shows the HDM results of mean monthly discharge and CT date changes forced with the dynamically downscaled ECHAM5 A2 scenario. Future period is divided into two parts: 2040-2069 and 2070-2099. In the mid-century, it is projected that there is a slightly decrease in discharge for the three stations. However, there is no striking change in the CT of the discharges. By the end of the century, however,

all stations will have less discharge and striking shifts to earlier days are projected for the discharge.
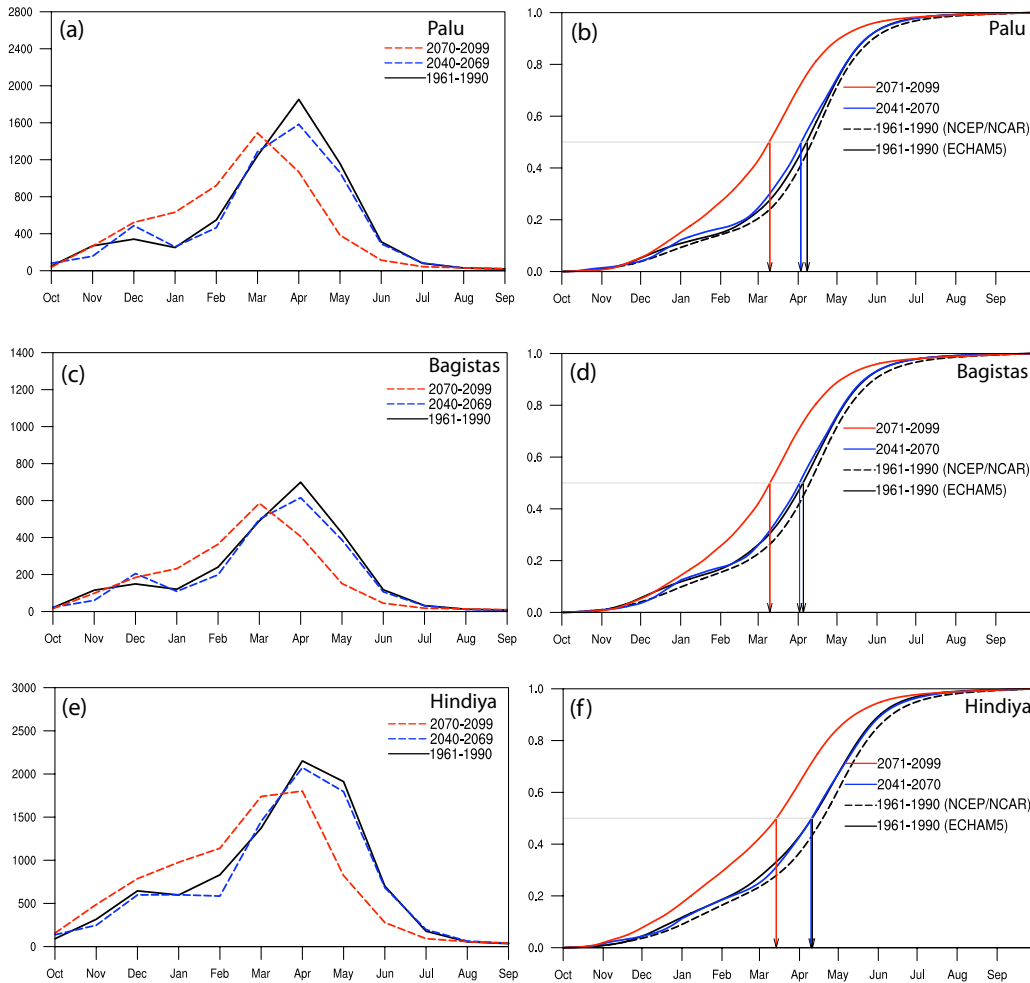
Figure 5.19 : The HDM simulation results of reference (solid line) and future periods (dashed line; blue for mid-century, red for end of the century) forced with dynamically downscaled the ECHAM5 A2 scenario output. Left column corresponds to changes in the mean monthly discharges (m^3/s). Right column corresponds to changes in the fraction of accumulated discharges. Vertical arrows correspond the days when 50% of annual discharge is reached.

Figure 5.20, 21, 22 demonstrate the HDM results forced with the dynamically downscaled outputs of CCSM3 A1FI, A2 and B1 scenarios. It is clearly depicted that discharge is projected to decrease dramatically from the mid-century in higher (A1FI) and mid-high (A2) emission scenario simulations. Moreover, striking shifts to earlier days are projected for the discharge in the both A1FI and A2 emission scenario simulastions. On the other hand, relatively small reductions in discharge and shifts are projected in B1 emission scenarios, which has lower emissions. Table 5.3 presents the date of CT for both reference and future periods in RCM-forced

simulations. CT of the discharges occurs in early April in reference period, while it is projected to shift to 3-5 weeks to earlier (early and mid March) in future periods.
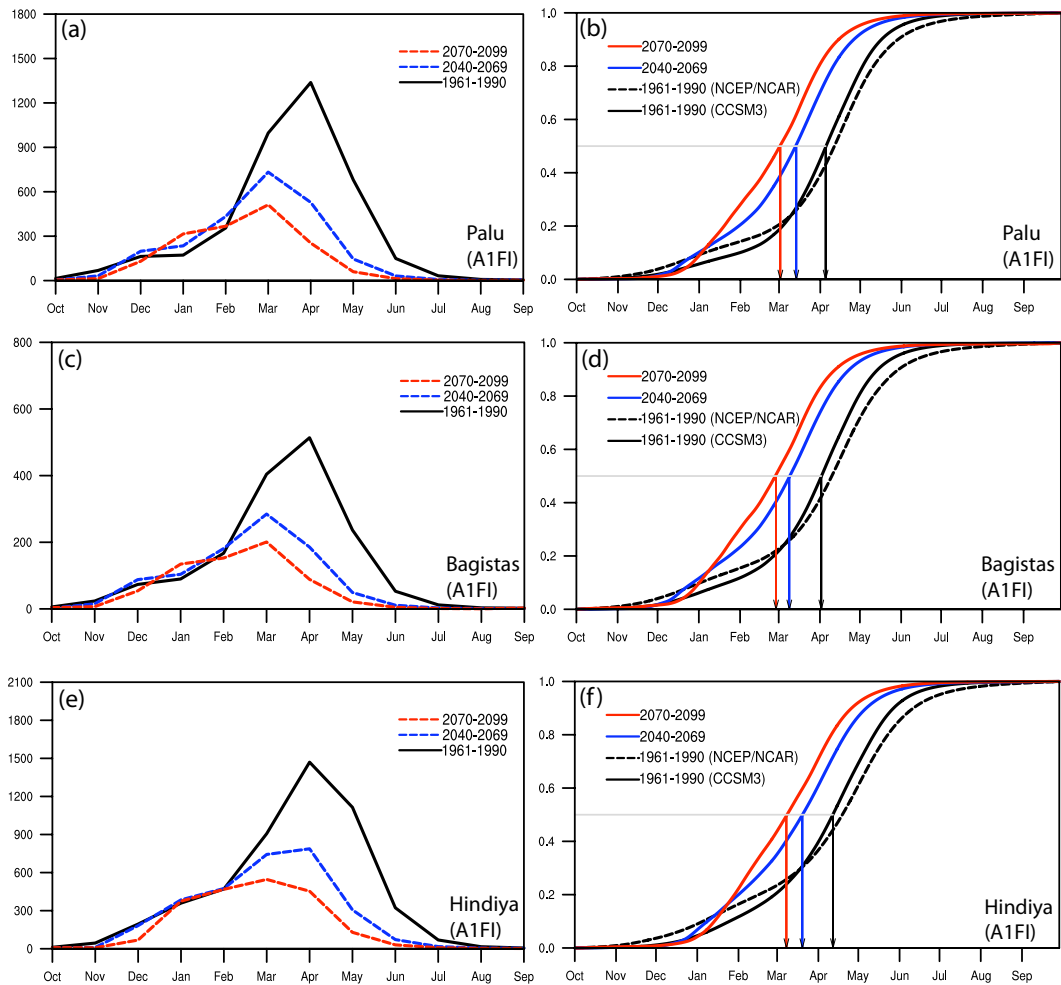
Figure 5.20 : The HDM simulation results of reference (solid line) and future periods (dashed line; blue for mid-century, red for end of the century) forced with dynamically downscaled the CCSM3 A1FI scenario output. Left column corresponds to changes in the mean monthly discharges (m^3/s). Right column corresponds to changes in the fraction of accumulated discharges. Vertical arrows correspond the days when 50% of annual discharge is reached.
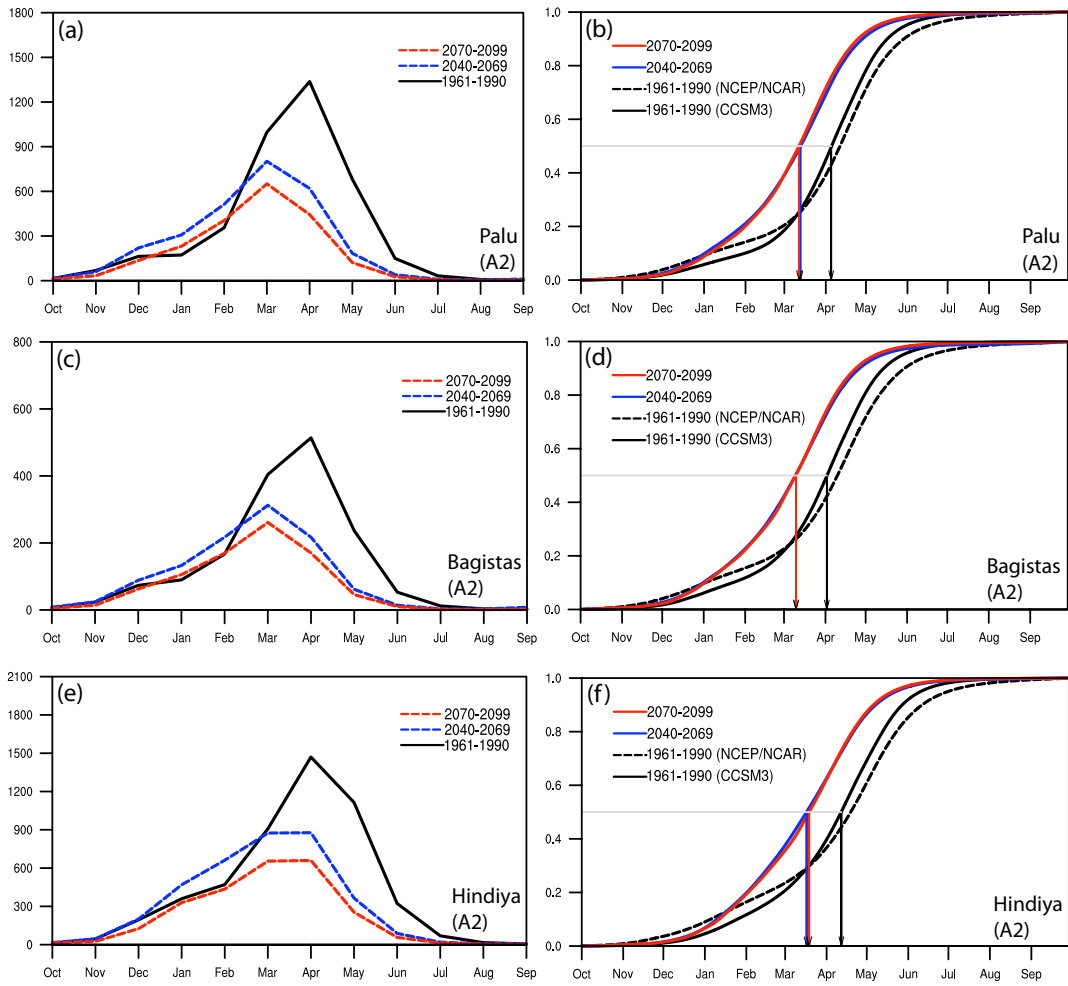
Figure 5.21 : The HDM simulation results of reference (solid line) and future periods (dashed line; blue for mid-century, red for end of the century) forced with dynamically downscaled the CCSM3 A2 scenario output. Left column corresponds to changes in the mean monthly discharges (m^3/s). Right column corresponds to changes in the fraction of accumulated discharges. Vertical arrows correspond the days when 50% of annual discharge is reached.
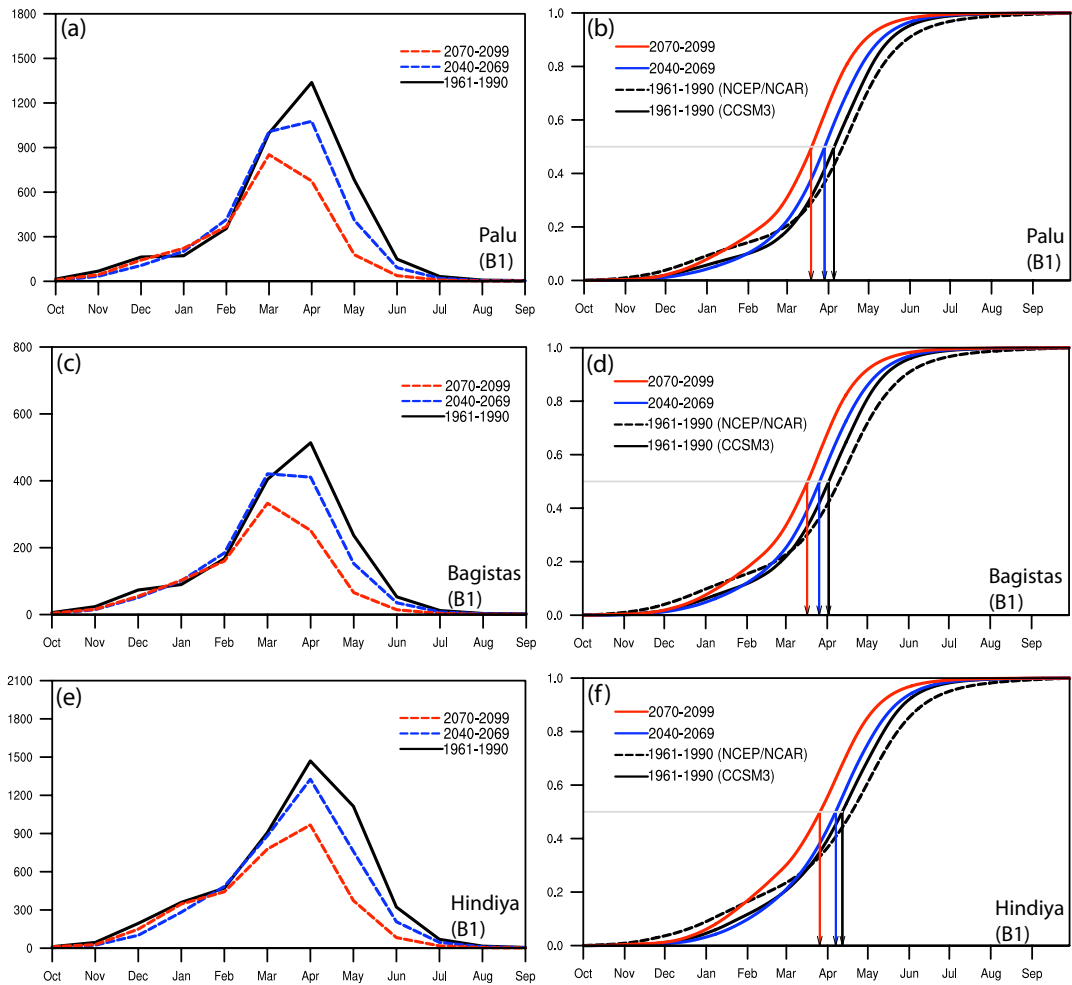
Figure 5.22 : The HDM simulation results of reference (solid line) and future periods (dashed line; blue for mid-century, red for end of the century) forced with dynamically downscaled the CCSM3 B1 scenario output. Left column corresponds to changes in the mean monthly discharges (m^3/s). Right column corresponds to changes in the fraction of accumulated discharges. Vertical arrows correspond the days when 50% of annual discharge is reached.

Table 5.3 : Center time dates of the discharges for Palu, Bağıştaş and Hindiya based on different model and scenario forced simulations.

Palu	1961-1990	2040-2069	2070-2099
ECHAM5 A2	6 April	19 March	3 March
CCSM3 A2	4 April	12 March	11 March
CCSM3 A1FI	4 April	13 March	1 March
CCSM3 B1	4 April	28 March	18 March

Bağıştaş	1961-1990	2040-2069	2070-2099
ECHAM5 A2	3 April	16 March	2 March
CCSM3 A2	1 April	9 March	9 March
CCSM3 A1FI	1 April	8 March	26 February
CCSM3 B1	1 April	25 March	16 March

Hindiya	1961-1990	2040-2069	2070-2099
ECHAM5 A2	10 April	23 March	4 March
CCSM3 A2	11 April	16 March	18 March
CCSM3 A1FI	11 April	20 March	7 March
CCSM3 B1	11 April	6 April	25 March

6. CONCLUSIONS

6.1 Summary and Conclusions

This study aims to provide a compherensive analysis for past and future climate change impacts on the hydrology of the Euphrates-Tigris Basin, which has major water resources of the Middle East, within two research topics: (i) historical climate variability in the basin and (ii) regional hydro-climatological consequences of future climate change in the basin. In order to demonstrate historical climate variability, an investigation of how changes in hydrometeorological variables and large-scale patterns affect regional hydrology in the context of changing climate was carried out using the meteorological and streamflow stations. Hydro-climatic effects of future climate change in the basin have been investigated using dynamically downscaled outputs of different GCM (ECHAM5, CCSM3 and HadCM3)-emissions scenario (A1FI, A2 and B1) simulations via a regional climate model (RegCM3), obtained from a UNDP project (MDG-F 1680) entitled with "Enhancing the capacity of Turkey to adapt to climate change". In addition to analysis of atmospheric model outputs, the impacts of future climate changes on river discharges in the basin have been investigated via a hydrological discharge model (the HDM). Hydrological discharge simulations have been carried out by using surface runoff and drainage outputs of CMIP3 simulations of ECHAM5 and CMIP5 simulations of MPI-ESM-LR under different scenarios (A1B for ECHAM5 and RCP 4.5 for MPI-ESM-LR). In addition to this, the HDM was forced by high resolution RCM outputs of different GCM (ECHAM5, CCSM3) - emissions scenario (A1FI, A2 and B1) simulations.

6.1.1 Observed climate changes

Based on the analyses of temperature, precipitation and streamflow observations in the basin, the following conclusions can be highlighted:

- Trend analysis of long-term temperature data (1961-2002) indicates that there has been a striking temperature increase after the early 1990s for both

highlands and lowlands of the basin. More pronounced and statistically significant increase in minimum temperatures in the main headwaters of the basin is detected.

- In terms of precipitation, both highlands and lowlands have no striking change based on the trend analysis of long-term precipitation data (1961-2002).

- The statistical analysis reveals that there are no significant trends in the annual streamflow data in the main headwaters of the basin (i.e., covering 35 years from 1972 to 2006). However, the streamflow timings of the Euphrates and Tigris Rivers, are found to be shifting to earlier days in the year. Six out of eight stations indicate statistically significant shifts between two consecutive 17-years periods (i.e., 1972-1988 and 1990-2006). Among these stations, the average shift to earlier times is over 5 days, suggesting earlier spring melting of snowpack due to increased temperatures in the second period.

- A striking increase in the discharges takes place during the first half of March, and it is observed at all stream gauging sites in the main headwaters area. An analysis based on the NCEP/NCAR reanalysis data indicates that warming which results in this increase is associated with the switching from the northeasterly flow to southwesterly flow over the Black Sea and western Anatolia caused by the weakening of the Siberian High over eastern Europe. These changes in the circulation features from the first to second periods are found to be very consistent with the positive and negative phases of the North Sea-Caspian pattern.

6.1.2 Hydro-climatic effects of future climate change

6.1.2.1 Atmospheric model simulation results

Hydro-climatic spatial changes for the 2071-2099 period and annual hydro-climatic elevation-based and country-based changes for two future periods, 2041-2070 and 2071-2099, point out the following main findings:

- All scenario simulations indicate surface temperature increases across the entire Euphrates-Tigris basin. The increase is comparatively greater over the

highlands in winter. Increase in annual surface temperature in the highlands ranges between 2.1 °C (lower emissions scenario, B1) and 4.1 °C (higher emissions scenario, A1FI) for 2041-2070, whereas it ranges between 2.6 °C and 6.1 °C for 2071-2099. Cold season temperature increase has the potential to greatly impact the regional hydrological cycle by reducing the snow cover and changing the seasonality of surface runoff.

- In terms of precipitation, there is a broad agreement among the simulations, which indicate a decrease in the highlands and northern parts of the basin and an increase in the southern parts. Our results confirm the findings of the previous studies that demonstrate similar spatial changes of precipitation in the ETB (e.g., Evans, 2008; Önol and Semazzi, 2009; Chenoweth et al., 2011). The changes in precipitation are statistically significant in the large areas of the basin in all simulations except for the ECHAM5 simulation. Precipitation in the highlands is projected to decrease by 33% under the higher emissions scenario (A1FI) simulation of CCSM3 by the end of the present century, whereas the A2 scenario simulations produce a decrease ranging between 6-24%.

- Projected changes in the annual evapotranspiration indicate generally statistically significant decreases in the basin by the end of the century, which is most likely related with the projected decreases in precipitation.

- A striking impact of warming could be seen on the snow water equivalent in the highlands of the basin, which is projected to decrease by 55% for B1 scenario, 77-85% for A2 scenario and 87% for A1FI scenario. Özdoğan (2011) also found substantial declines (between 10% and 60%) in available snow water, particularly under the A2 scenario, by the end of this century using a hydrological model and a set of regional climate change simulations driven by 13 different GCM. The dynamically downscaled simulations in the present study indicate therefore more pronounced declines. It is also found that the greatest relative changes in the snow cover take place in the lower elevations, a result that is also reported by Özdoğan (2011).

- Based on different model and scenario simulations, the annual total surface runoff is found to decrease about 25-55% in the eastern Anatolian mountains (main headwaters of the basin) by the end of the 21st century.

- One of the most striking consequences of the temperature increases in the basin is the 18-39 day shifts to the earlier days in the surface runoff timing for the main headwaters of the basin. By analyzing the observations from the streamflow gauging stations in this region, Sen et al. (2011) found statistically significant shifts to earlier times (over 5 days) in streamflow timing in recent decades (no significant changes in the annual streamflow were detected for the same period). The climate change projections of the present study show significant changes in both total surface runoff and the timing of the surface runoff, which implies that the water resources of the ETB will be dramatically affected by the climate change.

- Country-based assessments indicate that the territory of Turkey will likely experience more adverse direct effects of the climate change compared to the territories of the other countries in the basin. The annual surface runoff is projected to decrease by 26-57% in the territory of Turkey by the end of the present century. Because much of the headwaters are located in this territory, all other countries in the basin are expected to feel the stress for the diminishing waters during the twenty first century.

6.1.2.2 Hydrological discharge simulation results

Based on the hydrological discharge simulations, the following conclusions can be highlighted:

- The HDM validation points out that the simulations forced with low resolution GCM outputs are not able to reproduce seasonal cycle of discharge well. Moreover, the simulations do not capture the timing of the annual peak discharge. These results are mostly related with the shortcomings of the GCM driving fields. Since the surface orography is the main source of the precipitation over the highlands of the basin, coarse resolutions of the GCMs may not adequate to represent the spatial distribution of precipitation. It should be also noted that the simulations forced with the MPI-ESM-LR driving fields yield better results compared to ECHAM5-forced simulations.

- In contrast to GCM-forced simulations, high resolution RCM-forced simulations reasonably reproduce the annual cycle of discharge. However, overestimation of the discharge during the cold season and bias in the timing

of the springtime snowmelt peak of discharge persist in the RCM-forced simulations. Overestimation of discharge can be caused by shortcomings of the RCM, especially related to the annual cycle of precipitation. Indeed, observed annual cycle of precipitation compared with RCM simulations in the upper Euphrates Basin indicate an overestimation of precipitation in the cold season. Moreover, warmer temperature values in transition month (March) may be accounted for high peak discharge values in RCM driven simulations.

• Future hydrological discharge simulations indicate a striking decrease in discharge of the Euphrates River. The decrease is more remarkable by the end of the century. Another important result of the hydrological discharge simulations is that significant temporal shifts to earlier days (3-5 weeks) in the center time of the discharges are projected by the end of the century. Different model and scenario combinations are in agreement with these two main results. High resolution RCM-forced simulations yield more pronounced decreases and shifting compared to the low resolutions GCM-forced simulations.

6.2 Discussions

Based on the results of the present study, it could be said that the changes in the hydroclimatic parameters may have profound impacts on the physical and biological components of the ecosystems in the basin as well as on the socio-economic developments of the basin countries. The most likely adverse impact of the climate change in the Euphrates-Tigris Basin will be the decreased water availability. Combined with the population increase, climate change will further stress the water resources of the downstream countries that rely heavily upon the upstream water. Chenoweth et al. (2011) suggested that per capita water resources of the Middle East is likely to be reduced noticeably due to climate change combined with a rapid population growth. There are still plans and investments to construct more dams on the Euphrates and Tigris rivers. On one hand, decreased water availability and reduced hydropower potential in the future make it questionable to build more dams on these rivers for power generation. On the other hand, the temporal change in the peak flows may make it necessary to build more dams to compensate the diminishing

reservoir attribute of the snow cover to be able to save water for the spring and summer when dry conditions prevail in the basin. Construction of more dams in the basin, however, causes, in addition to environmental problems, irreversible damages to the rich historical and cultural heritage of the region. For instance, planned construction of Ilisu Dam on the Tigris River has already been beginning to affect the biological, historical and cultural heritage of Hasankeyf, which hosts a unique habitat in the upper Mesopotamia (Şekercioğlu et al., 2011).

Being largely located in an arid and semi-arid region, the Euphrates-Tigris Basin has frequent and intense droughts in the past. A severe drought event in the winter of 2007-2008 had a big impact on the crop yield in the basin in 2008. Irrigation related problems (e.g., soil salinization) and changes in land cover combined with the changing climatic conditions (warmer temperatures, altered patterns of precipitation and surface runoff, changes in soil moisture) may further exacerbate the consequences of the future droughts. Land degradation and desertification are other possible impacts of climate change in the Euphrates-Tigris Basin. Changes in geological settlings such as rock slope stability due to continued snow cover decrease over the mountains will result in the rise of the likelihood of the natural hazards such as landslides, debris flows and rock flows especially in the foothills regions. This will also influence the water quality of the basin due to possible changes in erosion patterns and amount of debris carried by.

According to Hemming et al. (2011) larger ranges in the uncertainty of the future precipitation projections of RCM ensemble members compared to GCM ensemble members for the Middle East region indicate that increasing the model resolution might lead to increases in the sensitivity of the modeled precipitation. As they suggest that reducing large uncertainties can be achieved by improving the understanding and modeling of large-scale processes and their teleconnections to the regional climate, with a more focus on localized processes, further modeling studies are needed to analyze and understand the main sources of the modeling uncertainties of the climate of the Euphrates-Tigris Basin and its surroundings. Finally, there is a clear need to inform the societies on the changing hydroclimatological conditions, and comprehensive climate information based on different projections will certainly be important to implement the efficient adaptation measures in the basin.

REFERENCES

Adam, J. C., Hamlet, A. F., and Lettenmaier, D. P. (2009). Implications of global climate change for snowmelt hydrology in the twenty-first century. *Hydrol. Process.,* 23 (7), 962-972.

Akyurek, Z., Surer, S., Beser, Ö. (2011). Investigation of the snow-cover dynamics in the Upper Euphrates Basin of Turkey using remotely sensed snow-cover products and hydrometeorological data. *Hydrol. Process*, 25, 3637-3648. DOI:10.1002/hyp.8090.

Alpert, P., Neumann, J. (1989). An ancient correlation between streamflow and distant rainfall in the Near East. *J Near East. Stud.*, 48**,** 313-314.

Alpert, P., Neeman, B. U., Shay-El, Y. (1990). Climatological analysis of Mediterranean cyclones using ECMWF data. *Tellus*, 42A**,** 65-77.

Ammann, C. M., Meehl, G. A., Washington, W. M., Zender, C. S. (2003). A monthly and latitudinally varying volcanic forcing dataset in simulations of 20th century climate. *Geophys. Res. Lett.,* 30, 1657.

Anthes, R. A. (1977). A cumulus parameterization scheme utilizing a one-dimensional cloud model. *Mon. Wea. Rev.*, 105, 270-286.

Arakawa, A., Schubert, W. H. (1974). Interaction of a cumulus cloud ensemble with the large-scale environment, Part I. *J. Atmos. Sci.*, 31, 674-701.

Barnett, T. P., Adam, J. C., and Lettenmaier, D. P. (2005). Potential impacts of a warming climate on water availability in snow-dominated regions. *Nature*, 438, 303-309.

Barnston, A., Livezey., R. E. (1987). Classification, seasonality and persistence of low-frequency circulation patterns. *Mon. Wea. Rev.*, 115, 1083-1126.

Bartholmes, J., Todini, E. (2005). Coupling meteorological and hydrological models for flood forecasting. *Hydrol. Earth Sys. Sci.*, 9(4), 333-346.

Bell, V. A., Kay, A. L., Jones, R. G., Moore, R. J. (2007). Use of a grid-based hydrological model and regional climate model outputs to assess changing flood risk. *Int. J. Climatol.*, 27, 1657-1671.

Bergant, K., Belda, M., Halenka, T. (2007). Systematic errors in the simulation of European climate (1961-2000) with RegCM3 driven by NCEP/NCAR reanalysis. *Int. J. Climatol.*, 27, 455-472. DOI:10.1002/joc.1413.

Beven, K. (1989). Changing ideas in hydrology: the case of physically-based models. *J. Hydrol.*, 105, 157-172.

Bonan, G. B., Levis, S., Kergoat, L., Oleson, K. W. (2002). Landscapes as patches of plant functional types: An integrating approach for climate and ecosystem models. *Glob. Biogeochem. Cyc.*, 16, 5.1-5.23.

Bonan, G. B. (2002). *Ecological Climatology: Concepts and Applications*. Cambridge University Press.

Bond, G., Kromer, B., Beer, J., Muscheler, R., Evans, M. N., Showers, W., ..., Bonani, G. (2001). Persistent solar influence on North Atlantic climate during the Holocone. *Science*, 294, 2130-2136.

Boville, B. A., Rasch, P. J., Hack, J. J., McCaa, J. R. (2006). Representation of clouds and precipitation processes in the Community Atmosphere Model (CAM3). *J. Climate.*, 19, 2184-2198.

Bozkurt, D., Sen, O. L. (2011). Precipitation in the Anatolian Peninsula: sensitivity to increased SSTs in the surrounding seas. *Clim. Dyn.*, 36 (3-4), 711-726. DOI:10.1007/s00382-009-0651-3.

Bozkurt, D., Turuncoglu, U., Sen, O. L., Onol, B., Dalfes, H. N. (2012). Downscaled simulations of the ECHAM5, CCSM3 and HadCM3 global models for the eastern Mediterranean-Black Sea region: Evaluation of the reference period. *Clim. Dyn.*, 39 (1-2), 207-225. DOI:10.1007/s00382-011-1187-x.

Bozkurt, D., Sen, O. L. (2013). Climate change impacts in the Euphrates-Tigris Basin based on different model and scenario simulations. *J. Hydrol.*, 480, 149-161. DOI:10.1016/j.hydrol.2012.12.021.

Brandt, R. E., Warren, S. G., Grenfell, T. C., Worby, A. P. (2005). Surface albedo of the Antarctic sea ice zone. *J. Climatol.*, 18, 3606-3622.

Briegleb, B. P., Bitz, C. M., Hunke, E. C., Lipscomb, W. H., Holland, M. M., Schramm, J. L., Moritz, R. E. (2004). Scientific description of the sea ice component in the Community Climate System Model, Version Three. *Tech. Rep. NCAR/TN-463+STR*, NCAR, Boulder, CO, 78 pp.

Brinkman, J. A. (1968). *A political history of post-Kassite Babylonia*, 1158-722 BC. Analecta Orientalia, Ville.

Brovkin, V., Raddatz, T., Reick, C. H., Claussen, M., Gayler, V. (2009). Global biogeophysical interactions between forest and climate. *Geophys. Res. Lett.*, 36, L07405. DOI:10.1029/2009GL037543.

Brovkin, V., Boysen, L., Raddatz, T., Gayler, V., Loew, A., Claussen, M., (2012). Evaluation of vegetation cover and land-surface albedo in MPI-ESM CMIP5 simulations. *J. Adv. Model. Earth Sys.*, accepted.

Busioc, A., Von Storch, H., Schnur, R. (1999). Verification of GCM-generated regional seasonal precipitation for current climate and of statistical downscaling estimates under changing climate conditions. *J. Clim.*, 12, 258-272.

Cayan, D. R., Kammerdiener, S., Dettinger, M. D., Caprio, J. M., Peterson, D. H. (2001). Changes in the onset of spring in the western United States. *Bull. Amer. Meteor. Soc.*, 82, 399-415.

Chenoweth, J., Hadjinicolaou, P., Bruggeman, A., Lelieveld, J., Levin, Z., Lange, M. A., ..., Hadjikakou, M. (2011). Impact of climate change on the water resources of the eastern Mediterranean and Middle East region: Modeled 21st century changes and implications. *Water. Resour. Res.*, 47, W06506. DOI: 10.1029/2010WR010269.

Chow, V. T. (1998). *Applied Hydrology*. McGraw-Hill Inc., 572 pp.

Christensen, N. S., Wood, A. W., Voisin, N., Lettenmaier, D. P., Palmer, R. N. (2004). Effects of climate change on the hydrology and water resources of the Colorado river basin. *Clim. Change*, 62, 337-363.

Clarke, L. E., Edmonds, J. A., Jacoby, H. D., Pitcher, H., Reilly, J. M., Richels, R. (2007). Scenarios of greenhouse gas emissions and atmospheric concentrations. *Sub-report 2.1a of Synthesis and Assessment Product 2.1. Climate Change Science Program and the Subcommittee on Global Change Research*, Washington DC.

Collins, W. D. (2001). Parameterization of generalized cloud overlap for radiative calculations in general circulation models. *J. Atmos. Sci.*, 58, 3224-3242.

Collins, W. D., Hackney, J. K., Edwards, D. P. (2002a). A new parameterization for infrared emission and absorption by water vapor in the National Center for Atmospheric Research Community Atmosphere Model. *J. Geophys. Res.*, 107, 8028. DOI:10.1029/2000JD000032.

Collins, W. D., Rasch, P. J., Eaton, B. E., Fillmore, D. W., Kiehl, J. T., Beck, T. C., Zender, C. S. (2002b). Simulation of aerosol distributions and radiative forcing for INDOEX: Regional climate impacts. *J. Geophys. Res.*, 107, 4664. DOI:10.1029/2001JD001365.

Collins, W. D., et al. (2004). Description of the NCAR Community Atmosphere Model (CAM3). *Tech. Rep. NCAR/TN-464+STR*, NCAR, Boulder, CO, 226 pp.

Collins, W. D., et al. (2006a). The community climate system model version 3 (CCSM3). *J. Clim.*, 19 (11), 2122-2143.

Collins, W. D., et al. (2006b). The formulation and atmospheric simulation of the Community Atmosphere Model version 3 (CAM3). *J. Clim.*, 19, 2144-2161.

Collins, W. D., Lee-Taylor, J. M., Edwards, D. P., Francis, G. L. (2006c). Effects of increased near-infrared absorption by water vapor on the climate system. *J. Geophys. Res.*, 111, D18109. DOI:10.1029/2005JD006796.

Connolley, W. M., Gregory, J. M., Hunke, E. C., McLaren, A. J. (2004). On the consistent scaling of terms in the sea-ice dynamics equation. *J. Phys. Oceanogr.*, 34, 1776-1780.

Coppola, E., Tomassetti, B., Mariotti, L., Verdecchia, M., Visconti, G. (2007). Cellular automata algorithms for drainage network extraction and rainfall data assimilation. *Hydrol. Sci.*, 52(3), 579-592.

Cox, P. (1984). A primitive equation, 3 dimensional model of the ocean. *GDFL Ocean Group Technical Rep. 1*, Princeton, NJ, USA, 143 pp.

Cox, P., Betts, R., Bunton, C., Essery, R, Rowntree, P. R., Smith, J. (1998). The impact of new land surface physics on the GCM simulation of climate and climate sensitivity. *Clim. Dyn.*, 15, 183-203.

Cullen, H. M., deMenocal, P. B. (2000). North Atlantic Influence on Tigris-Euphrates Streamflow. *Int. J. Climatol.*, 20 (8), 853-863.

Cullen, H. M., Kaplan, A., Arkin, P. A., deMenocal, P. B. (2002). Impact of North Atlantic Oscillation on Middle Eastern climate and streamflow. *Climatic Change*, 55 (3), 315-338.

Cusack, S., Slingo, A., Edwards, J. M., Wild, M. (1998). The radiative impact of a simple aerosol climatology on the Hadley Centre climate model. *Quart. J. Roy. Meteor. Soc.*, 124, 2517-2526.

Daoudy, M. (2004). *Syria and Turkey in water diplomacy (1962-2003). Water in the Middle East and in North Africa: Resources, Protection and Management*, Zereini, F., and Jaeschke, W. (eds). Springer.

deMenocal, P. B. (2001). Cultural responses to climate change during the late Holocene. *Science*, 292, 667-673.

Dickinson, R. E., Henderson-Sellers, A., Kennedy, P. J. (1993). Biosphere-atmosphere transfer scheme (BATS) version 1e as coupled to the NCAR community climate model. *Tech. Note. TN-387+STR*, NCAR, 72 pp.

Dickinson, R. E., Oleson, K. W., Bonan, G., Hoffman, F., Thornton, P., Vertenstein, ..., Zeng, X. (2006). The Community Land Model and its climate statistics as a component of the Community Climate System Model *J. Clim.*, 19, 2302-2324.

Duffy, P. B., Arritt, R. W., Coquard, J., Gutowski, W., Han, J., Iorio, J., ..., Zeledon, E. (2006). Simulations of present and future climates in the Western United States with four nested regional climate models. *J. Clim.*, 19, 873-895.

Dümenil, L., Todini, E. (1992). A rainfall-runoff scheme for use in the Hamburg climate model. In: Advances in Theoretical Hydrology, A Tribute to James Dooge, edited by Kane, J. O. *European Geophysical Society Series on Hydrological Sciences*, 129-157 pp. Elsevier, Amsterdam.

Edwards, J. M., Slingo, A. (1996). Studies with a flexible new radiation code. I: Choosing a configuration for a large-scale model. *Quart. J. Roy. Meteor. Soc.*, 122, 689-719.

Emanuel, K. A. (1991). A scheme for representing cumulus convection in large-scale models. *Quart. J. Roy. Meteor. Soc.*, 48, 2313-2335.

Emanuel, K. A., Zivkoviç-Rothman, M. (1999). Development and evaluation of a convection scheme for use in climate models. *J. Atmos. Sci.*, 56, 1766-1782.

Evans, J. P., Smith, R. B., Oglesby, R. J. (2004). Middle East climate simulation and dominant precipitation processes. *Int. J. Climatol.*, 24, 1671-1694.

Evans, J. P. (2008). Changes in water vapor transport and the production of precipitation in the eastern Fertile Crescent as a result of global warming. *J. Hydromet.*, 9, 1390-1401. DOI:10.1175/2008JHM998.1.

Food and Agriculture Organization (FAO) (2009). Irrigation in the Middle East region in figures: AQUASTAT Survey – 2008. *FAO Water Reports 34*. Edited by Frenken, K. Rome.

Fouquart, Y., Bonnel, B. (1980). Computations of solar heating of the earth's atmosphere: A new parameterization. *Beitr. Phys. Atmos.*, 53, 35-62.

Fritsch, J. M., Chappel, C. F. (1980). Numerical prediction of convectively driven mesoscale pressure systems. Part 1 Convective parameterization, *J. Atmos. Sci.*, 37, 1722-1733.

Fujihara, Y., Tanaka, K., Watanabe, T., Nagano, T., Kojiri, T. (2008). Assessing the impacts of climate change on the water resources of the Seyhan River Basin in Turkey: Use of dynamically downscaled data for hydrologic simulations. *J. Hydrol.*, 353, 33-48.

Gao, X., Pal, J. S., Giorgi, F. (2006). Projected changes in mean and extreme precipitation over the Mediterranean region from high resolution double nested RCM simulations. *Geophys. Res. Lett.*, 33, L03706.

Giorgi, F., Bates, G. T., Nieman, S. J. (1993a). The multi-year surface climatology of a regional atmospheric model over the western United States. *J. Clim.*, 6, 75-95.

Giorgi, F., Marinucci, M. R., Bates, G. T., DeCanio, G. (1993b). Development of a second generation regional climate model (RegCM2). Part II: Convective processes and assimilation of lateral boundary conditions. *Mon. Wea. Rev.*, 121, 2814-2832.

Giorgi, F., Shields, C., Bates, G. T. (1994). Regional climate change scenarios over the United States produced with a nested regional climate model. *J. Clim.*, 7, 375-399.

Giorgi, F., Francisco., R. (2000). Uncertainties in regional climate change predictions. A regional analysis of ensemble simulations with the HADCM2 GCM. *Clim. Dyn.*, 16, 169-182.

Giorgi, F., Bi, X., Pal, J. S. (2004a). Mean, interannual variability and trends in a regional climate change experiment over Europe, I. Present day climate (1961-1990). *Clim. Dyn.*, 22, 733-756.

Giorgi, F., Bi, X., Pal, J. S. (2004b). Mean, interannual variability and trends in a regional climate change experiment over Europe, II. Climate change scenarios (2071-2100). *Clim. Dyn.*, 23, 839-858.

Giorgi, F. (2006). Climate change hot-spots. *Geophys. Res. Lett.*, 33, L08707. DOI:10.1029/2006GL025734.

Gordon, C., Cooper, C., Senior, C. A., Banks, H., Gregory, H. M., Johns, T. C., ..., Wood, R. A. (2000). The simulation of SST, sea ice extent and ocean heat transports in a version of the Hadley Centre coupled model without flux adjustments. *Clim. Dyn.*, 16, 147-168.

Gregory, D., Rowntree, P. (1990). A mass flux convection scheme with representation of cloud ensemble characteristics and stability-dependent closure. *Mon. Wea. Rev.*, 118, 1483-1506.

Gregory, D., Kershaw, R., Innes, P. (1997). Parametrization of momentum transport by convection. Part II: Tests in single-column and general circulation models. *Quart. J. Roy. Meteor. Soc.*, 123, 1153-1183.

Gregory, J. M., Stott, P. A., Cresswell, J., Rayner, N. A., Gordon, C., Sexton, D. M. H. (2002). Recent and future changes in Arctic Sea ice simulated by the HadCM3 AOGCM. *Geophys. Res. Lett.*, 29 (24), 2175, DOI:10.1029/2001HL014575.

Grell, F. (1993). Prognostic evaluation of assumptions used by cumulus parameterization. *Mon. Wea. Rev.*, 121, 764-787.

Gruen, G. E. (2000). Turkish waters: Source of regional conflict or catalyst for peace? *Water, Air, and Soil Pollution*, 123, 565-579.

Hagemann, S., Dümenil, L. (1998). A parametrization of the lateral waterflow for the global scale. *Clim. Dyn.*, 14 (1), 17-31.

Hagemann, S., Dümenil-Gates, L. (2001). Validation of the hydrological cycle of ECMWF and NCEP reanalyses using the MPI hydrological discharge model. *J. Geophys.* Res, 106, 1503-1510.

Hagemann, S. (2002). An improved land surface parameter dataset for global and regional climate models. *Max Planck Institute for Meteorology Report*, 336.

Hagemann, S., Loew, A., Andersson, A. (2012). Combined evaluation of MPI-ESM land surface water and energy fluxes. *J. Adv. Model. Earth Sys.*, DOI:10.1029/2012MS000173.

Han, J., Roads, J. (2004). U.S. climate sensitivity simulated with the NCEP regional spectral model. *Clim. Change*, 62, 115-154.

Hay, L. E., Clark, M. P., Wilby, R. L., Gutowski, W. J., Leavesley, G. H., Pan, ..., Takle, E. S. (2002). Use of regional climate model output for hydrologic simulations. *J. Hydromet.*, 3 (5), 571-590.

Hayhoe, K., Wake, C. P., Huntington, T. G., Luo, L., Schwartz, M. D., Sheffield, ..., Wolfe, D. (2007). Past and future changes in climate and hydrological indicators in the U.S. Northeast. *Clim. Dyn.*, 28, 381-407. DOI:10.1007/s00382-006-0187-8.

Hemming, D., Buontempo, C., Burke, E., Collins, M., Kaye, N. (2011). How uncertain are climate model projections of water availability indicators across the Middle East. *Philos. Trans. Roy. Soc.*, 368, 5117-5135. DOI:10.1098/rsta.2010.0174.

Holstag, A. A. M., DeBruijn, E. I. F., Pan, H. L. (1990). A high resolution air mass transformation model for short range weather forecasting. *Mon. Wea. Rev.*, 118, 1561-1575.

Holstag, A. A. M., Boville, B. (1993). Local versus non-local boundary layer difussion in a global climate model. *J. Climatol.*, 6, 1825-1842.

Houghton, J. T., Jenkins, G. J., Ephraums, J. J. (Ed.) (1990). *Climate Change. The IPCC Assessment.* Cambridge University Press.

Hsie, E. Y., Anthes, R. A., Keyser, D. (1984). Numerical simulation of frontogenisis in a moist atmosphere. *J. Atmos. Sci.*, 41, 2581-2594.

Hu, Z. Z., Wu, A. (2004). The intensification and shift of the annual North Atlantic Oscillation in a global warming scenario simulation. *Tellus*, 56A, 112-124.

Huntingford, C., Jones, R. G., Prudhomme, C., Lamb, R., Gash, J. H. C., Jones, D. A. (2003). Regional climate model predictions of extreme rainfall for a changing climate. *Quart. J. Roy. Meteor. Soc.*, 129, 1607-1622.

Hurrel, J. W. (1995). Decadal trends in the North Atlantic Oscillation: Regional temperatures and precipitation. *Science*, 269, 676-679.

Immerzeel, W. W., van Beek, L. P. H., Bierkens, M. F. P. (2010). Climate change will affect the Asian water towers. *Science*, 328, 1382-1385.

IPCC SRES (2000). *Special Report on Emission Scenarios: A special report of Working Group III of the Intergovernmental Panel on Climate Change*. N., Nakicenovic, N., R., Swart, (Ed.), Cambridge University Press, Cambridge, UK, 599 pp.

IPCC (2007). *Intergovernmental Panel on Climate Change fourth assessment report on scientific aspects of climate change for researchers, students, and policymakers*. Genewa, Switzerland, 28 pp.

Johns, T. C., Carnell, R. E., Crossley, J. F., Gregory, J. M., Mitchell, J. F. B., Senior, C. A., ..., Wood, R. A. (1997). The second Hadley Centre coupled ocean-atmosphere GCM: Model description, spinup, and validation. *Clim. Dyn.*, 13, 103-134.

Jungclaus, J. H., Fischer, N., Haak, H. Lohmann, K., Marotzke, J., Matei, D., ..., von Storch, J. S. (2012). Characteristics of the ocean simulations in MPIOM, the ocean component of the MPI Earth System Model. *J. Adv. Model. Earth Sys*, accepted.

Kalnay, E., Kanamitsu, M., Kistler, R., et al. (1996). The NCEP/NCAR 40-Year Reanalysis Project. *Bull. Am. Meteor. Soc.*, 77, 437-471.

Kaniewski, D., Paulissen, E., Van Campo, E., Weiss, H., Otto, T., Bretschneider, J., Van Lerberghe, K. (2010). Late second-early first millennium BC abrupt climate change in coastal Syria and their possible significance for the history of the Eastern Mediterranean. *Quatern. Res.*, 74, 207-215.

Kavvas, M. L., Chen, Z. Q., Anderson, M. L., Ohara, N., Yoon, J. Y., Xiang, F. (2011). A study of water balances over the Tigris-Euphrates watershed. *Phys. Chem. Earth*, 36, 197-203.

Kay, P. A., Johnson, D. L. (1981). Estimation of the Tigris-Euphrates streamflow from regional paleoenvironmental proxy data. *Climatic Change*, 3, 251-263.

Kendall, M. G. (1970). *Rank Correlation Methods*. (2nd ed.). New York: Hafner.

Kiehl, J. T., Hack, J. J., Bonan, G. B., Boville, B. A., Briegleb, B. P., Williamson, D. L., Rasch, P. J. (1996). Description of the NCAR Community Climate Model (CCM3). *NCAR Tech. Note, NCAR/TN-420+STR*, 152 pp.

Kitoh, A., Yatagai, A., Alpert, P. (2008). First super-high-resolution model projection that the ancient "Fertile Crescent" will disappear in this century. *Hydrol. Res. Lett.*, 2, 1-4. DOI:10.3178/HRL.2.1.

Kolars, J. F., Mitchell, W. A. (1991). *The Euphrates River and the Southeast Anatolia Development Project*. Southern Illinois University Press.

Krichak, S. O., Alpert, P., Kunin, P. (2010). Numerical simulation of seasonal distribution of precipitation over the eastern Mediterranean with a RCM. *Clim. Dyn.*, 34, 47-59.

Kutiel, H., Benaroch, Y. (2002). North Sea-Caspian Pattern (NCP) - an upper level atmospheric teleconnection affecting the Eastern Mediterranean: Identification and definition. *Theor. Appl. Climatol.*, 71, 17-28.

Kutiel, H., Maheras, P., Türkeş, M., Paz, S. (2002). North Sea-Caspian Pattern (NCP) - an upper level atmospheric teleconnection affecting the Eastern Mediterranean - Implications on the regional climate. *Theor. Appl. Climatol.*, 72, 173-192.

Kutiel, H., Maheras, P., Türkeş, M., Paz, S. (2002). North Sea-Caspian Pattern (NCP) - an upper level atmospheric teleconnection affecting the Eastern Mediterranean - Implications on the regional climate. *Theor. Appl. Climatol.*, 72, 173-192.

Libscomb, W. H., Hunke, E. C. (2004). Modeling sea-ice transport using incremental remapping. *Mon. Wea. Rev.*, 132, 1341-1354.

Lin, S. J., Rood, R. B. (1996). Mutlidimensional flux form semi-Lagrangian transport. *Mon. Wea. Rev.*, 124, 2046-2068.

Lin, C. A., Wen, L., Lu, G., Wu, Z., Zhang, J., Yang, Y., Zhu, Y., Tong, L. (2006). Atmospheric- hydrological modeling of severe precipitation and floods in the Huaihe River Basin, China. *J. Hydrol.*, 330, 249-259.

Lionello, P., Malanotte-Rizzoli, P., Boscolo, R. (Ed.) (2006). Cyclones in the Mediterranean region: climatology and effects on the evironment. *Mediterranean Climate Variability*. Elsevier, Amsterdam, 325-372.

Mann, H. B. (1945). Nonparametric tests against trend. *Econometrica*, 13, 245-259.

Martinez-Castro, D., da Rocha, R. P., Bezanilla-Morlot, A., Alvarez-Escudero, L., Reyes-Fernandez, J. P., Silva-Vidal, Y., Arritt, R. W. (2006). Sensitivity studies of the RegCM3 simulation of summer precipitation, temperature and local wind field in the Caribbean Region. *Theor. Appl. Climatol.*, 86, 5-22.

McGregor, J. L. (1997). Regional climate modeling. *Meteorol. Atm. Phys.*, 63, 105-117.

Messager, C., Gallee, H., Brasseur, O. (2004). Precipitation sensitivity to regional SST in a regional climate simulation during the West African monsoon for two dry years. *Clim. Dyn.*, 22, 249-266.

Mitchell, T. D., Jones, P. D. (2005). An improved method of constructing a database of monthly climate observations and associated high-resolution grids. *Int. J. Climatol.*, 25, 693-712.

Mlawer, E. J., et al. (1997). Radiative transfer for inhomogeneous atmospheres: RRTM, a validated correlated-k model for the longwave. *J. Geophys. Res.*, 102, 16663-16682.

Moss, R. H., Edmonds, J. A., Hibbard, K. A., Manning, M. R., Rose, S. K., van Vuuren, D. P., ..., Wilbanks, T. J. (2010). The next generation of scenarios for climate change research and assessment. *Nature*, 463, 747-756.

Nakicenovic, N., et al. (2000). *A special report of Working Group III of the Intergovernmental Panel on Climate Change*. Cambridge University Press, Cambridge, UK, 599 pp.

Neumann, J., Parpola, S. (1987). Climatic change and the eleventh-tenth-century eclipse of Assyria and Babylonia. *J. Near East. Stud.*, 46, 161-182.

Nicoll, K. (2009). Landscape development within a young collision zone: implications for post-Tethyan evolution of the Upper Tigris River system in southeastern Turkey. *Int. Geol. Rev.*, 1-19.

Nohara, D., Kitoh, A., Hosaka, M., Oki, T. (2006). Impact of climate change on river discharge projected by multi-model ensemble. *J. Hydromet.*, 7, 1076-1089.

Nordeng, T. E. (1994). Extended versions of the convective parameterization scheme at ECMWF and their impact on the mean and transient activity of the model in the tropics. *Technical Memorandum*, 206, ECMWF, Reading, UK.

Oleson, K. W., et al. (2004). Technical description of the Community Land Model (CLM). *Tech. Rep. NCAR/TN-461+STR*, NCAR, Boulder, CO, 174 pp.

Önol, B. (2007). Downscaling climate change scenario using regional climate model over eastern Mediterranean. *PhD Thesis*, Istanbul Technical University.

Önol, B., Semazzi, F. H. M. (2009). Regionalization of climate change simulations over Eastern Mediterranean. *J. Climatol.*, 22, 1944-1961.

Özdoğan, M. (2011). Climate change impacts on snow water availability in the Euphrates-Tigris basin. *Hydrol. Earth Syst. Sci.*, 15, 2789-2803. DOI:10.5194/hess-15-2789-2011.

Pal, J. S., Smal, E. E., Eltahir, E. A. B. (2000). Simulation of regional-scale water and energy budgets: representation of subgrid cloud and precipitation processes within RegCM. *J. Geophys. Res.*, 105 (D24), 29579-29594. DOI:10.1029/2000JD900415.

Pal, J. S., Giorgi, F., Bi, X., et al. (2007). Regional climate modeling for the developing world: the ICTP RegCM3 and RegCNET. *Bull. Am. Meteorol. Soc.*, 88 (9), 1395-1409.

Perovich, D. K., Grenfell, T. C., Light, B., Hobbs, P. V. (2002). Seasonal evolution of the albedo multiyear Arctic sea ice. *J. Geophys. Res.*, 107, 8044.

Rasch, P. J., Collins, W. D., Eaton, B. E. (2001). Understanding the Indian Ocean Experiment (INDOEX) aerosol distributions with an aerosol assimilation. *J. Geophys. Res.*, 106, 7337-7356.

Rayner, N. A., Parker, D. E., Horton, E. B., Folland, C. K., Alexander, L. V., Rowell, D. P., Kent, E. C., Kaplan, A. (2003). Global analyses of sea surface temperature, sea ice, and nigh marine temperature since the late nineteenth century. *J. Geophys. Res. Atmos.*, 108 (D14), 4407. DOI:10.1029/2002JD002670.

Rockel, B., Raschke, E., Weyres, B. (1991). A parameterization of broad band relative transfer properties of water, ice, and mixel clouds. *Beitr. Phys. Atmos.*, 64, 1-12.

Roeckner, E., Bauml, G., Bonaventura, L., Brokopf, R., Esch, M., Giorgetta, M., ..., Tompkins, A. (2003). The atmospheric general circulation model ECHAM5. Part I: Model description. *Max Planck Institute for Meteorology Report*, 349, 127 pp.

Roeckner, E., Brokopf, R, Esch, M, Giorgetta, M., Hagemann, S., Kornblueh, L., ..., Schulzweida, U. (2004). The atmospheric general circulation model ECHAM5. Part II: Sensitivity of simulated climate to horizontal and vertical resolution. *Max Planck Institute for Meteorology Report*, 354, 56 pp.

Rohling, E. J., Hilgen, F. J. (1991). The eastern Mediterranean climate at times of sapropel formation: a review. *Geologie en Mijnbouw*, 70, 253-264.

Romem, M., Ziv, B., Saaroni, H. (2007). Scenarios in the development of Mediterranean cyclones. *Adv. Geosci.*, 12, 59-65.

Russel, G. L., Gornitz, V., Miller, J. R. (2000). Regional sea-level changes projected by the NASA/GISS atmosphere-ocean model. *Clim. Dyn.*, 16, 789-797.

SAPRDA (2009). Southeastern Anatolian Project Regional Development Administration. Retrieved December 5, 2010 from http://www.gap.gov.tr/english.

Schmitd, G. A., Bitz, C. M., Mikolajewicz, U., Tremblay, L. B. (2004). Ice-ocean boundary conditions for coupled models. *Ocean Modell*, 7, 59-74.

Schulz, J. P., Dümenil, L., Polcher, J. (2001). On the land surface-atmosphere coupling and its impact in a single-column atmospheric model. *J. Appl. Meteorol.*, 40, 642-663.

Sen, O. L., Wang, B., Wang, Y. (2004a). Impacts of re-greening the desertified lands in northwestern China: Implications from a regional climate model experiment. *J. Met. Soc. Japan*, 82 (6), 1679-1693.

Sen, O. L., Wang, Y., Wang, B. (2004b). Impact of Indochina deforestation on the East-Asian summer monsoon. *J. Climatol.*, 17, 1366-1380.

Sen, O. L., Unal, A., Bozkurt, D., Kindap, T. (2011). Temporal changes in the Euphrates and Tigris discharges and teleconnections. *Environ. Res. Lett.*, **6**, 024012. DOI:10.1088/1748-9326/6/2/024012.

Seth, A., Rauscher, S. A., Camargo, S. J., Qian, J. H., Pal, J. S. (2007). RegCM3 regional climatologies for South America using reanalysis and ECHAM global model driving fields. *Clim. Dyn.*, 28, 461-480. DOI:10.1007/s00382-006-0191-z.

Simmons, A. J., et al. (1989). The ECMWF medium-range prediction model: Development of the numerical formulations and the impact of increased resolution. *Meteorol. Atmos. Phys.*, 40, 28-60.

Singh, V. P. (1998). Hydrological Systems: Rainfall-Runoff Modeling. Ed. by Fellows, C. 1 Englewood Cliffs, New Jersey: Prentice Hall, 480 pp.

Singh, P., Bengtsson, L. (2004). Hydrological sensitivity of a large Himalayan basin to climate change. *Hydrol. Process*, 18, 2363-2385.

Smith, R. (1993). Unified model documentation paper no. 24. *Tech. Rep.*, Meteorological Office, UK.

Smith, R. D., Gent, P. R. (2002). Reference manual for the Parallel Ocean Program (POP), ocean component of the Community Climate System Model (CCSM2.0 and 3.0). *Tech. Rep. LA-UR-02-2484*, Los Alamos National Laboratory.

Sorooshian, S., Hsu, K. L., Coppola, E., Tomasetti, B., Verdecchia, M., Visconti, G. (eds) (2008). *Hydrological Modelling and the Water Cycle: Coupling the Atmospheric and Hydrological Models*. Springer, 291 pp.

Stevens, B., et al. (2012). The atmospheric component of the MPI-M earth system model: ECHAM6. *J. Adv. Model. Earth Sys*, DOI:10.1002/jame.20015.

Stewart, I. T., Cayan, D. R., Dettinger, M. D. (2005). Hydrological sensitivity of a large Himalayan basin to climate change. *Hydrol. Process*, 18, 2363-2385.

Sundqvist, H., Berge, E., Kristjansson, J. (1989). The effects of domain choice on summer precipitation simulation and sensitivity in a regional clime model. *J. Climatol.*, 11, 2698-2712.

Sylla, B., Coppola, E., Mariotti, L., Giorgi, F., Ruti, P. M., Dell'Aquila, A., Bi, X. (2010). Multiyear simulation of the African climate using a regional climate model (RegCM3) with the high resolution ERA-interim reanalysis. *Clim. Dyn.*, 35, 231-247. DOI: 10.1007/s00382-009-0613-9.

Şekercioğlu, Ç. H., et al. (2011). Turkey's globally important biodiversity in crisis. *Biol. Conserv.*, 144, 2752-2769.

Tiedtke, M. (1989). A comprehensive mass flux scheme for cumulus parameterization in large-scale models. *Mon. Wea. Rev.*, 117, 1779-1800.

Tomassetti, B., Coppola, E., Verdecchia, M., Visconti, G. (2005). Coupling a distributed grid based hydrological model and MM5 meteorological model for flooding alert mapping. *Adv. in Geosci.*, 2, 59-63.

Tribe, A. (1992). Automated recognition of valley lines and drainage networks from grid digital elevation models: a review and a new method. *J. Hydrol.*, 139, 263-293.

Trigo, R. M., Pozo-Vazquez, D., Osborn, T. J., Castro-Diez, J., Gamiz-Fortis, S., Esteban-Parra, M. J. (2004). North Atlantic Oscillation influence on precipitation, river flow and water resources in the Iberian Peninsula. *Int. J. Climatol.*, 24, 925-944.

Türkeş, M., Erlat, E. (2009). Winter mean temperature variability in Turkey associated with the North Atlantic Oscillation. *Meteorol. Atmos. Phys.*, 105, 211-225.

Url-1 *<http://www.utexas.edu/courses/classicalarch/images2/mapane.jpg>*. Retrieved March 5, 2012.

Url-2 < http://regclim.coas.oregonstate.edu >. Retrieved February 19, 2013.

USCB (2009). United States Census Bureau, International Data Base. Retrieved August 5, 2009 from http://www.census.gov/ipc/www/idb.

van Vuuren, et al. (2011). The representative concentration pathways: an overview. *Climatic Change*, 109, 5-31. DOI:10.1007/s10584-011-0148-z.

Verdecchia, M., et al. (2008). Flood forecast in complex orography coupling distributed hydro-meteorological models and in-situ and remote sensing data. *Meteorol. Atmos. Phys.*, 101, 267-285.

Visbech, M. H., Hurrel, J. W., Polvani, L., Cullen, H. M. (2001). The North Atlantic Oscillation: past, present, and future. *Proc. Nat. Acad. Sci.*, 98, 12876-7.

Yuan, F., Ren, L. L. (2004). Methodology of a grid-based hydrological model and its application. *Environmental hydraulics and sustainable water management, Proceedings of the 4th International Symposium on Environmental Hydraulics and the 14th Congress of Asia and Pacific Division*, International Association of Hydraulic Engineering and Research.

Xu, C. (1999). Climate change and hydrological models: A review of existing gaps and recent research developments. *Water Res. Manag.*, 13, 369-382.

Walshaw, S. C. (1999). Reconstruction of environment in early bronze age Syria through phytolith analysis on human dental calculus. *MSc Thesis*, University of Alberta.

Wang, Y., Leung, L. R., McGregor, J. L., Lee, D., Wang, W., Ding, Y., Kimura, F. (2004). Regional climate modeling: progress challenges and prospects. *J. Met. Soc. Japan*, 82, 1599-1628.

Wang, G. (2005). Agricultural drought in a future climate: Results from 15 global climate models participating in the IPCC 4th Assessment. *Clim. Dyn.*, 25, 739-753.

Weiss, H. (1982). The decline of the Late Bronze Age civilization as a possible response to climate change. *Climatic Change*, 4, 173-198.

Weiss, H. (1986). The origins of Tell Leilan and the conquest of space in third millennium Mesopotamia. In Weiss, H. (ed.): *The Origins of Cities in Dry-Farming Syria and Mesopotamia in the Third Millennium.* Connecticut Four Quarters, 71-108 pp.

Weiss, H., Courty, M. A., Wetterstrom, W., Guichard, F., Senior, L., Meadow, R., Curnow, A. (1993). The genesis and collapse of third millennium north Mesopotamian civilization. *Science*, 261, 995-1004.

Wilby, R. L., Hay, L. E., Gutowski, W. J., Arritt, R. W., Takle, E. S., Pan, Z., ..., Clark, M. P. (2000). Hydrological responses to dynamically and statistically downscaled climate model outputs. *Geophys. Res. Lett.*, 27 (8), 1199-1202.

Zakharova, E., Kouraev, A., Al-Yamani, F., Polikarpov, I., Cretaux, J. F. (2007). Monitoring hydrological regime of the Euphrates-Tigris river basin using satellite observations. *2nd Space for Hydrology Workshop, Surface Water Storage and Runoff: Modeling, In-Situ data and Remote Sensing.* Geneva, Switzerland.

Zeng, X., Zhao, M., Dickinson, R. E. (1998). Intercomparison of bulk aerodynamic algorithms for the computation of sea surface fluxes using toga coare and tao data. *J. Clim.*, 11, 2628-2644.

APPENDICES

APPENDIX A: Mann-Kendall trend test

APPENDIX B: Student's t test

APPENDIX A

The Mann-Kendall test is non-parametric statistical method for trend analyzing in data over time. It had been formulated by Mann (1945) as non-parametric test for trend detection and the test statistic distribution had been given by Kendall (1975) for testing non-linear trend.

The Mann-Kendall statistics (S) is defined as the sum of the number of positive differences minus the number of negative differences. It is formulated as:

$$S = \sum_{i=1}^{n-1} \sum_{j=i+1}^{n} sgn(x_j - x_i) \qquad \text{(A.1)}$$

The formulation is applied to a time series of n data points x_1, x_2, ... x_n where x_j represents the data point at time j. The first step is to determine the sign of the difference between x_j and x_i:

$$sgn(x_j - x_i) = \begin{cases} +1, if \ x_j - x_i \ > 0 \\ \ 0, if \ x_j - x_i \ = 0 \\ -1, if \ x_j - x_i \ < 0 \end{cases} \qquad \text{(A.2)}$$

The magnitude of S determines the strength of the trend. A very high positive value of S represents an increasing trend, a very low negative value represents a decreasing trend. The confidence in the trend for the Mann-Kendall statistic is determined using a Kendall probability tables. First, variance of S, Var(S) is calculated as follows:

$$Var(S) = \frac{1}{18}\left[n(n-1)(2n+5) - \sum_{1}^{g}(t_p - 1)(2t_p + 5) \right] \qquad \text{(A.3)}$$

Then a normalized test statistic Z is calculated as follows:

$$Z = \begin{cases} \dfrac{S-1}{[Var(S)]^{1/2}}, if \ S > 0 \\ \quad 0, if \ S \ = 0 \\ \dfrac{S+1}{[Var(S)]^{1/2}}, if \ S < 0 \end{cases} \qquad \text{(A.4)}$$

The probability of Z is given by:

$$f(z) = \frac{1}{\sqrt{2\pi}} e^{-\frac{z^2}{2}} \qquad \text{(A.5)}$$

APPENDIX B

The Student's t-test is a statistical hypothesis test that can be used to assess whether the means of two groups are statistically different from each. It is employed under a null hypothesis and is most commonly applied when the test statistic would follow a normal distribution if the value of a scaling term in the test statistic were known.

In this study, the t-test was applied in order to check the differences between scores for reference and future climate simulations. In other words, the difference between their means to the spread or variability of their scores has been assessed. The t-value can be formulated as follows:

$$t = \frac{\overline{X}_1 - \overline{X}_2}{S_{\overline{X}_1 - \overline{X}_2}} \quad \text{(B.1)}$$

$$S_{\overline{X}_1 - \overline{X}_2} = \sqrt{\frac{S_1^2}{n_1} + \frac{S_2^2}{n_2}} \quad \text{(B.2)}$$

where S^2 is the unbiased estimator of the variance of the two samples and n is the dimension of the data.

Once the t-value is computed, it is compared with values of the table of significance in order to test whether the t-value is large enough to say that the difference between two groups is not likely to have been a chance finding. To test the significance, it is needed to set a risk level (alpha level). In addition to this the degrees of freedom is needed to determine for the test and it is given by dimension of the data minus 2. To check whether there is a significant change, a standard table of significance is used with the determined the alpha level, the degree of freedom, and the t-value.

CURRICULUM VITAE

Name Surname: Deniz Bozkurt

Place and Date of Birth: Samandağ, 28.07.1980

Address: Istanbul Technical University, Eurasia Institute of Earth Sciences, 34469 Maslak, Istanbul.

E-Mail: deniboz@gmail.com

B.Sc.: Middle East Technical University, Environmental Engineering

M.Sc.: Istanbul Technical University, Eurasia Institute of Earth Sciences

Publications:

SCI-indexed papers:

▪ Göktürk, O.M., **Bozkurt, D**., Sen, O.L., Karaca, M., 2008. Quality control and homogeneity of Turkish precipitation data. *Hydrological Processes,* vol. 22, issue 16, pp. 3210-3218 .

▪ **Bozkurt, D.**, Sen, O.L., 2011. Precipitation in the Anatolian Peninsula: sensitivity to increased SSTs in the surrounding seas. *Climate Dynamics*, 36 (3-4):711-726. DOI:10.1007/s00382-009-0651-3.

▪ Sen, O. L., Unal, A., **Bozkurt, D.**, Kindap, T. (2011). Temporal changes in the Euphrates and Tigris discharges and teleconnections. *Environ. Res. Lett.*, **6**, 024012. DOI:10.1088/1748-9326/6/2/024012.

▪ **Bozkurt, D.**, Turuncoglu, U., Sen, O. L., Onol, B., Dalfes, H. N. (2012). Downscaled simulations of the ECHAM5, CCSM3 and HadCM3 global models for the eastern Mediterranean-Black Sea region: Evaluation of the reference period. *Clim. Dyn.*, 39 (1-2), 207-225. DOI:10.1007/s00382-011-1187-x.

▪ Sen, O.L., **Bozkurt, D.**, Vogler, J.B., Ziegler, A.D., Fox, J., Giambelluca, T.W., 2012. Hydro-climatic effects of future land-cover/land-use change in montane mainland southeast Asia. *Climatic Change*, DOI 10.1007/s10584-012-0632-0, in press.

▪ **Bozkurt, D.**, Sen, O. L. (2013). Climate change impacts in the Euphrates-Tigris Basin based on different model and scenario simulations. *J. Hydrol.*, 480, 149-161. DOI:10.1016/j.hydrol.2012.12.021.

▪ Sen, O.L., **Bozkurt, D.**, Fox, J., Vogler, J.B., Giambelluca, T.W., Ziegler, A.D., 2012. Projected impacts of global warming on regional climate in southeast Asia. *Climate Dynamics*, in revision.

▪ Önol, B., **Bozkurt, D.**, Turuncoglu, U.U., Sen, O.L., Dalfes, H.N., 2012. Evaluation of the 21st century RCM simulations driven by multiple GCMs over the Eastern Mediterranean-Black Sea region, *Climate Dynamics*, in revision.

Peer reviewed proceedings:

▪ Karaca, M., Ezber, Y., Cengiz, T., Gokturk, O.M., **Bozkurt, D.**, Kindap, T., and Sen, O.L., 2006. Regional climate change after Southeast Anatolia Project (in Turkish), *Proceedings of the GAP V. Engineering Congress- 2. Volume, Şanlıurfa*, 1612-1619.

▪ Turunçoğlu, U.U., Önol, B., **Bozkurt, D.**, 2008. Regional climate change projections with dynamic models (in Turkish). *Proceedings of the Forests in the Resolution of Global Climate Change and Water Related Issues. Turkish Foresters Association, Istanbul*. 47-54.

▪ Bozkurt, **D.**, Sen, O.L., 2009. Sensitivity of Turkish precipitation to SST variability in the surrounding seas. *Proceedings of the International Conference on Environment: Survival and Sustainability Vol. 10, pp. 4965-4974. Near East University, Nicosia-Northern Cyprus.*

▪ **Bozkurt, D.**, Sen, O.L., 2010. Last floods: Is our sea getting warmer? (in Turkish), *Proceedings of the II. National Flood Symposium, Afyon*, 249-253.

▪ Sen, O.L., **Bozkurt, D.**, 2010. An atmosphere-hydrology system for Middle Euphrates Basin and a case study (in Turkish), *Proceedings of the II. National Flood Symposium, Afyon*, 275-280**.**

▪ **Bozkurt, D.**, Sen, O.L., 2011. Future climate change impacts on water resources of Fırat Basin (in Turkish), *Proceedings of the V. National Water Engineering Symposium*, Istanbul, 199-207.

Conference Papers, Posters and Presentations:

▪ **Bozkurt, D.**, Göktürk, O.M., 2006. Quality control and homogenization of Turkish precipitation and streamflow data sets. *Geophysical Research Abstracts, Vol. 8, 07488.*

▪ **Bozkurt, D.**, Sen, O.L., 2007. Sensitivity of Turkish precipitation to sea surface temperature variabilities in the surrounding seas. *Geophysical Research Abstracts, Vol. 9, EGU2007-A-02667.*

▪ **Bozkurt, D.**, Sen, O.L., Karaca, M., 2008. Wet season evaluation of RegCM3 performance for Eastern Mediterranean. *Geophysical Research Abstracts, Vol. 10, EGU2008-A-04210.*

▪ **Bozkurt, D.**, Sen, O.L., Turunçoğlu, U.U., Karaca, M. and Dalfes, H.N., 2008. Regional climate change projections for Eastern Mediterranean: Preliminary results, *Geophysical Research Abstracts, Vol. 10, EGU2008-A-04264.*

▪ Can, Z., Bozkurt, K., **Bozkurt, D.**, Elcin, B., Oğuz, O. and Kutlu, K., 2008. Investigation of interactions of GPS signals with ionosphere in Marmara region. *URSI General Assembly, Chicago, USA.*

▪ **Bozkurt, D.**, Sen, O.L., Turunçoğlu, U.U., Onol, B., Kindap, T., Dalfes, H.N., and Karaca, M., 2010. Impacts of climate change on hydrometeorology of the Euphrates and Tigris Basins*, Geophysical Research Abstracts, Vol. 12, EGU2010-14278*.

▪ Sen, O.L., Unal, A., Kindap, T., **Bozkurt, D.**, Dalfes, H.N., and Karaca, M., 2010. Past and future changes in the discharges of the Euphrates and Tigris Rivers*, Geophysical Research Abstracts, Vol. 12, EGU2010-10135*.

▪ **Bozkurt, D.**, Sen, O.L., 2011. Hyrdological response of past and future climate changes in the Euphrates-Tigris Basin, *Geophysical Research Abstracts, Vol. 13, EGU2011-11072*.

▪ **Bozkurt, D.**, Onol, B., Sen, O.L., 2011. Simulated intense convective precipitation over the Black Sea coasts: sensitivity to temporal modifications of SST, *Geophysical Research Abstracts, Vol. 13, EGU2011-12911.*

▪ **Bozkurt, D**., **Sen, O.L.**, 2012. Snow Dynamics of the eastern Anatolio region during the last 20 years: A modeling study. Mountain Resources and Their Response to Global Change, SEEmore Conference 2012 Abstract Book, Ankara University Press, pp. 21-22, Ankara.

▪ **Bozkurt, D**., **Sen, O.L.**, 2012. Impacts of climate change in the Euphrates-Tigris Basin. Mountain Resources and Their Response to Global Change, SEEmore Conference 2012 Abstract Book, Ankara University Press, pp. 16-17, Ankara**.**

▪ **Bozkurt, D.,** Sen, O.L., 2012. Snow dynamics of the Eastern Anatolia Region during the last decades: A modeling study. Abstract A41I-0093 presented at 2012 Fall Meeting, AGU, San Francisco, Calif., 3-7 Dec.

Given seminars:

▪ Climate change in the Euphrates-Tigris Basin (14.03.2012). ZMAW/KlimaCampus Seminar, Max Planck Institute for Meteorology, Hamburg-Germany.